Study on Carriers Generated in Ionic-Liquid-Gated Transistors Fabricated with PBTTT

PBTTT を用いて作製した イオン液体トランジスター中に生成する キャリヤーに関する研究

February 2019

Ippei ENOKIDA

榎田　一平

Study on Carriers Generated in Ionic-Liquid-Gated Transistors Fabricated with PBTTT

PBTTT を用いて作製した イオン液体トランジスター中に生成する キャリヤーに関する研究

February 2019

Waseda University

Graduate School of Advanced Science and Engineering

Department of Advanced Science and Engineering

Research on Chemistry and Biochemistry

Ippei ENOKIDA

榎田　一平

Contents

List of abbreviations

I_D	Drain current
I_G	Gate current
V_D	Drain voltage
V_G	Gate voltage
I_L	Leak current
OTFT	Organic thin-film transistor
OFET	Organic field-effect transistor
ILGT	Ionic-liquid-gated transistor
EDL	Electric double layer
ESR	Electron spin resonance
P3HT	Poly(3-hexylthiophene-2,5-diyl)
PBTTT	Poly(2,5-bis(3-alkylthiophen-2-yl)thieno[3,2-b]thiophene)
PBTTT-C14	Poly(2,5-bis(3-tetradecylthiophen-2-yl)thieno[3,2-b]thiophene)
PBTTT-C16	Poly(2,5-bis(3-hexadecyllthiophen-2-yl)thieno[3,2-b]thiophene)
ITO	Indium-tin oxide
XRD	X-ray diffraction
AFM	Atomic force microscopy
HOMO	Highest occupied molecular orbital
FWHM	Full width at half maximum
[BMIM][TFSI]	1-butyl-3-methylimidazolium bis(trifluoromethylsulfonyl)imide
[EMIM][TFSI]	1-ethyl-3-methylimidazolium bis(trifluoromethylsulfonyl)imide
[EMIM][FAP]	1-ethyl-3-methylimidazolium tris(pentafluoroethyl)trifluorophosphate

Chapter 1

Introduction

1.1 General introduction

Organic semiconductors have received considerable attention for fabricating various electric devices, such as transistors [1–4], solar cells [5–8], light-emitting diodes [9,10], lasers [11,12], and thermoelectric elements [13,14]. Electric devices are a key factor in advancing society. Currently, inorganic materials such as Si are used for fabricating such electric devices. However, the manufacturing processes for inorganic semiconductors, such as film formation by dry processes, require high vacuum and high temperatures. These processes must be conducted on a massive scale for manufacturing inorganic devices, resulting in significant energy and resource consumption. In the future, the demand for electric devices will increase, reducing the barriers around sharing information and producing energy. Using organic materials has some advantages over using inorganic semiconductors. Organic devices are less expensive, and because they are soluble, fabricating large-area devices is much easier as a wet process can be used. Wet processes are spin coating [15–17], inkjet printing [18–20], etc. [21–23]. These technologies are environmentally friendly and consume less energy. In addition, these techniques can be used to fabricate light, thin and flexible devices that are expected to be applicable in many situations.

Recently, organic EL have been used for smartphone displays. However, other organic devices have not been put into practical use because the electrical characteristics have not reached sufficient levels yet. Advancing organic transistors to the point where organic EL flexible displays are practical is of great interest. Investigations in this field have been directed toward the synthesis of semiconductors with new structures [24–27], the optimization of solid-state materials [28–30] and the modification of process engineering techniques [31–33]. Thermal annealing is the most well-known method for increasing the crystallinity of an organic semiconductor film. In a crystalline state, organic semiconductors are aligned and ordered, which results in good overlap of the π electrons. This overlap increases the mobility of the carriers, allowing them to move quickly in the crystal.

A theoretical understanding of organic semiconductors is important for developing this field. Recently, the importance of theory-guided material design, such as using quantum chemical calculation, has become obvious [34–36]. T. Yamamoto and K. Takimiya predicted promising new organic semiconductors using molecular orbital (MO) calculations before synthesis [37]. Z. Bao et al. also used computational screening before synthesis and achieved a very high mobility (16 $cm^2 V^{-1} s^{-1}$) [38]. Thus, a strong theoretical understanding will greatly facilitate the design of

organic semiconductors with improved performance. However, in theoretical understanding, the effects of carrier species in organic devices have not been elucidated sufficiently. There are two types of carriers, a polaron and a bipolaron in a nondegenerate conjugated polymer, which is explained in detail in Section 1.3. A polaron has $+e$ or $-e$, and a bipolaron has $+2e$ or $-2e$. It has been reported that a bipolaron affects the electrical properties of organic devices [39–41]. However, the carrier species generated in these devices are identified using ESR or the effect was explained by a simulation. They cannot dismiss the effect of a polaron pair. Therefore, elucidating the fundamental mechanism of carrier species, such as electron-lattice interactions, charge transport and carrier generation, is of great importance.

1.2 Organic transistors

Organic transistors, often called OTFTs or OFETs are promising organic devices. Transistors can amplify or switch an electric current. These devices were used as a tool for evaluating the charge transport properties of organic semiconductors early in the development of this field, and the mobility of the first OTFT was only 10^{-5} cm^2 V^{-1} s^{-1} [42]. In these days, OTFTs were intended for use in flexible devices such as displays, ID tags and banknotes [43–46]. Today, their mobilities are approaching those of polycrystalline silicon transistors (>10 cm^2 V^{-1} s^{-1}). In particular, single crystal semiconductors show high mobilities; for example, rubrene transistors achieved a mobility of 18 cm^2 V^{-1} s^{-1} [47]. Polymer semiconductors have attracted great research interest because of their facile solution processing and good mechanical properties. Beng S. Ong et al. reported a high mobility in the saturation regime (up to 10.5 cm^2 V^{-1} s^{-1}) with N-alkyl diketopyrrolopyrrole-dithienylthieno[3,2-b]thiophene (DPP-DTT), which is a polymer semiconductor [48]. Thus, polymer semiconductors with a high mobility have already been synthesized.

The configuration of OFETs, which are called bottom gate and bottom contact devices, is shown in Figure 1.1. These devices have three electrodes; a gate, a source and a drain. Organic semiconductors are used as an active layer. Highly doped silicon crystals are typically used as the gate electrode with silicon-oxide layers as insulators. The I_D, which flows between the source and the drain electrodes, can be modified by tuning not only the V_D but also the V_G. When the V_G is applied, an electric field is generated, and the electric charge accumulates in the active layer. During charge accumulation, the organic semiconductors are doped, and the carriers are generated. These carriers are transported as the I_D. Therefore, the value of I_D depends on the charge

concentration.

For heavily doped organic semiconductors, electrolytes can be used as an insulator [49,50]. They have a high capacitance, which leads to a high I_D and a low operating voltage because they can achieve high charge accumulation. C. D. Frisbie et al. used ionic liquids as the insulator [51] because they offer additional advantages. They have wide potential windows that facilitate high charge density (up to 10^{21} cm^{-3}) [52,53]. There are many kinds of ionic liquids, which allows their role in doping to be assessed. Therefore, ILGTs are more attractive for practical applications. The weak point of ILGTs is their slow response speed, which can be a few kHz because ions in ionic liquids move slowly under an applied voltage. Therefore, it is difficult to use ILGTs as logic circuits such as CPUs. However, ILGTs are fast enough to be used in illumination as displays and biosensor because human biosignals are slower than 1 kHz.

There are two ways of doping ILGTs: electrostatic and electrochemical doping, as shown in Figure 1.2 [54,55]. In electrostatic doping, cations and anions are alternatively superimposed to form an EDL by applying a V_G at the interface between an ionic liquid and an active layer, and this results in a doped organic semiconductor. In electrochemical doping, the anions of ionic liquids at the interface penetrate into an organic semiconductor film, and the active layer is doped. Importantly, electrochemical doping can achieve a high carrier density and heavy doping not only at the interface but also in the bulk region of the active layer. To investigate a bipolaron, the active layer must be heavily doped, and ILGTs are useful for researching doping mechanisms and carrier generation in organic semiconductors because the carrier concentration can be evaluated by electrochemical measurements [52,56–60].

1.3 Carrier species of conjugated polymers

Carrier species are important for understanding electrical properties. In conjugated polymers with a degenerate ground state and alternating C−C and C=C bonds, such as *trans*-polyacetylene, charged solitons serve as the carriers [61]. Conjugated polymers with a nondegenerate ground state have two types of carriers: polarons and bipolarons [62–64]. A polaron and a bipolaron in polythiophene are shown in Figure 1.3. Most conjugated polymers are nondegenerate as none of their ground state structures are identical. A polaron has $+e$ or $-e$ and a spin of 1/2. The charge is localized over several rings of the polymer, which causes a change in geometry. For example, structural changes from benzenoid to quinoid moieties can occur, as shown in Figure 1.4. When

another electron is removed from or appended to the conjugated polymer, two polarons are or a bipolaron which has +2*e* or −2*e* and no spin, is formed. At a low doping level, a polaron was generated, and a bipolaron was generated at a high doping level [63,65]. These carrier species affect the electrical, magnetic and optical properties of the polymer [56,58,66–69].

Carrier species can be identified using optical absorption spectroscopy, vibrational spectroscopy and ESR spectroscopy. However, carrier identification is difficult in the early stage of studying these physical properties. When a polaron or a bipolaron is formed, two electronic levels ($+\omega_0$ and $-\omega_0$ for a polaron and $+\omega_0$' and $-\omega_0$' for a bipolaron) are formed. No electron is in the $-\omega_0$' level. The model developed by Fesser, Bishop and Campbell [70] shows that a polaron has three transition, and a bipolaron has two transition, as shown in Figure 1.5. A polaron has two allowed transitions: the P1 transition from the valence band to the $-\omega_0$ level and the P2 transition from the $-\omega_0$ level to the $+\omega_0$ level. The P3 transitions from the $-\omega_0$ level to a conduction band or from the valence band to the $+\omega_0$ level are forbidden. A Bipolaron has one allowed transition, BP1, which is from the valence band to the $-\omega_0$' level. The BP3 transition from the valence band to the $+\omega_0$' level is forbidden. In addition, a polaron show ESR signals because it has a spin of 1/2. As experimental results, two absorption bands were observed in polythiophene [71], and the ESR signals of a doped polythiophene were smaller than those expected from an injected charge [72]. The ESR result indicated that spinless carriers, bipolarons, were generated. Therefore, A. J. Heeger et al. suggested that bipolarons were generated mainly in doped polythiophene, and polarons were generated only at a so low doping level [73]. This assignment was widely applied to other conjugated polymers. Therefore, for a long time, bipolarons were considered the major species generated by doping.

This assignment, however, was not correct [74]. Fesser's model predicts that the intense of the allowed transition, BP1 is much stronger than that of the forbitten transition, BP3. Two absorption bands observed in a doped polythiophene should be assigned to polarons in this respect. In addition, other studies of doped oligomers showed that the two bands should be attributed to polarons [75,76]. Shimoi et al. also showed that the two bands should be attributed to polarons and one band could be attributed to bipolarons using calculations in the presence of electron-electron interactions [77]. In addition, it was suggested that a pair of polarons gives rise to no ESR signal [74]. Therefore, two absorption bands should be assigned to polarons, and one absorption band should be attributed to bipolarons. Thus, it was difficult to correctly identify the carrier species of doped conjugated polymers. Currently, carrier species can be correctly identified.

Therefore, not only major carriers but also minor carriers (bipolarons) should be investigated to fully understand the physical properties of organic semiconductors.

In situ measurements of carrier generation in an operated transistor are also difficult. Carriers are generated in the channel region of transistors, and this region in an operated transistor is too small to use optical absorption spectroscopy. ESR is often used to investigate operated transistors. However, a spinless carrier such as a bipolaron cannot be observed directly using ESR mesurement. Vibrational spectroscopy is also a powerful tool for studying the structures of carriers. Band positions shift due to changes in bond length, the force constant and localization of charges. When carriers are generated, infrared active vibrational modes are strongly observed, and they were explained on the basis of the effective conjugation theory [78]. However, using IR spectroscopy to elucidate the structure of the device is difficult because glass does not transmit some wavelengths of infrared light. Raman spectroscopy can be used to observe the polarons and bipolarons generated in the microscale area through a glass barrier. This method is useful for investigating carrier generation in organic devices such as ILGTs.

1.4 Outline of thesis

The outline of this thesis is as follows. In Chapter 2, I discuss the ILGTs fabricated with PBTTT-C14 and [BMIM][TFSI]. Raman and optical absorption spectra of a PBTTT-C14 film doped with $FeCl_3$ were acquired, and Raman spectra of positive polarons and bipolarons in PBTTT-C14 were identified. The generation of polarons and bipolarons in the ILGT fabricated with PBTTT-C14 was observed using Raman spectroscopy. Conductivities, doping levels and mobilities of this ILGT were determined using electrochemical measurements. The relationship between carrier species and these electric properties was investigated. I show high bipolaron mobilities in PBTTT-C14 using of the ILGT configuration. In Chapter 3, I discuss the ILGTs fabricated with unannealed and annealed PBTTT-C16 films. The crystalline contents of PBTTT-C16 films were evaluated using Raman spectroscopy. Raman and optical absorption spectra of a PBTTT-C16 film doped with $FeCl_3$ were acquired, and Raman spectra of positive polarons and bipolarons of PBTTT-C16 were identified. I determined the doping levels and the mobilities of polarons and bipolarons using Raman spectroscopy and electrochemical measurements on the ILGTs. The bipolaron mobilities of unannealed and annealed PBTTT-C16 were high. I showed the effect of high crystalline contents on carrier generation and mobilities. In Chapter 4, I discuss

the investigation of the relationship between carrier generation and the size of the anions in ionic liquids. I measured ILGTs fabricated with [EMIM][TFSI] and [EMIM][FAP] using Raman spectroscopy and electrochemical measurements. I showed that large anions impeded bipolaron formation in ILGTs. In Chapter 5, I discuss the conclusions of the thesis.

1.5 References

[1] H. Koezuka, A. Tsumura, T. Ando, Field-effect transistor with polythiophene thin film, Synth. Met. 18 (1987) 699–704. doi:10.1016/0379-6779(87)90964-7.

[2] P.F. Baude, D.A. Ender, M.A. Haase, T.W. Kelley, D. V. Muyres, S.D. Theiss, Pentacene-based radio-frequency identification circuitry, Appl. Phys. Lett. 82 (2003) 3964–3966. doi:10.1063/1.1579554.

[3] H. Sirringhaus, Device physics of solution-processed organic field-effect transistors, Adv. Mater. 17 (2005) 2411–2425. doi:10.1002/adma.200501152.

[4] T. Hasegawa, J. Takeya, Organic field-effect transistors using single crystals, Sci. Technol. Adv. Mater. 10 (2009) 024314. doi:10.1088/1468-6996/10/2/024314.

[5] N.S. Sariciftci, L. Smilowitz, A.J. Heeger, F. Wudl, A.J. Heeger, Photoinduced electron transfer from a conducting polymer to buckminsterfullerene, Science. 258 (1992) 1474–1476. doi:10.1126/science.258.5087.1474.

[6] M. Hiramoto, H. Fujiwara, M. Yokoyama, p-i-n like behavior in three-layered organic solar cells having a co-deposited interlayer of pigments, J. Appl. Phys. 72 (1992) 3781–3787. doi:10.1063/1.352274.

[7] C.W. Tang, Two-layer organic photovoltaic cell, Appl. Phys. Lett. 48 (1986) 183–185. doi:10.1063/1.96937.

[8] W. Zhao, S. Li, H. Yao, S. Zhang, Y. Zhang, B. Yang, J. Hou, Molecular optimization enables over 13% efficiency in organic solar cells, J. Am. Chem. Soc. 139 (2017) 7148–7151. doi:10.1021/jacs.7b02677.

[9] C.W. Tang, S.A. VanSlyke, Organic electroluminescent diodes, Appl. Phys. Lett. 51 (1987) 913–915. doi:10.1063/1.98799.

[10] W. Brütting, S. Berleb, A.G. Mückl, Device physics of organic light-emitting diodes based on molecular materials, Org. Electron. 2 (2001) 1–36. doi:10.1016/S1566-1199(01)00009-X.

[11] A.J.C. Kuehne, M.C. Gather, Organic lasers: recent developments on materials, device geometries, and fabrication techniques, Chem. Rev. 116 (2016) 12823–12864. doi:10.1021/acs.chemrev.6b00172.

[12] A.K. Bansal, A. Penzkofer, Linear and nonlinear optical spectroscopic characterisation of triphenylamine and 1,2,3-tris(3-methylphenylphenylamino)benzene, Chem. Phys. 352

(2008) 48–56. doi:10.1016/J.CHEMPHYS.2008.05.006.

[13] O. Bubnova, X. Crispin, Towards polymer-based organic thermoelectric generators, Energy Environ. Sci. 5 (2012) 9345. doi:10.1039/c2ee22777k.

[14] G.-H. Kim, L. Shao, K. Zhang, K.P. Pipe, Engineered doping of organic semiconductors for enhanced thermoelectric efficiency, Nat. Mater. 12 (2013) 719–723. doi:10.1038/nmat3635.

[15] J.-F. Chang, B. Sun, D.W. Breiby, M.M. Nielsen, T.I. Sölling, M. Giles, Iain McCulloch, H. Sirringhaus, Enhanced mobility of poly(3-hexylthiophene) transistors by spin-coating from high-boiling-point solvents, Chem. Mater. 16 (2004) 4772–4776. doi:10.1021/CM049617W.

[16] Y. Yuan, G. Giri, A.L. Ayzner, A.P. Zoombelt, S.C.B. Mannsfeld, J. Chen, D. Nordlund, M.F. Toney, J. Huang, Z. Bao, Ultra-high mobility transparent organic thin film transistors grown by an off-centre spin-coating method, Nat. Commun. 5 (2014) 3005. doi:10.1038/ncomms4005.

[17] F. Zhang, C. Di, N. Berdunov, Y. Hu, Y. Hu, X. Gao, Q. Meng, H. Sirringhaus, D. Zhu, Ultrathin film organic transistors: precise control of semiconductor thickness via spin-coating, Adv. Mater. 25 (2013) 1401–1407. doi:10.1002/adma.201204075.

[18] H. Gau, S. Herminghaus, P. Lenz, R. Lipowsky, M. Inbasekaran, W. Wu, E.P. Woo, Liquid morphologies on structured surfaces: from microchannels to microchips, Science 283 (1999) 46–49. doi:10.1126/science.283.5398.46.

[19] H. Minemawari, T. Yamada, H. Matsui, J. Tsutsumi, S. Haas, R. Chiba, R. Kumai, T. Hasegawa, Inkjet printing of single-crystal films, Nature. 475 (2011) 364–367. doi:10.1038/nature10313.

[20] T. Kawase, H. Sirringhaus, R.H. Friend, T. Shimoda, Inkjet printed via-hole interconnections and resistors for all-polymer transistor circuits, Adv. Mater. 13 (2001) 1601–1605. doi:10.1002/1521-4095(200111)13:21<1601::AID-ADMA1601>3.0.CO;2-X.

[21] T. Uemura, Y. Hirose, M. Uno, K. Takimiya, J. Takeya, Very high mobility in solution-processed organic thin-film transistors of highly ordered [1]benzothieno[3,2-b]benzothiophene derivatives, Appl. Phys. Express. 2 (2009) 111501. doi:10.1143/APEX.2.111501.

[22] K. Nakayama, Y. Hirose, J. Soeda, M. Yoshizumi, T. Uemura, M. Uno, W. Li, M.J. Kang,

M. Yamagishi, Y. Okada, E. Miyazaki, Y. Nakazawa, A. Nakao, K. Takimiya, J. Takeya, Patternable solution-crystallized organic transistors with high charge carrier mobility, Adv. Mater. 23 (2011) 1626–1629. doi:10.1002/adma.201004387.

[23] M. Uno, Y. Tominari, M. Yamagishi, I. Doi, E. Miyazaki, K. Takimiya, J. Takeya, Moderately anisotropic field-effect mobility in dinaphtho[2,3-b:2',3'-f]thiopheno[3,2-b]thiophenes single-crystal transistors, Appl. Phys. Lett. 94 (2009) 223308. doi:10.1063/1.3153119.

[24] I. McCulloch, M. Heeney, C. Bailey, K. Genevicius, I. MacDonald, M. Shkunov, D. Sparrowe, S. Tierney, R. Wagner, W. Zhang, M.L. Chabinyc, R.J. Kline, M.D. McGehee, M.F. Toney, Liquid-crystalline semiconducting polymers with high charge-carrier mobility, Nat. Mater. 5 (2006) 328–333. doi:10.1038/nmat1612.

[25] B.S. Ong, Yiliang Wu, Ping Liu, S. Gardner, High-performance semiconducting polythiophenes for organic thin-film transistors, 126 (2004) 3378–3379. doi:10.1021/JA039772W.

[26] H.H. Fong, V.A. Pozdin, A. Amassian, G.G. Malliaras, D.-M. Smilgies, M. He, S. Gasper, F. Zhang, M. Sorensen, Tetrathienoacene copolymers as high mobility, soluble organic semiconductors, J. Am. Chem. Soc. 130 (2008) 13202–13203. doi:10.1021/ja804872x.

[27] I. Osaka, S. Shinamura, T. Abe, K. Takimiya, Naphthodithiophenes as building units for small molecules to polymers; a case study for in-depth understanding of structure–property relationships in organic semiconductors, J. Mater. Chem. C. 1 (2013) 1297–1304. doi:10.1039/C2TC00261B.

[28] D.M. DeLongchamp, R.J. Kline, Y. Jung, D.S. Germack, E.K. Lin, A.J. Moad, L.J. Richter, M.F. Toney, M. Heeney, I. McCulloch, Controlling the orientation of terraced nanoscale "ribbons" of a poly(thiophene) semiconductor, ACS Nano. 3 (2009) 780–787. doi:10.1021/nn800574f.

[29] T. Umeda, S. Tokito, D. Kumaki, High-mobility and air-stable organic thin-film transistors with highly ordered semiconducting polymer films, J. Appl. Phys. 101 (2007) 054517. doi:10.1063/1.2711780.

[30] H. Ito, T. Harada, H. Tanaka, S. Kuroda, Critical regime for the insulator–metal transition in highly ordered conjugated polymers gated with ionic liquid, Jpn. J. Appl. Phys. 55 (2016) 03DC08. doi:10.7567/JJAP.55.03DC08.

[31] J. Rivnay, L.H. Jimison, J.E. Northrup, M.F. Toney, R. Noriega, S. Lu, T.J. Marks, A.

Facchetti, A. Salleo, Large modulation of carrier transport by grain-boundary molecular packing and microstructure in organic thin films, Nat. Mater. 8 (2009) 952–958. doi:10.1038/nmat2570.

[32] M.M.L. And, Z. Bao, Thin film deposition, patterning, and printing in organic thin film transistors, Chem. Mater. 16 (2004) 4824–4840. doi:10.1021/CM0496117.

[33] F.C. Krebs, Fabrication and processing of polymer solar cells: a review of printing and coating techniques, Sol. Energy Mater. Sol. Cells. 93 (2009) 394–412. doi:10.1016/J.SOLMAT.2008.10.004.

[34] L. Wang, G. Nan, X. Yang, Q. Peng, Q. Li, Z. Shuai, Computational methods for design of organic materials with high charge mobility, Chem. Soc. Rev. 39 (2010) 423–434. doi:10.1039/B816406C.

[35] J. Hachmann, R. Olivares-Amaya, S. Atahan-Evrenk, C. Amador-Bedolla, R.S. Sánchez-Carrera, A. Gold-Parker, L. Vogt, A.M. Brockway, A. Aspuru-Guzik, The Harvard clean energy project: large-scale computational screening and design of organic photovoltaics on the world community grid, J. Phys. Chem. Lett. 2 (2011) 2241–2251. doi:10.1021/jz200866s.

[36] R. Gómez-Bombarelli, J. Aguilera-Iparraguirre, T.D. Hirzel, D. Duvenaud, D. Maclaurin, M.A. Blood-Forsythe, H.S. Chae, M. Einzinger, D.-G. Ha, T. Wu, G. Markopoulos, S. Jeon, H. Kang, H. Miyazaki, M. Numata, S. Kim, W. Huang, S.I. Hong, M. Baldo, R.P. Adams, A. Aspuru-Guzik, Design of efficient molecular organic light-emitting diodes by a high-throughput virtual screening and experimental approach, Nat. Mater. 15 (2016) 1120–1127. doi:10.1038/nmat4717.

[37] T. Yamamoto, K. Takimiya, Facile synthesis of highly π-extended heteroarenes, dinaphtho[2,3-b:2‘,3‘-f]chalcogenopheno[3,2-b]chalcogenophenes, and their application to field-effect transistors, J. Am. Chem. Soc. 129 (2007) 2224–2225. doi:10.1021/JA068429Z.

[38] A.N. Sokolov, S. Atahan-Evrenk, R. Mondal, H.B. Akkerman, R.S. Sánchez-Carrera, S. Granados-Focil, J. Schrier, S.C.B. Mannsfeld, A.P. Zoombelt, Z. Bao, A. Aspuru-Guzik, From computational discovery to experimental characterization of a high hole mobility organic crystal, Nat. Commun. 2 (2011) 437. doi:10.1038/ncomms1451.

[39] J. Behrends, A. Schnegg, K. Lips, E.A. Thomsen, A.K. Pandey, I.D.W. Samuel, D.J. Keeble, Bipolaron formation in organic solar cells observed by pulsed electrically

detected magnetic resonance, Phys. Rev. Lett. 105 (2010) 176601. doi:10.1103/PhysRevLett.105.176601.

[40] L.S. Swanson, J. Shinar, A.R. Brown, D.D.C. Bradley, R.H. Friend, P.L. Burn, A. Kraft, A.B. Holmes, Electroluminescence-detected magnetic-resonance study of polyparaphenylenevinylene (PPV)-based light-emitting diodes, Phys. Rev. B. 46 (1992) 15072–15077. doi:10.1103/PhysRevB.46.15072.

[41] P.A. Bobbert, T.D. Nguyen, F.W.A. van Oost, B. Koopmans, M. Wohlgenannt, Bipolaron mechanism for organic magnetoresistance, Phys. Rev. Lett. 99 (2007) 216801. doi:10.1103/PhysRevLett.99.216801.

[42] A. Tsumura, H. Koezuka, T. Ando, Macromolecular electronic device: Field-effect transistor with a polythiophene thin film, Appl. Phys. Lett. 49 (1986) 1210–1212. doi:10.1063/1.97417.

[43] V. Subramanian, P.C. Chang, J.B. Lee, S.E. Molesa, S.K. Volkman, Printed organic transistors for ultra-low-cost RFID applications, IEEE Trans. Components Packag. Technol. 28 (2005) 742–747. doi:10.1109/TCAPT.2005.859672.

[44] U. Zschieschang, T. Yamamoto, K. Takimiya, H. Kuwabara, M. Ikeda, T. Sekitani, T. Someya, H. Klauk, Organic electronics on banknotes, Adv. Mater. 23 (2011) 654–658. doi:10.1002/adma.201003374.

[45] S.-J. Kim, J.-S. Lee, Flexible organic transistor memory devices, Nano Lett. 10 (2010) 2884–2890. doi:10.1021/nl1009662.

[46] G. Gelinck, P. Heremans, K. Nomoto, T.D. Anthopoulos, Organic transistors in optical displays and microelectronic applications, Adv. Mater. 22 (2010) 3778–3798. doi:10.1002/adma.200903559.

[47] J. Takeya, M. Yamagishi, Y. Tominari, R. Hirahara, Y. Nakazawa, T. Nishikawa, T. Kawase, T. Shimoda, S. Ogawa, Very high-mobility organic single-crystal transistors with in-crystal conduction channels, Appl. Phys. Lett. 90 (2007) 102120. doi:10.1063/1.2711393.

[48] J. Li, Y. Zhao, H.S. Tan, Y. Guo, C.-A. Di, G. Yu, Y. Liu, M. Lin, S.H. Lim, Y. Zhou, H. Su, B.S. Ong, A stable solution-processed polymer semiconductor with record high-mobility for printed transistors, Sci. Rep. 2 (2012) 754. doi:10.1038/srep00754.

[49] D. Ofer, R.M. Crooks, M.S. Wrighton, Potential dependence of the conductivity of highly oxidized polythiophenes, polypyrroles, and polyaniline: finite windows of high

conductivity, J. Am. Chem. Soc. 112 (1990) 7869–7879. doi:10.1021/ja00178a004.

[50] H.S. White, G.P. Kittlesen, M.S. Wrighton, Chemical derivatization of an array of three gold microelectrodes with polypyrrole: fabrication of a molecule-based transistor, J. Am. Chem. Soc. 106 (1984) 5375–5377. doi:10.1021/ja00330a070.

[51] J. Lee, M.J. Panzer, Y. He, T.P. Lodge, C.D. Frisbie, Ion gel gated polymer thin-film transistors, J. Am. Chem. Soc. 129 (2007) 4532–4533. doi:10.1021/JA070875E.

[52] Y. Ando, H. Ito, S. Watanabe, S. Kuroda, Variable-range hopping conduction in ion-gel-gated electrochemical transistors of regioregular poly(3-hexylthiophene), J. Phys. Soc. Japan. 81 (2012) 114721. doi:10.1143/JPSJ.81.114721.

[53] B.D. Paulsen, C.D. Frisbie, Dependence of conductivity on charge density and electrochemical potential in polymer semiconductors gated with ionic liquids, J. Phys. Chem. C. 116 (2012) 3132–3141. doi:10.1021/jp2093934.

[54] J.D. Yuen, A.S. Dhoot, E.B. Namdas, N.E. Coates, M. Heeney, I. McCulloch, D. Moses, A.J. Heeger, Electrochemical doping in electrolyte-gated polymer transistors, (2007). doi:10.1021/JA0749845.

[55] Y. Nagasaki, J.-H. Lee, Y. Kubozono, T. Kambe, Dynamics of carrier injection in picene thin-film field-effect transistors with an ionic liquid sheet and ionic liquid gel, Org. Electron. 15 (2014) 3070–3075. doi:10.1016/J.ORGEL.2014.08.043.

[56] J. Yamamoto, Y. Furukawa, Raman characterization and electrical properties of poly(3-hexylthiophene) doped electrochemically in an ionic liquid-gated transistor geometry, Org. Electron. 28 (2016) 82–87. doi:10.1016/J.ORGEL.2015.10.016.

[57] Y. Wada, I. Enokida, J. Yamamoto, Y. Furukawa, Raman imaging of carrier distribution in the channel of an ionic liquid-gated transistor fabricated with regioregular poly(3-hexylthiophene), Spectrochim. Acta Part A Mol. Biomol. Spectrosc. 197 (2018) 166–169. doi:10.1016/J.SAA.2018.01.043.

[58] Y. Furukawa, K. Akiyama, I. Enokida, J. Yamamoto, Raman spectra of carriers in ionic-liquid-gated transistors fabricated with poly(2,5-bis(3-tetradecylthiophen-2-yl)thieno[3,2-b]thiophene), Vib. Spectrosc. 85 (2016) 29–34. doi:10.1016/J.VIBSPEC.2016.03.024.

[59] H. Tanaka, M. Hirate, S. Watanabe, S. Kuroda, Microscopic signature of metallic state in semicrystalline conjugated polymers doped with fluoroalkylsilane molecules, Adv. Mater. 26 (2014) 2376–2383. doi:10.1002/adma.201304691.

[60] H. Tanaka, S. Nishio, H. Ito, S. Kuroda, Microscopic signature of insulator-to-metal transition in highly doped semicrystalline conducting polymers in ionic-liquid-gated transistors, Appl. Phys. Lett. 107 (2015) 243302. doi:10.1063/1.4938137.

[61] W.P. Su, J.R. Schrieffer, A.J. Heeger, Solitons in Polyacetylene, Phys. Rev. Lett. 42 (1979) 1698–1701. doi:10.1103/PhysRevLett.42.1698.

[62] S.A. Brazovskiĭ, N.N. Kirova, Excitons, polrons, and bipolarons in conductiong polymers, Sov. Phys. JETP Lett. 33 (1981) 4.

[63] J.E. Brédas, R.R. Chance, R. Silbey, Theoretical studies of charged defect states in doped polyacetylene and polyparaphenylene, Mol. Cryst. Liq. Cryst. 77 (1981) 319–332. doi:10.1080/00268948108075251.

[64] A.R. Bishop, D.K. Campbell, K. Fesser, Polyacetylene and relativistic field theory models, Mol. Cryst. Liq. Cryst. 77 (1981) 253–264. doi:10.1080/00268948108075245.

[65] Y. Shimoi, S. Abe, Competition between polarons and bipolarons in nondegenerate conjugated polymers, Phys. Rev. B. 50 (1994) 14781–14784. doi:10.1103/PhysRevB.50.14781.

[66] Z. Pomerantz, A. Zaban, S. Ghosh, J.-P. Lellouche, G. Garcia-Belmonte, J. Bisquert, Capacitance, spectroelectrochemistry and conductivity of polarons and bipolarons in a polydicarbazole based conducting polymer, J. Electroanal. Chem. 614 (2008) 49–60. doi:10.1016/J.JELECHEM.2007.11.005.

[67] R.A. Street, A. Salleo, M.L. Chabinyc, Bipolaron mechanism for bias-stress effects in polymer transistors, Phys. Rev. B. 68 (2003) 085316. doi:10.1103/PhysRevB.68.085316.

[68] M. Tsuji, Y. Takahashi, Y. Sakurai, Y. Yomogida, T. Takenobu, Y. Iwasa, K. Marumoto, Two-dimensional magnetic interactions and magnetism of high-density charges in a polymer transistor, Appl. Phys. Lett. 102 (2013) 133301. doi:10.1063/1.4800550.

[69] G. Zotti, S. Zecchin, G. Schiavon, B. Vercelli, A. Berlin, E. Dalcanale, L. “Bert” Groenendaal, Potential-driven conductivity of polypyrroles, poly-N-alkylpyrroles, and polythiophenes: role of the pyrrole NH moiety in the doping-charge dependence of conductivity, Chem. Mater. 15 (2003) 4642–4650. doi:10.1021/CM030336I.

[70] K. Fesser, A.R. Bishop, D.K. Campbell, Optical absorption from polarons in a model of polyacetylene, Phys. Rev. B. 27 (1983) 4804–4825. doi:10.1103/PhysRevB.27.4804.

[71] T.-C. Chung, J.H. Kaufman, A.J. Heeger, F. Wudl, Charge storage in doped poly(thiophene): Optical and electrochemical studies, Phys. Rev. B. 30 (1984) 702–710.

doi:10.1103/PhysRevB.30.702.

[72] J. Chen, A.J. Heeger, F. Wudl, Confined soliton pairs (bipolarons) in polythiophene: In-situ magnetic resonance measurements, Solid State Commun. 58 (1986) 251–257. doi:10.1016/0038-1098(86)90212-7.

[73] A.J. Heeger, S. Kivelson, J.R. Schrieffer, W.-P. Su, Solitons in conducting polymers, Rev. Mod. Phys. 60 (1988) 781–850. doi:10.1103/RevModPhys.60.781.

[74] Y. Furukawa, Electronic absorption and vibrational spectroscopies of conjugated conducting polymers, J. Phys. Chem. 100 (1996) 15644–15653. doi:10.1021/JP960608N.

[75] N. Yokonuma, Y. Furukawa, M. Tasumi, M. Kuroda, J. Nakayama, Electronic absorption and Raman studies of $BF4^-$-doped polythiophene based on the spectra of the radical cation and dication of α-sexithiophene, Chem. Phys. Lett. 255 (1996) 431–436. doi:10.1016/0009-2614(96)00383-1.

[76] Y. Furukawa, N. Yokonuma, M. Tasumi, M. Kuroda, J. Nakayama, Raman studies of doped polythiophene and the radical cation and dication of quinquethiophene, Mol. Cryst. Liq. Cryst. Sci. Technol. Sect. A. Mol. Cryst. Liq. Cryst. 256 (1994) 113–120. doi:10.1080/10587259408039238.

[77] Y. Shimoi, S. Abe, K. Harigaya, Theory of optical absorption in doped conjugated polymers, Mol. Cryst. Liq. Cryst. Sci. Technol. Sect. A. Mol. Cryst. Liq. Cryst. 267 (1995) 329–334. doi:10.1080/10587259508034012.

[78] G. Zerbi, C. Castiglioni, M. Gussoni, Understanding of vibrational spectra of polyconjugated molecules by means of the “effective conjugation coordinate,” Synth. Met. 43 (1991) 3407–3412. doi:10.1016/0379-6779(91)91315-2.

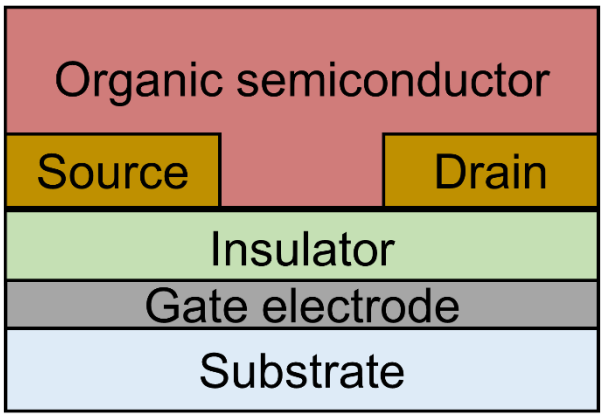

Figure 1.1. The device structure of the bottom contact/bottom gate

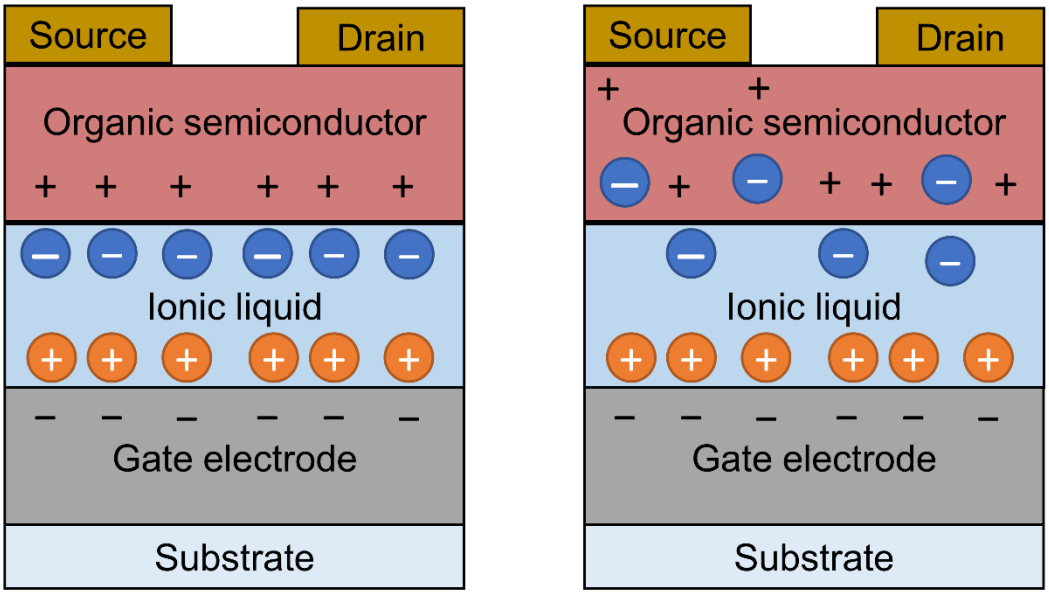

Figure1.2. Electrostatic (left) and electrochemical (right) doping

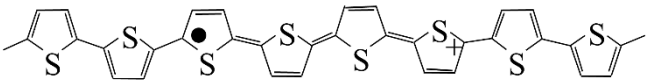

Polaron

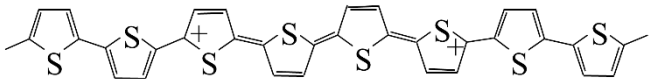

Bipolaron

Figure 1.3. The schematic structures of a polaron and a bipolaron in polythiophene

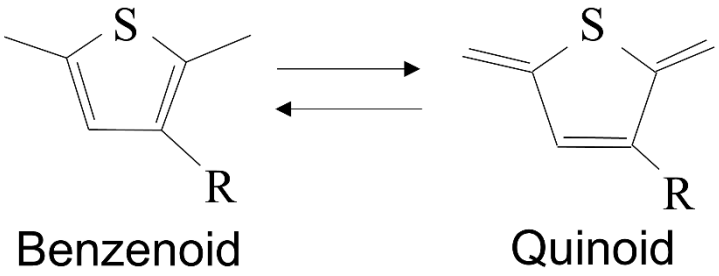

Figure 1.4. The benzenoid and quinoid structures

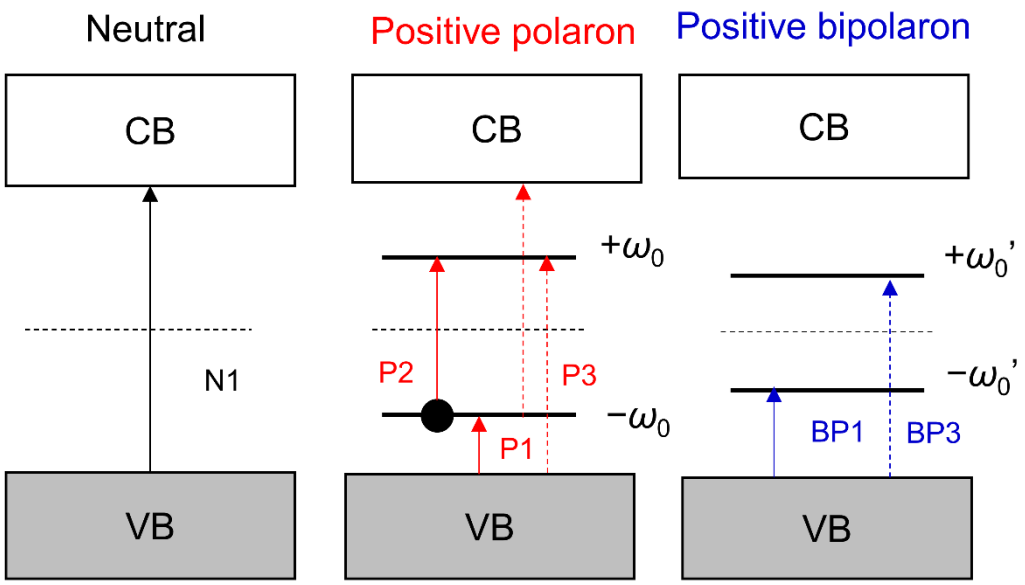

Figure 1.5. Schematic electronic structure of a neutral polymer, a positive polaron and a positive bipolaron

Chapter 2

Study on carriers of PBTTT-C14 generated in an ILGT using Raman spectroscopy

2.1 Introduction

In this chapter, I investigate an ILGT fabricated with PBTTT-C14 as the active layer and [BMIM][TFSI] as the ionic liquid using Raman and electrochemical measurements. The chemical structures of PBTTT-C14 and [BMIM][TFSI] are shown in Figure 2.1.

PBTTT is a conjugated polymer that acts as a p-type semiconductor with positive polarons and bipolarons as carriers upon oxidation [1–8]. It is widely used for organic devices such as a solar cell, a spintronic device, a thermoelectric device and a transistor [9–11]. This compound has two thiophene rings and one thienothiophene ring as a repeating unit. In a design of organic conjugated polymer, HOMO level is an important factor for improvement in oxidative stability. PBTTT has a thienothiophene unit that has a larger resonance stabilization energy than a single thiophene unit. It reduces delocalization of electrons into the backbone. This molecular design resulted in a lower HOMO level (5.1 eV) [12] than that of with P3HT (4.8 eV) [13]. In addition, a crystalline domain is also important because crystalline domains allow short intermolecular π-π distance, which allows high mobility. Thienothiophene ring is a linear conjugated comonomer unit and promotes a higher degree of order and generating large crystalline domains. A large positive carrier mobility (1 $cm^2 s^{-1} V^{-1}$) can thus be achieved in an OTFT [3]. PBTTT molecules are aligned in an edge-on orientation, allowing current to easily flow in the lateral direction. The source and drain electrodes are patterned laterally in most transistors as shown in Figure 1.1, and the I_D flows in this direction. Therefore, PBTTT is suitable for use as an active layer in transistors.

Raman spectroscopy is a powerful tool for detecting carrier species [14–17]. Carrier generation in the channel region of ILGTs can be detected in situ using this technique. The I_D and I_G can be determined using electrical measurements. Electrical conductivity can be calculated from I_D and V_D, and resulted in a higher degree of order, generating crystalline domains, and the injected charge density can be calculated from the integral of I_G. The mobility of each carrier and the critical doping level of carrier generation can be determined by comparison of the Raman spectra.

The Raman spectra of the polarons and bipolarons of PBTTT-C14 have not been elucidated. Therefore, the carrier species should be identified using optical absorption spectroscopy. Polarons have two intense absorption bands, and bipolarons have one intense absorption band based on theoretical models under the one-electron approximation [18,19]. A PBTTT-C14 film doped with $FeCl_3$ was evaluated with both optical absorption spectroscopy and Raman spectroscopy to

identify the Raman bands of the polarons and bipolarons. I obtain the relation between the carrier generation in the ILGT and the mobilities, conductivities and doping levels based on Raman spectroscopy and electrochemical measurements.

2.2 Experimental methods

2.2.1 Materials and devices

PBTTT-C14 was purchased from Lumtec (Hsin-Chu, Taiwan). [BMIM][TFSI], $FeCl_3$ and 1,2-dichlorobenzene were purchased from Kanto Chemical. EAGLE XG® glass substrate (20×20×0.7 mm) was purchased from Corning. A schematic of the structure of the ILGT devices used in this work is shown in Figure 2.2. Ni (5 nm) and Au (45 nm) were deposited using a shadow mask on the glass substrate as the source and drain electrodes. The width and length of the channel region were 1 mm and 50 μm, respectively. A PBTTT-C14 film was prepared from a solution of 1,2-dichlorobenze (15 mg/mL, at 90 °C) using a spin-coating method. The film was not annealed. The thickness of the film was measured to be 60 nm using a Bruker AXS Dektak XT surface profilometer. [BMIM][TFSI] was used as the gate dielectric. The thickness of the dielectric layer was 200 μm using a Naflon® (polytetrafluoroethylene) spacer purchased from NICHIAS. A glass substrate coated with ITO was purchased from GEOMATEC. The sheet resistivity was 30 $\Omega\ sq^{-1}$. The ITO-coated glass substrate was used as the gate electrode.

2.2.2 $FeCl_3$ vapor doping

A PBTTT-C14 film was doped by exposure to $FeCl_3$ vapor at reduced pressure using a cell as shown in Figure 2.3. The PBTTT-C14 film was formed on a BaF_2 window of the cell by spin coating. Solid $FeCl_3$ powder was placed in the cell. The Vis/NIR absorption spectra were obtained using a JASCO V-570 UV/Vis/NIR spectrometer. Raman spectra were obtained using a Renishaw InVia Raman microscope with a Leica N PLAN L 50× objective (working distance, 8.2 mm; numerical aperture, 0.50) with an excitation wavelength of 785 nm. The spatial resolution was 2.8 cm^{-1}.

2.2.3 Raman and electrochemical measurements of an ILGT

Raman and electrochemical measurements were performed on the same ILGT (Figure 2.4). Raman measurements were performed under the conditions described in Section 2.2.2. V_D was applied, and I_D was measured using a KEITHLEY 6487 picoammeter/voltage source. V_G was applied, and I_G was measured using an ADVANTEST R6243DC current monitor/voltage source. V_D was fixed at −0.01 V. The dependence of the Raman spectrum on V_G was measured from V_G = 0 to −2.0 V every −0.1 V, and measurements were taken 30 s after the change in the V_G. The change in I_G as a function of time (Figure 2.5) was integrated over 200 s starting from the change in V_G; the current after 200 s was considered I_L. I_D was also measured after 200 s. Thus, the stepwise injection charge was obtained. The injected charge (Q) at V_G was the sum of the stepwise injected charges. The charge density (n) can be evaluated from the following equation:

$$n = \frac{1}{eSd}\int (I_G - I_L)dt = \frac{Q}{eSd} \tag{2.1}$$

where e is the elementary charge, and S and d are the area and the thickness of the PBTTT-C14 film, respectively. Based on the XRD data, the lattice parameters of the unit cell of a PBTTT-C14 triclinic crystal are a = 2.15 nm, b = 0.54 nm, c = 1.35 nm, α = 137°, β = 86°, γ = 89°, and Z = 1 [20]. The number of repeating units per unit volume N (9.43×10^{20} cm^{-3}) was calculated from these values. The number of π electrons in one unit of PBTTT-C14 was 14. The doping level per π electron x (%/π electron) was calculated by the following equation:

$$x = \frac{n}{14N} \times 100 \tag{2.2}$$

The average electrical conductivity (σ) of PBTTT-C14 at each V_G value was calculated from I_D, V_D = −0.01 V, the width of the channel (W = 1.0 mm), the length of the channel (L = 5.0×10 μm) and the thickness of the film (d = 5.0×10 nm). The mobility (μ) was obtained using the following equation:

$$\mu = \frac{\sigma}{pq} \tag{2.3}$$

The carrier density (p) is n for polarons and $n/2$ for bipolarons, and the charge of a carrier (q) is $+e$ for polarons and $+2e$ for bipolarons.

2.3 Results and discussion

2.3.1 Vis-NIR absorption and Raman spectra of a PBTTT-C14 film doped with $FeCl_3$

Figure 2.6 shows changes in the optical spectra of a PBTTT-C14 film upon $FeCl_3$ doping. The dopants penetrate the film more deeply with increasing doping time. A pristine PBTTT-C14 film shows a band at 2.37 eV. Upon $FeCl_3$ doping, the intensity of the 2.37-eV band decreases, and two new bands appear at approximately 1.52 eV and in the NIR range extending into the infrared region. After 120 min of doping, the band at 1.52 eV is the most intense. After 140 min, the intensity of the band in the NIR region had increased further, while the intensity of the 1.52-eV band had decreased. After 270 min, the band at 1.52 eV had disappeared. These spectral changes can be explained based on the electronic-level diagrams of a positive polaron and a positive bipolaron in the one-electron picture shown in Figure 2.7. The 2.37-eV band observed for the pristine PBTTT-C14 film originates from the π-π* transition (N1). When a positive polaron forms, two localized electronic levels are generated (+ε and −ε). Therefore, two strong transitions, P1 and P2, are observed. The 1.52-eV band is attributed to P2, and the band in the NIR region is attributed to P1. The positive bipolaron has only one strong band, BP1. The NIR band that appears after 270 min is attributed to BP1. These results indicate that polarons form in the early doping stage, and bipolarons form after 140 min, as evidenced by the decrease in the intensity of the 1.52-eV band. After 270 min, bipolarons are the dominant species, as evidenced by the absence of the 1.52-eV band, although a small number of polarons may exist because it is difficult to separate the remaining 1.52-eV band into the components of bipolarons and polarons.

The 785-nm excited Raman spectra of PBTTT-C14 were obtained at the same time as the optical absorption spectra. Figure 2.8 shows changes in the Raman spectra of the PBTTT-C14 film upon $FeCl_3$ doping. The excitation wavelength of 785 nm (1.58 eV) is located within the polaron absorption band (1.52 eV). Notably, the intensities of the Raman bands of the polarons

are enhanced by the resonance Raman effect. The Raman spectrum of the pristine PBTTT-C14 film exhibits intense bands at 1490, 1457, 1412 and 1391 cm^{-1}. The 1412-cm^{-1} band is assigned to the C=C stretching vibration of the thienothiophene ring. The 1490- and 1391-cm^{-1} bands are assigned to the C=C and C−C stretching vibrations of the thiophene ring, respectively [21]. The observed Raman spectra can be attributed to polarons and/or bipolarons based on the results of the optical absorption spectra. After 10 min, the Raman spectrum changed substantially. The spectrum shows intense bands at 1452, 1381, 1210, 744, 698 and 638 cm^{-1}. These bands are attributed to polarons. Carriers observed in the first 120 min of doping are attributed to polarons. The bands at 1452 and 1381 cm^{-1} show small downward shifts and changes in their relative intensities. These downward shifts originate from increasing the effective conjugation and/or making the polaron pair [22]. At 140 min of doping, the spectrum shows bands at 1446, 1374, 1210, 741, 699 and 637 cm^{-1}. The spectra change with increasing doping time. At 270 min, the spectrum shows bands at 1434, 1362, 1208, 738, 694 and 635 cm^{-1}. These bands are attributed to bipolarons. These bands show small downward shifts from those of polarons. These downward shifts originate from decreasing chain length and decreasing the force constants associated the C=C and C−C [20]. It is because it reduces a bond order when the π electron is removed from C=C. These results indicate that the Raman spectral features between 1500 and 1300 cm^{-1} can be used to identify the types of carriers in PBTTT-C14.

2.3.2 Raman spectra of an ILGT

Figure 2.9 shows the changes in the Raman spectra of an ILGT as a function of $-V_G$ from 0.0 to 2.0 V. The spectrum acquired at $-V_G$ = 0.0 V shows intense bands at 1488, 1413 and 1391 cm^{-1}. These bands are attributed to neutral PBTTT-C14 polymers, and other bands observed in the spectrum are attributed to [BMIM][TFSI] as marking the star in Figure 2.9. The intensity of the 1391-cm^{-1} band at $-V_G$ = 0.9 V increases dramatically. The spectra acquired at $-V_G$ = 0.9 and 1.1 V show a mixture of neutral species and polarons. At $-V_G$ = 1.3 V, the features of the spectrum are attributed to polarons because this spectrum is quite similar to that of the polarons generated by $FeCl_3$ doping shown in Figure 2.8. The spectra acquired between $-V_G$ = 1.4 and 1.7 V show a mixture of polarons and bipolarons. The features of the spectra acquired above $-V_G$ = 1.8 V are attributed to bipolarons. Accordingly, polarons form below $-V_G$ = 1.3 V; polarons and bipolarons coexist between $-V_G$ = 1.4 and 1.7 V, and bipolarons are dominant above $-V_G$ = 1.8 V.

2.3.3 Electrical properties of an ILGT

The relationship between I_D and V_G at $V_D = -0.01$ V for an ILGT is shown in Figure 2.10. In the $-V_G$ range of 0.0 to 1.1 V, $-I_D$ increases gradually. On the other hand, $-I_D$ increases rapidly from 1.1 to 1.6 V. Initially, PBTTT-C14 is electrostatically doped by the EDL. Above 1.1 V, anions penetrate into the PBTTT-C14 film and the electrochemical doping occurs. The maximum value of $-I_D$ is reached at 1.9 V. The σ values were calculated from these values of I_D and V_D. The values of n and x were calculated from Q. The relationship between n and $-V_G$ is shown in Figure 2.11, and the relationship between x and $-V_G$ is shown in Figure 2.12. The values of σ and μ are plotted against x in Figure 2.13. The σ values increase gradually from $x = 0$ to 0.69% and then increase rapidly when x is greater than 1.0%. The maximum value of σ (62.2 S cm^{-1}) was observed at x = 9.4%. Based on the Raman results, polarons form below $x = 1.5\%$, and bipolarons start to form at $x = 3.0\%$. Above $x = 8.2\%$, bipolarons are dominant. The μ values of the polarons are strongly dependent on x, and they increase with increasing x. The μ values of the bipolarons decrease slightly with increasing x. The highest μ value of the polarons (4.2×10^{-2} cm^2 V^{-1} s^{-1}) was observed at $x = 1.5\%$ and $n = 2.0 \times 10^{20}$ cm^{-3} ($-V_G = 1.3$ V). The highest μ value of the bipolarons (0.36 cm^2 V^{-1} s^{-1}) was observed at $x = 8.2\%$ and $n = 1.1 \times 10^{21}$ cm^{-3} ($-V_G = 1.8$ V). It has been reported that the bipolaron mobility in P3HT is 2.5×10^{-3} cm^2 V^{-1} s^{-1}, and bipolarons of P3HT decrease the conductivity of transistors because of their low mobility [16]. However, the bipolarons of PBTTT-C14 show high mobilities, indicating that both polarons and bipolarons can serve as effective carriers.

2.4 Conclusion

Optical absorption and Raman spectra of polarons and bipolarons formed in a PBTTT-C14 film by $FeCl_3$ vapor doping were measured. The Raman spectra of polarons and bipolarons were elucidated based on the assignment of their optical absorption spectra. The electrical conductivities and doping levels were obtained from electrochemical measurements of the ILGT fabricated with PBTTT-C14. The type of carriers formed in the ILGT as a function of the doping level was elucidated using Raman spectroscopy.

Polarons form below x = 1.5%, and bipolarons start to form at x = 3.0%. Above x = 8.2%, bipolarons are the dominant species. The highest μ value of the polarons (4.2×10^{-2} cm^2 V^{-1} s^{-1}) was observed at x = 1.5% and $n = 2.0 \times 10^{20}$ cm^{-3} ($-V_G$ = 1.3 V). The highest μ value of the bipolarons (0.36 cm^2 V^{-1} s^{-1}) was observed at x = 8.2% and $n = 1.1 \times 10^{21}$ cm^{-3} ($-V_G$ = 1.8 V). Bipolarons of PBTTT-C14 show high mobilities, whereas bipolarons of P3HT show low mobilities. It indicates that a bipolaron can be also used as an effective carrier.

The combination of Raman spectroscopy and electrochemical measurements is useful for investigating carriers in ILGTs fabricated with organic polymers. The critical doping level of the polaron-to-bipolaron transition and the dependence of the mobilities on the doping levels can be determined using this method.

2.5 References

[1] A. de la Fuente Vornbrock, D. Sung, H. Kang, R. Kitsomboonloha, V. Subramanian, Fully gravure and ink-jet printed high speed pBTTT organic thin film transistors, Org. Electron. 11 (2010) 2037–2044. doi:10.1016/J.ORGEL.2010.09.003.

[2] H. Tanaka, S. Nishio, H. Ito, S. Kuroda, Microscopic signature of insulator-to-metal transition in highly doped semicrystalline conducting polymers in ionic-liquid-gated transistors, Appl. Phys. Lett. 107 (2015) 243302. doi:10.1063/1.4938137.

[3] T. Umeda, D. Kumaki, S. Tokito, Surface-energy-dependent field-effect mobilities up to 1 cm^2/V s for polymer thin-film transistor, J. Appl. Phys. 105 (2009) 024516. doi:10.1063/1.3072669.

[4] T. Umeda, S. Tokito, D. Kumaki, High-mobility and air-stable organic thin-film transistors with highly ordered semiconducting polymer films, J. Appl. Phys. 101 (2007) 054517. doi:10.1063/1.2711780.

[5] H. Ito, T. Harada, H. Tanaka, S. Kuroda, Critical regime for the insulator-metal transition in highly ordered conjugated polymers gated with ionic liquid, Jpn. J. Appl. Phys. 55 (2016) 03DC08. doi:10.7567/JJAP.55.03DC08.

[6] T. Harada, H. Ito, Y. Ando, S. Watanabe, H. Tanaka, S. Kuroda, Signature of the insulator-metal transition of a semicrystalline conjugated polymer in ionic-liquid-gated transistors, Appl. Phys. Express. 8 (2015) 021601. doi:10.7567/APEX.8.021601.

[7] C. Wang, L.H. Jimison, L. Goris, I. McCulloch, M. Heeney, A. Ziegler, A. Salleo, Microstructural origin of high mobility in high-performance poly(thieno-thiophene) thin-film transistors, Adv. Mater. 22 (2010) 697–701. doi:10.1002/adma.200902303.

[8] N. Zhao, Y.-Y. Noh, J.-F. Chang, M. Heeney, I. McCulloch, H. Sirringhaus, Polaron localization at interfaces in high-mobility microcrystalline conjugated polymers, Adv. Mater. 21 (2009) 3759–3763. doi:10.1002/adma.200900326.

[9] A.C. Mayer, M.F. Toney, S.R. Scully, J. Rivnay, C.J. Brabec, M. Scharber, M. Koppe, M. Heeney, I. McCulloch, M.D. McGehee, Bimolecular crystals of fullerenes in conjugated polymers and the implications of molecular mixing for solar cells, Adv. Funct. Mater. 19 (2009) 1173–1179. doi:10.1002/adfm.200801684.

[10] Q. Zhang, Y. Sun, F. Jiao, J. Zhang, W. Xu, D. Zhu, Effects of structural order in the pristine state on the thermoelectric power-factor of doped PBTTT films, Synth. Met. 162

(2012) 788–793. doi:10.1016/J.SYNTHMET.2012.03.003.

[11] S. Watanabe, K. Ando, K. Kang, S. Mooser, Y. Vaynzof, H. Kurebayashi, E. Saitoh, H. Sirringhaus, Polaron spin current transport in organic semiconductors, Nat. Phys. 10 (2014) 308–313. doi:10.1038/nphys2901.

[12] I. McCulloch, M. Heeney, C. Bailey, K. Genevicius, I. MacDonald, M. Shkunov, D. Sparrowe, S. Tierney, R. Wagner, W. Zhang, M.L. Chabinyc, R.J. Kline, M.D. McGehee, M.F. Toney, Liquid-crystalline semiconducting polymers with high charge-carrier mobility, Nat. Mater. 5 (2006) 328–333. doi:10.1038/nmat1612.

[13] S. Holliday, J.E. Donaghey, I. McCulloch, Advances in charge carrier mobilities of semiconducting polymers used in organic transistors, Chem. Mater. 26 (2014) 647–663. doi:10.1021/cm402421p.

[14] C. Francis, D. Fazzi, S.B. Grimm, F. Paulus, S. Beck, S. Hillebrandt, A. Pucci, J. Zaumseil, Raman spectroscopy and microscopy of electrochemically and chemically doped high-mobility semiconducting polymers, J. Mater. Chem. C. 5 (2017) 6176–6184. doi:10.1039/C7TC01277B.

[15] Y. Wada, I. Enokida, J. Yamamoto, Y. Furukawa, Raman imaging of carrier distribution in the channel of an ionic liquid-gated transistor fabricated with regioregular poly(3-hexylthiophene), Spectrochim. Acta Part A Mol. Biomol. Spectrosc. 197 (2018) 166–169. doi:10.1016/J.SAA.2018.01.043.

[16] J. Yamamoto, Y. Furukawa, Raman characterization and electrical properties of poly(3-hexylthiophene) doped electrochemically in an ionic liquid-gated transistor geometry, Org. Electron. 28 (2016) 82–87. doi:10.1016/J.ORGEL.2015.10.016.

[17] Y. Furukawa, Electronic absorption and vibrational spectroscopies of conjugated conducting polymers, J. Phys. Chem. 100 (1996) 15644–15653. doi:10.1021/JP960608N.

[18] Y. Shimoi, S. Abe, K. Harigaya, Theory of optical absorption in doped conjugated polymers, Mol. Cryst. Liq. Cryst. Sci. Technol. Sect. A. Mol. Cryst. Liq. Cryst. 267 (1995) 329–334. doi:10.1080/10587259508034012.

[19] K. Fesser, A.R. Bishop, D.K. Campbell, Optical absorption from polarons in a model of polyacetylene, Phys. Rev. B. 27 (1983) 4804–4825. doi:10.1103/PhysRevB.27.4804.

[20] E. Cho, C. Risko, D. Kim, R. Gysel, N. Cates Miller, D.W. Breiby, M.D. McGehee, M.F. Toney, R.J. Kline, J.-L. Bredas, Three-dimensional packing structure and electronic

properties of biaxially oriented poly(2,5-bis(3-alkylthiophene-2-yl)thieno[3,2-*b*]thiophene) films, J. Am. Chem. Soc. 134 (2012) 6177–6190. doi:10.1021/ja210272z.

[21] J. Gao, A.K. Thomas, R. Johnson, H. Guo, J.K. Grey, Spatially resolving ordered and disordered conformers and photocurrent generation in intercalated conjugated polymer/fullerene blend solar cells, Chem. Mater. 26 (2014) 4395–4404. doi:10.1021/cm501252y.

[22] G. Zerbi, C. Castiglioni, M. Gussoni, Understanding of vibrational spectra of polyconjugated molecules by means of the “effective conjugation coordinate,” Synth. Met. 43 (1991) 3407–3412. doi:10.1016/0379-6779(91)91315-2.

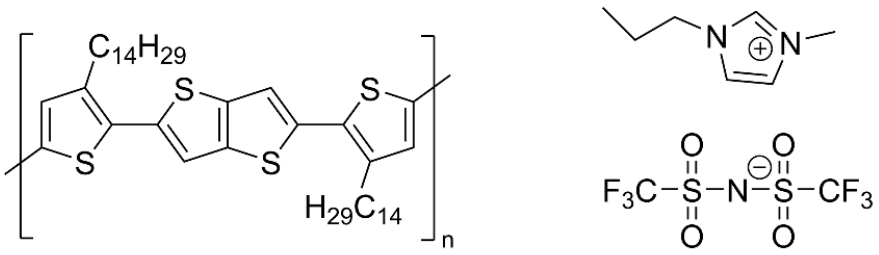

PBTTT-C14 [BMIM][TFSI]

Figure 2.1. Chemical structures

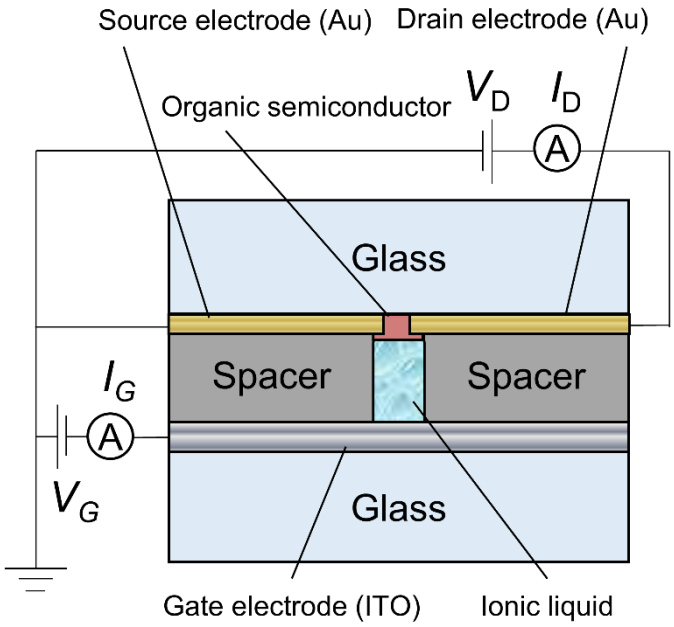

Figure 2.2. Schematic of an ILGT device

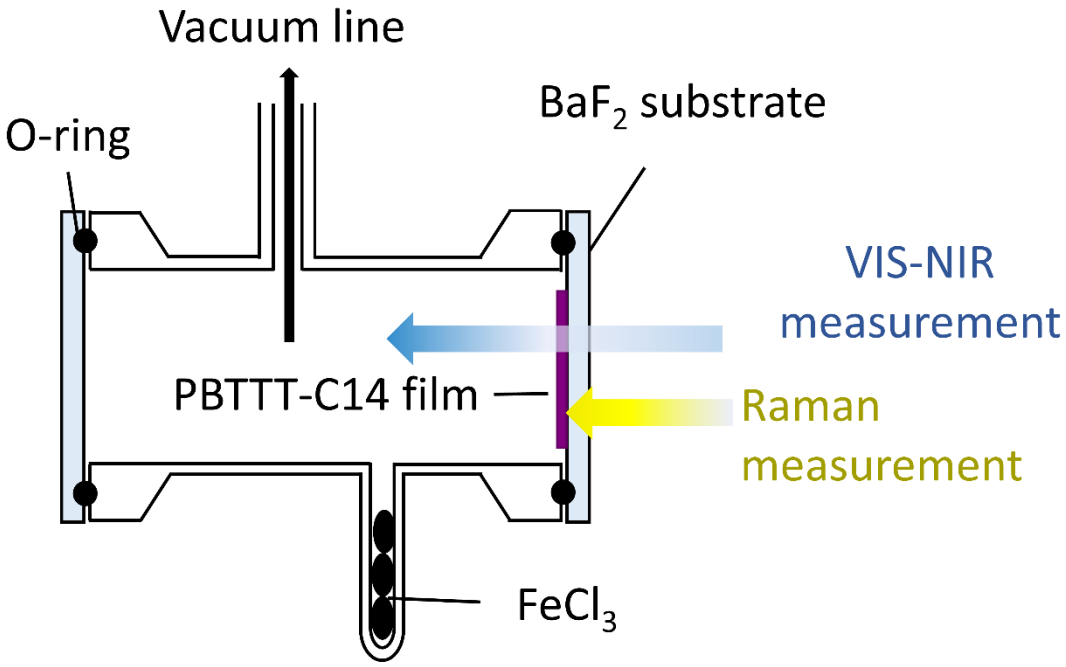

Figure 2.3. The cell for chemical vapor doping

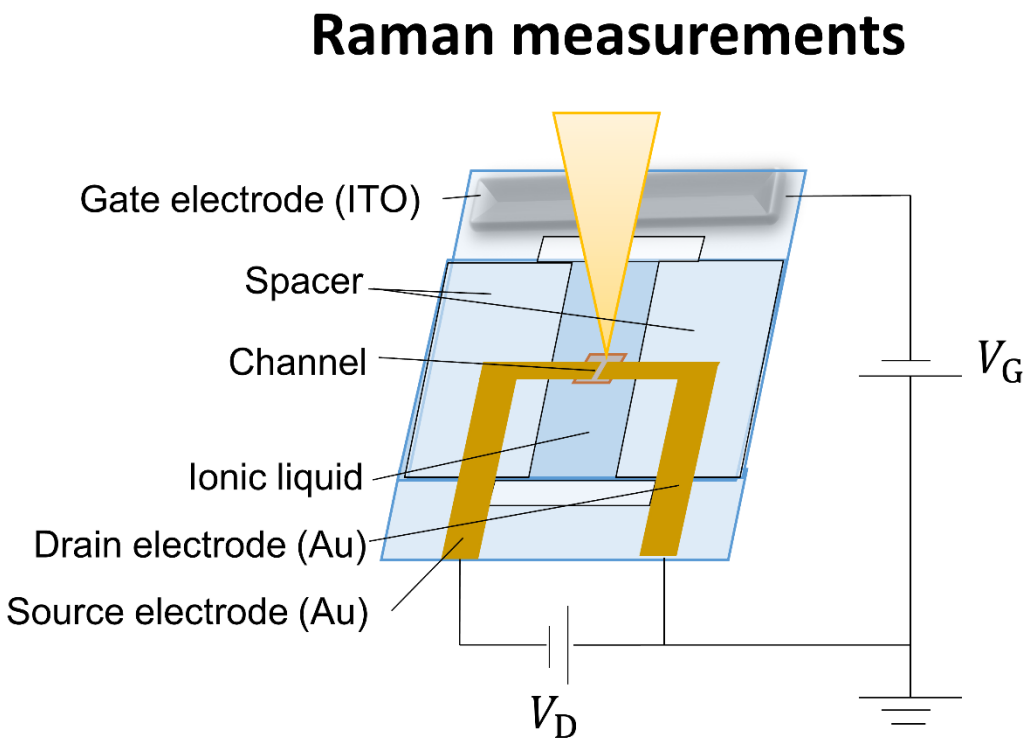

Figure 2.4. Raman measurements in the channel region with electrochemical measurements

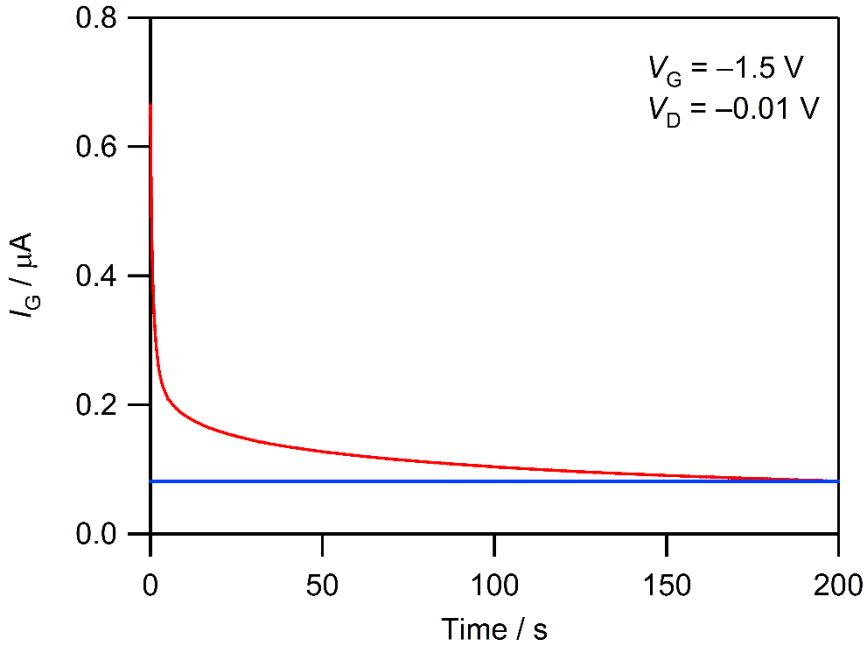

Figure 2.5. I_G as a function of time

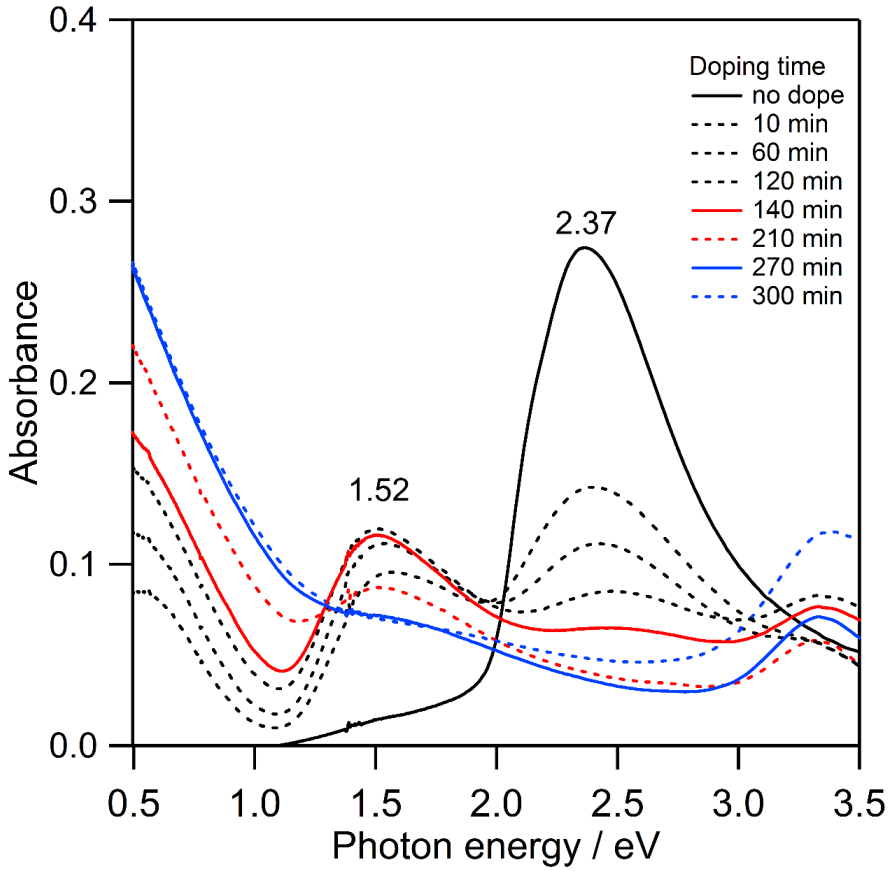

Figure 2.6. Changes in the Vis-NIR absorption spectra of a PBTTT-C14 film doped with $FeCl_3$

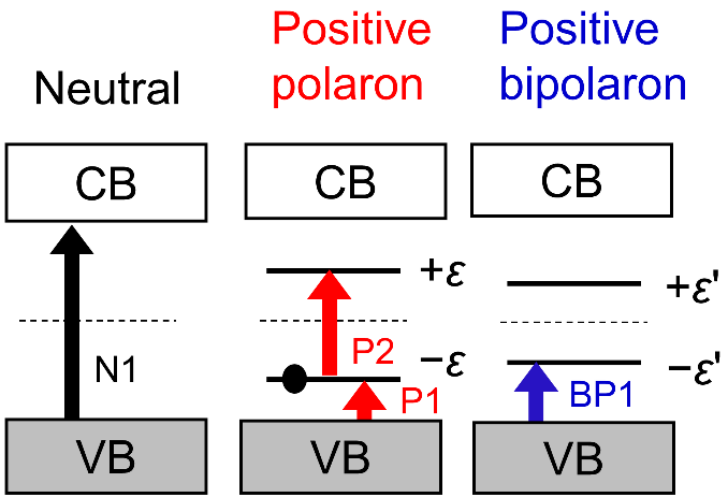

Figure 2.7. Configurations of the electron levels of a neutral conjugated polymer, a positive polaron and a positive bipolaron

(CB and VB denote the conduction band and valence band, respectively)

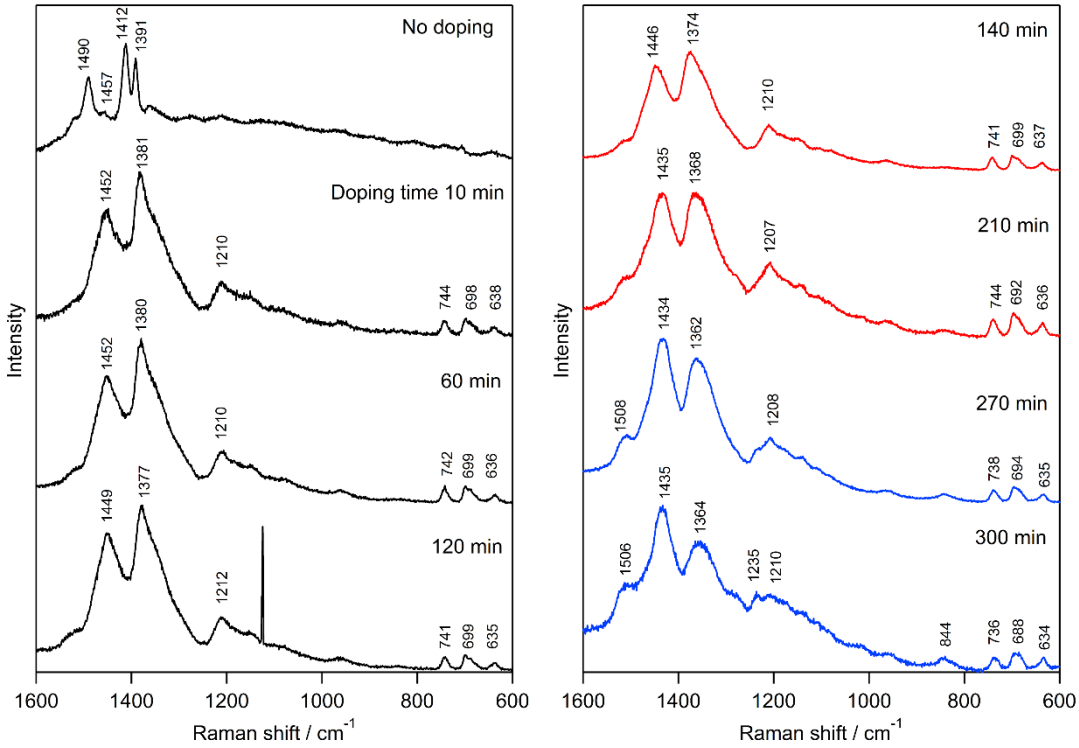

Figure 2.8. Changes in the Raman spectra of a PBTTT-C14 film upon doping with $FeCl_3$

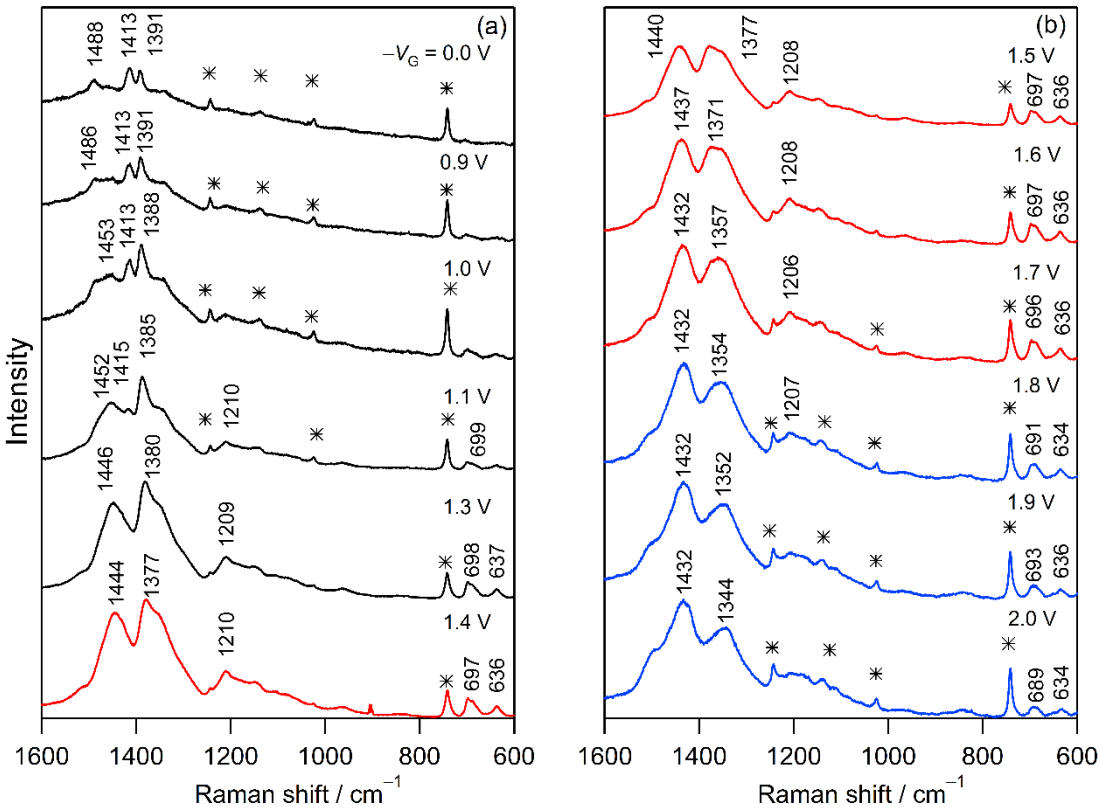

Figure 2.9. Changes in the Raman spectra of an ILGT fabricated with PBTTT-C14

(* indicates the bands of the ionic liquids)

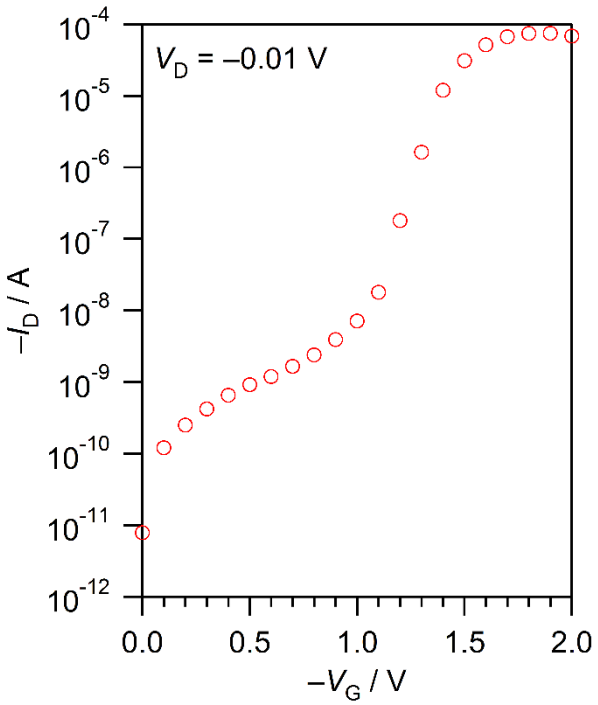

Figure 2.10. Transfer characteristics of an ILGT fabricated with PBTTT-C14

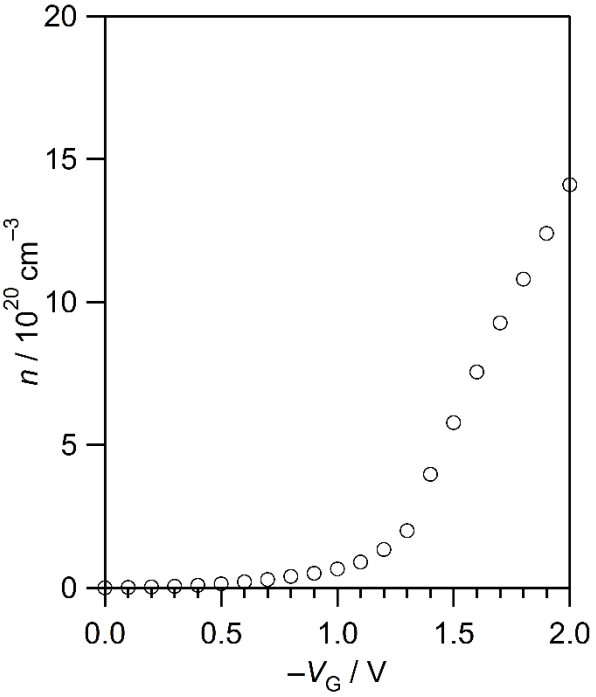

Figure 2.11. Plots of n versus $-V_G$ for an ILGT fabricated with PBTTT-C14

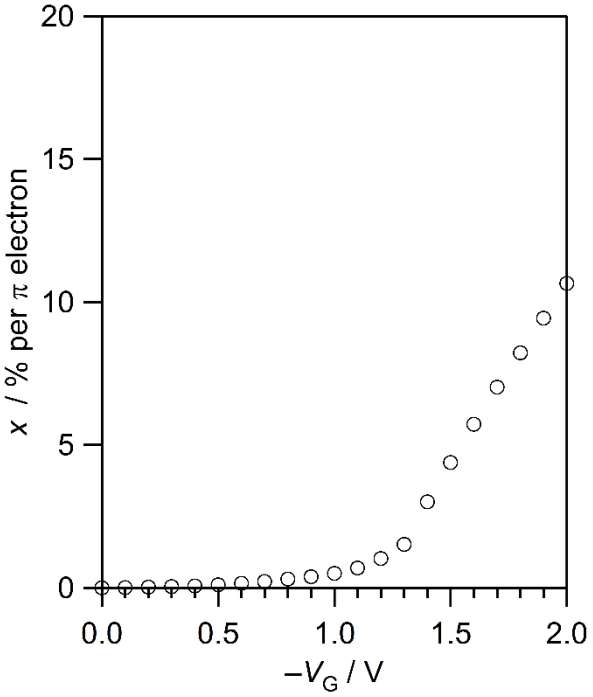

Figure 2.12. Plots of x versus $-V_G$ for an ILGT fabricated with PBTTT-C14

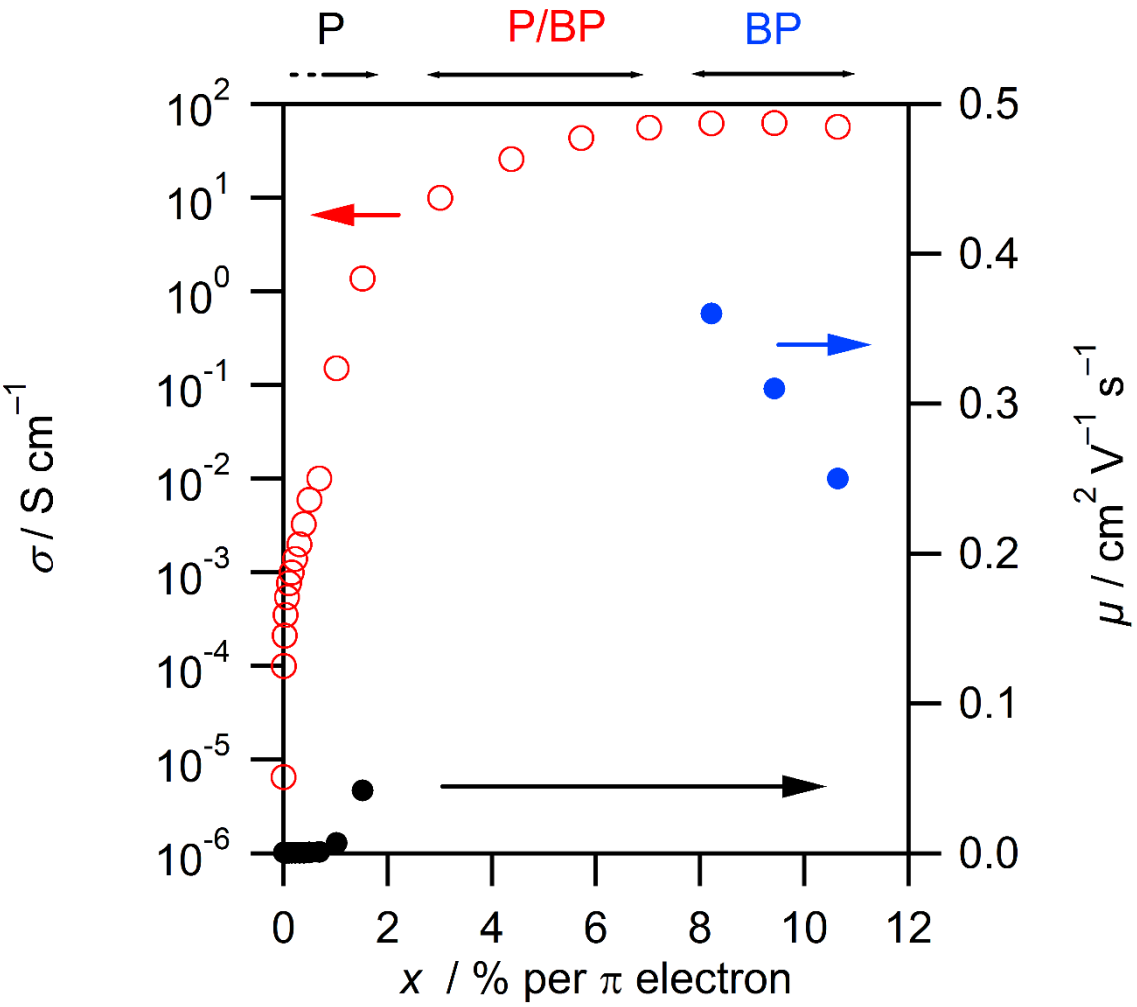

Figure 2.13. Plots of σ and μ versus x for an ILGT fabricated with PBTTT-C14

Chapter 3

Study on the effect of annealing on carriers of PBTTT-C16 generated in ILGTs

3.1 Introduction

In this chapter, ILGTs fabricated with unannealed and annealed PBTTT-C16 films as the active layer and [BMIM][TFSI] as the ionic liquid were investigated using Raman and electrochemical measurements.

Thermal annealing is a common method for improving the properties of organic devices because it alters the solid structure [1–3]. PBTTT-C16 has long side chains and good solubility (Figure 3.1), making it suitable for the fabrication of transistors by wet processing [4–8]. PBTTT has two endotherms on heating and two exotherms on cooling [9]. PBTTT-C16 undergoes phase transitions to a liquid crystalline phase (smectic liquid crystal) above 130 °C and to an isotropic phase (liquid) above 235 °C [10]. The crystallinity of the polymer is increased by heating above the phase-transition temperature and slow cooling to room temperature. In addition, the different heating above 130 and 235 °C exhibits a change of a surface topology as a terrace and a ribbon shape, respectively [4,11]. The morphological changes in PBTTT improve the mobility of transistors [4,10,12,13].

The stability of the carriers is associated with the electron-lattice interactions and the electron-electron interaction in a single chain as the basic theory [14,15]. However, the effect of interchain coupling is also important for the stability of carriers [16]. Therefore, the solid structures of conjugated polymers affect the carrier stabilities. In ILGTs, the doping mechanism, which includes penetration of anions into the active layer, is different from that of OFETs. The penetrating anions also affect the stability of carriers as a counter ion [17]. Therefore, the structural changes of not only the surface topology but also inside the film have a great influence on the generation of carriers.

Raman spectroscopy can be used not only to identify the carrier species but also to evaluate the crystalline contents of an organic semiconductor film. The band of PBTTT-C16 was deconvoluted into two bands attributable to the crystalline and amorphous regions, which can be used to evaluate the overall crystalline contents. For the carrier identification, the Raman spectra of the polarons and bipolarons of PBTTT-C16 must be elucidated. Therefore, the optical absorption and Raman spectra of a PBTTT-C16 film doped with $FeCl_3$ were acquired to identify the Raman spectra of the polarons and bipolarons, as described in Chapter 2. Carrier generation in ILGTs was observed using Raman spectroscopy, and the mobility of each carrier and the critical doping level of the polaron-to-bipolaron transition can be determined from electrochemical measurements. I discuss the relationship between the types of carriers generated in the ILGTs fabricated with unannealed and annealed PBTTT-C16 films and mobilities, conductivities and doping levels for carrier generation.

3.2 Experimental methods

3.2.1 Materials and devices

Lisicon SP210® (PBTTT-C16) was purchased from Merck and used as received. [BMIM][TFSI], $FeCl_3$, and 1,2-dichlorobenzene were purchased from Kanto Chemical. EAGLE XG® glass substrates (20×20×0.7 mm) were purchased from Coring. The structure of the ILGT is the same as what is shown in Figure 2.2. Ni (5 nm) and Au (45 nm) were deposited on the glass substrate as the source and drain electrodes using a shadow mask. The width and length of the channel were 1 mm and 50 μm, respectively. PBTTT-C16 films were prepared from a solution of 1,2-dichlorobenzene (12 mg/mL, at 90 °C) using spin coating. The thickness of the film was measured using a Bruker AXS Dektak XT surface profilometer, and it was 5.0×10 nm. The as-prepared film was annealed at 235 °C for 20 min under vacuum. XRD patterns were measured using a Rigaku RINT-Ultima III X-ray diffractometer. AFM images were acquired using a Digital Instruments Nanoscope IIIa microscope. [BMIM][TFSI] was used as the gate dielectric. The thickness of the ionic-liquid layer was 200 μm using a Naflon® (polytetrafluoroethylene) spacer purchased from NICHIAS. An ITO-coated glass substrate with a sheet resistivity of 30 $\Omega\ sq^{-1}$ was purchased from GEOMATEC. The surface of the ITO-coated glass substrate was cleaned with UV-ozone plasma treatment and used as the gate electrode.

3.2.2 Raman measurements of annealed PBTTT-C16 films

The quartz substrate was cleaned by sonication in an aqueous detergent solution, pure water, acetone, and then isopropyl alcohol for 5 min each, followed by UV/ozone treatment for 30 min. PBTTT-C16 films were fabricated on the quartz substrate. The films were thermally annealed at 180, 235 and 250 °C for 20 min under vacuum. Raman spectra were obtained using a Renishaw InVia Raman microscope with a Leica N PLAN L 50× objective (working distance, 8.2 mm; numerical aperture, 0.50) with an excitation wavelength of 785 nm. The spatial resolution was 2.8 cm^{-1}.

3.2.3 $FeCl_3$ vapor doping

A PBTTT-C16 film was doped by exposure to $FeCl_3$ vapor at reduced pressure using a cell, and the setup is the same as that in Figure 2.3. The PBTTT-C16 film was formed on a BaF_2 window of the cell by spin coating. Solid $FeCl_3$ powder was placed into the cell. The Vis/NIR absorption spectra were obtained using a JASCO V-570 UV/Vis/NIR spectrometer. Infrared spectra were measured on a Digilab FTS-7000 FT-IR spectrometer with a deuterium triglycine sulfate detector. Raman spectra were measured on a Renishaw InVia Raman microscope with an excitation wavelength of 785 nm.

3.2.4 Raman and electrochemical measurements of ILGTs

Raman and electrochemical measurements were performed on the same ILGT. Raman spectra were measured on a Renishaw InVia Raman microscope with an excitation wavelength of 785 nm. I_D was measured, and V_D was applied using a KEITHLEY 6487 picoammeter/voltage source. I_G was measured, and V_G was applied using an ADVANTEST R6243DC current monitor/voltage source. The dependence of the Raman spectrum on V_G was measured from V_G = 0 to −2.0 V every −0.1 V, and measurements were taken 30 s after the change in the V_G. The change in I_G as a function of time was integrated over 200 s starting from the change in V_G; the current after 200 s was considered I_L. I_D was also measured after 200 s. Thus, the stepwise injection charge was obtained. The injected charge (Q) at V_G was the sum of the stepwise injected charges. The charge density (n) can be evaluated from equation 2.1. Based on the XRD data, the lattice parameters of the unit cell of a PBTTT-C16 triclinic crystal are a = 2.35 nm, b = 0.54 nm, c = 1.35 nm, α = 137°, β = 87°, γ = 92°, and Z = 1 [18]. Using these values, the number of repeating units per unit volume (N) was calculated to be 8.57×10^{20} cm^{-3}. The number of π electrons in one unit of PBTTT-C16 was 14. The doping level per π electron (x, %/π electron) was calculated using equation 2.2. The average electrical conductivity (σ) in the channel was calculated from I_D, V_D = −0.01 V, the width of the channel (W = 1.0 mm), the length of the channel (L = 5.0×10 μm) and the thickness of the film (d = 5.0×10 nm). The mobility (μ) was obtained from σ, the carrier density (p, $p = n$ for polarons; $p = n/2$ for bipolarons), and the charge of a carrier (q, $q = +e$ for a polaron; $q = +2e$ for a bipolaron) using equation 2.3.

3.3 Results and discussion

3.3.1 Evaluation of the crystalline content using Raman spectroscopy

AFM images of the unannealed and annealed samples are shown in Figure 3.2. The surface roughness was reduced by thermal annealing. The XRD patterns of the unannealed and annealed PBTTT-C16 films are shown in Figure 3.3. Diffraction lines were observed at 2θ = 3.71, 7.43, and 11.0° and are assigned to the (100), (200), and (300) planes, respectively [19]. The intensities of the lines of the annealed film are stronger than those of the unannealed film, indicating that thermal annealing increases the crystallinity of the film. The crystallinity of polyethylene has been determined by XRD in Ref. [20]. If an amorphous halo is observed in XRD data, the crystallinity can be evaluated. However, the XRD signals of PBTTT-C16 shows so small 2 θ angles, and it is difficult to observe the amorphous halo clearly because the injected X-ray overlaps the region of the amorphous halo. Therefore, XRD is not suitable to evaluate the crystallinity of PBTTT-C16 films. The Raman spectra of an unannealed PBTTT-C16 film are shown in Figure 3.4. The bands at 1490 cm^{-1} and 1416 cm^{-1} are assigned to the C=C stretching mode of the thiophene ring, and the band at 1392 cm^{-1} is assigned to the the C=C stretching mode of the thienothiophene ring [6]. The 1490-cm^{-1} band is indicative of the effective conjugation, which is dependent on the solid state of the polymer. Therefore, this band was deconvoluted into a crystalline band and an amorphous band to evaluate the crystalline content in PBTTT-C16 films. The parameters of the curve fitting were determined and are shown in Table 3.1. The position and the FWHM of the crystalline band are fixed at 1489.4 cm^{-1} and 12 cm^{-1}, respectively. The band shape is a Lorentzian function. The amorphous region does not have a simple morphology, and its band shape is that of a Gaussian function. Therefore, the band shape is a linear combination of the Lorentzian and Gaussian functions. The position of the amorphous band was fixed at 1492 cm^{-1}. The FWHM and the ratio of Gaussian and Lorentzian function were variable. A least-squares fitting method was used for decomposition of the observed spectra from each set of annealing conditions. The results of the decomposition of the bands in the spectra of the PBTTT-C16 films are shown in Figures 3.4 to 3.7. The black lines are the experimental data. The red lines are the compositions of all bands. The yellowish green lines are the decomposed bands. The values of FWHMs and the Gaussian contents of the amorphous bands are shown in Table 3.2. The crystal content (X_C) of the PBTTT-C16 film was calculated from the following equation:

$$X_{\mathrm{C}} = \frac{I_{\mathrm{C}}}{I_{\mathrm{C}} + (\sigma_C/\sigma_A)I_{\mathrm{A}}} \tag{3.1}$$

where I_C and I_A are the integrated intensities of the crystalline and amorphous bands, respectively, and σ_C and σ_A are the cross sections of the crystalline and amorphous bands, respectively. The ratio of σ_C/σ_A of conjugated polymers have been reported in several studies [21–23]. The minimum reported value is 0.59 in Ref. [21], and the maximum reported value is 1.04 in Ref. [23]. The values of X_C calculated from these ratios of cross sections are shown in Table 3.3. Thermal annealing increases X_C. Raman spectroscopy was used to evaluate X_C.

3.3.2 Vis-NIR-IR absorption and Raman spectra of a PBTTT-C16 film doped with $FeCl_3$

Figure 3.8 shows the changes in the optical spectra of a PBTTT-C16 film upon $FeCl_3$ doping. The number of dopants that penetrates the film increases with increasing doping time. A pristine PBTTT-C16 film shows a band at 2.26 eV originating from the π-π* transition (N1). Upon $FeCl_3$ doping, the intensity of the 2.26-eV band decreases, and two new bands appear at approximately 0.41 and 1.71 eV. After 150 min of doping, the intensity of the band at 1.46 eV was strongest. After 180 min, the intensity of the band at 0.24 eV had increased further, while the intensity of the 1.46-eV band had decreased. After 330 min of doping, the 1.46-eV band almost disappears. These spectral changes can be explained based on the theory discussed in Section 2.3.1. The 1.46-eV band is attributed to P2, and the band in the NIR region is attributed to P1. The 0.24-eV band in the NIR region is attributed to BP1. These results indicate that polarons form in the first 150 min of doping, and then bipolarons form after 180 min, as evidenced by the decrease in the intensity of the 1.46-eV band. After 330 min, bipolarons are the dominant species, as evidenced by the absence of the 1.46-eV band, although a small number of polarons may exist after 330 min. It is difficult to separate the remaining 1.46-eV band into the components of polarons and bipolarons because the weak band originated from bipolarons may be observed around 1.46 eV.

The 785-nm excited Raman spectra and the optical absorption measurements of PBTTT-C16 were obtaine. Figure 3.9 shows the changes in the Raman spectra of the PBTTT-C16 film upon $FeCl_3$ doping. The excitation wavelength of 785 nm (1.58 eV) is within the polaron absorption band (1.46 eV). The changes in the Raman spectra can be attributed to polarons and/or bipolarons

based on the results of the optical absorption spectra. After 30 min of doping, the Raman spectrum had changed substantially. The spectrum shows intense bands at 1457, 1332, 1385, 1208, 744 and 692 cm^{-1}, which are attributed to polarons. The carriers ovserved in the first 150 min of doping are attributed to polarons. The bands at 1457 and 1385 cm^{-1} show small downward shifts and a change in their relative intensities. The band at 1385 cm^{-1} are assigned to a stretching mode of the thienothiophene ring [6]. After 180 min of doping, the intensity of the band at 1431 cm^{-1} increases substantially. At 390 min, i.e., when bipolarons are dominant, bands are observed at 1502, 1431, 1370, 1207, 741, and 690 cm^{-1}, and they are attributed to bipolarons. The band at 1431 cm^{-1} is more intense than the band at 1370 cm^{-1}. The band at 1370 cm^{-1} is assignable to a stretching mode of the thienothiophene ring. These results indicate that Raman spectral features between 1500 and 1300 cm^{-1} can be used to identify the types of carriers in PBTTT-C16. Polarons have the strongest band at 1385−1380 cm^{-1}, and a strong band at 1457−1451 cm^{-1} with a 1432-cm^{-1} shoulder. On the other hand, bipolarons have the strongest band at 1431 cm^{-1}, and a strong band at 1373−1370 cm^{-1}.

3.3.3 Raman spectra of ILGTs

Figure 3.10 shows the changes in the Raman spectra of an unannealed ILGT as a function of $-V_G$ from 0.0 to 2.0 V. The spectrum acquired at $-V_G$ = 0.0 V shows intense bands at 1490, 1460, 1417 and 1393 cm^{-1}, which are indicative of neutral PBTTT-C16 polymers. The other observed bands are attributed to [BMIM][TFSI]. The intensity of the 1392-cm^{-1} band at $-V_G$ = 0.9 V increases. The spectra acquired at $-V_G$ = 0.9 and 1.0 V are attribute to a mixture of neutral species and polarons. The spectra collected between $-V_G$ = 1.1 and 1.4 V are attributed to polarons because these spectra are quite similar to that of polarons generated by $FeCl_3$ doping shown in Figure 3.9. The spectra acquired at $-V_G$ = 1.5 and 1.6 V are attributed to a mixture of polarons and bipolarons. The spectra acquired above $-V_G$ = 1.7 V are attribute to bipolarons. Accordingly, polarons form below $-V_G$ = 1.4 V, polarons and bipolarons coexist at $-V_G$ = 1.5 and 1.6 V, and bipolarons are dominant above $-V_G$ = 1.7 V.

The changes in the Raman spectra of an ILGT fabricated with an annealed PBTTT-C16 film on V_G is shown in Figure 3.11. The types of carriers generated in the device are also identified as described above. According to the Raman spectra, polarons form below $-V_G$ = 1.1 V, polarons and bipolarons coexist at $-V_G$ = 1.2 and 1.3 V, and bipolarons are dominant above $-V_G$ = 1.4 V.

3.3.4 Electrochemical properties of ILGTs

The transfer characteristics of an ILGT fabricated with an unannealed PBTTT-C16 film at V_D = −0.01 V are shown in Figure 3.12. The $-I_D$ increases gradually when a voltage is initially applied due to electrostatic doping. On the other hand, $-I_D$ increases rapidly from 1.0 to 1.4 V and plateaus at voltages from 1.4 to 2.0 V due to electrochemical doping. The increases in $-I_D$ indicate the formation of carriers in the channel region. The n and x were calculated from the measured Q. The relationship between n and $-V_G$ is shown in Figure 3.13, and the relationship between x and $-V_G$ is shown in Figure 3.14. According to the Raman results, polarons are generated below 5.5%. Bipolarons begin to form from polarons at x = 7.3%, and they are the dominant carriers above x = 11%. The σ values were calculated from the observed I_D values and plotted against x in Figure 3.15. The σ values increased gradually from x = 0 to x = 1.2% and then increase rapidly above x = 1.5%. In this range, the σ values show a plateau at approximately 193 S cm^{-1}. The μ values of the polarons were obtained from the data collected below x = 5.5% ($n = 6.6\times10^{20}$ cm^{-3}, $-V_G$ = 1.4 V). The μ values of the bipolarons were obtained from the data collected above x = 11% ($n = 1.3\times10^{21}$ cm^{-3}, $-V_G$ = 1.7 V), although a small number of polarons may exist even above 11%. These μ values were also plotted against x in Figure 3.15 with the σ values. The μ values of the polarons were strongly dependent on x, and they increased with increasing x. The μ values of the bipolarons were moderately dependent on x. The highest μ values of the polarons and bipolarons were 1.0 cm^2 V^{-1} s^{-1} (observed at x = 5.5%, $n = 6.6\times10^{20}$ cm^{-3}) and 0.92 cm^2 V^{-1} s^{-1} (observed at x = 11%, $n = 1.3\times10^{21}$ cm^{-3}), respectively.

The transfer characteristics of an annealed PBTTT-C16 ILGT at V_D = −0.01 V are shown in Figure 3.16. The n and x values were calculated from the measured Q. The relationship between n and $-V_G$ is shown in Figure 3.17, and the relationship between x and $-V_G$ is shown in Figure 3.18. The σ values were calculated from the observed I_D values and were plotted against x in Figure 3.19. The μ values of the polarons were obtained from the data collected below x =2.7% ($-V_G$ = 1.1 V); the μ values of the bipolarons were obtained from the data collected above x = 4.8% ($-V_G$ = 1.4 V). The plots of these μ values are also shown in Figure 3.19. The σ values increase gradually from x = 0 to x = 0.19% and then increase rapidly above x = 0.28%. These increases are caused by electrostatic and electrochemical doping, respectively. According to the Raman results, polarons are generated below x = 2.7%. Bipolarons start to form from polarons at

x = 3.4%, and they are the dominant carriers above x = 4.8%. Then, the σ values show a plateau at approximately 118 S cm^{-1}. The μ values of the polarons increase with increasing x. The highest μ value of the polarons was 1.0 cm^2 V^{-1} s^{-1}, which was observed at x = 2.7% (n = 3.2×10^{20} cm^{-3}). The μ values of the bipolarons are moderately dependent on x. The highest μ value of the bipolarons was 1.2 cm^2 V^{-1} s^{-1}, and this value was observed at x = 4.8 and 5.2% (n = 5.7 and 6.2×10^{20} cm^{-3}).

Bipolaron formation begins at x = 7.3% in the unannealed ILGT, whereas bipolaron formation begins at x = 3.4% in the annealed ILGT, which indicates that polarons are more stable in the disordered structure of the unannealed PBTTT-C16 than they are in the annealed system. The σ values increased rapidly above x = 1.5% ($-V_G$ = 1.0 V) for the unannealed ILGT. On the other hand, the σ values increased rapidly above x = 0.28% ($-V_G$ = 0.5 V) for the annealed ILGT. This result can be attributed to the difference in the oxidation potential of the unannealed and annealed PBTTT-C16. The highest μ values of the polarons and bipolarons in the unannealed ILGT are in the same order as those of the annealed ILGT. The crystalline content of PBTTT-C16 in the annealed film is greater than that of the unannealed film. The highest μ value of the bipolarons in the annealed PBTTT-C16 ILGT is slightly higher than that in the unannealed ILGT. A higher crystalline content was achieved, which resulted in the highest μ value. The mobilities of the bipolarons in PBTTT-C16 are also substantially larger than those of the bipolarons in P3HT.

3.4 Conclusion

The values of X_C in PBTTT-C16 films were evaluated using Raman spectroscopy. Deconvolution of the Raman bands showed that thermal annealing increased X_C. Raman spectroscopy is a powerful tool for evaluating the X_C of polymers.

The changes in the absorption and Raman spectra of a PBTTT-C16 film upon $FeCl_3$ doping were determined. Based on the assignments of the absorption spectra, the Raman spectra of the positive polarons and bipolarons of PBTTT-C16 were elucidated. Carrier formation in ILGTs was explained using the Raman spectra of the carriers. The electrical conductivity and doping levels were determined using electrochemical measurements of the ILGTs fabricated with unannealed and annealed PBTTT-C16 films. The types of carriers were as a function of the doping level were elucidated. The mobilities were calculated from the conductivities and carrier densities.

Bipolarons start to form at x = 7.3%/π electron and are the dominant carriers above x = 11% for unannealed PBTTT-C16, whereas bipolarons begin to form at x = 3.4% and are the dominant carriers above x = 4.8% for annealed PBTTT-C16. Bipolarons in annealed PBTTT-C16 form at lower doping levels than in unannealed PBTTT-C16. Polarons are more stable in the disordered structure of PBTTT-C16. The mobilities of bipolarons are high in both unannealed and annealed films. The highest μ values of the bipolarons in the unannealed and annealed films were 0.92 and 1.2 $cm^2 V^{-1} s^{-1}$, respectively.

3.4 References

[1] H. Sirringhaus, R.J. Wilson, R.H. Friend, M. Inbasekaran, W. Wu, E.P. Woo, M. Grell, D.D.C. Bradley, Mobility enhancement in conjugated polymer field-effect transistors through chain alignment in a liquid-crystalline phase, Appl. Phys. Lett. 77 (2000) 406. doi:10.1063/1.126991.

[2] Y. Li, S.P. Singh, P. Sonar, A High Mobility P-Type DPP-thieno[3,2-b]thiophene copolymer for organic thin-film transistors, Adv. Mater. 22 (2010) 4862–4866. doi:10.1002/adma.201002313.

[3] W. Ma, C. Yang, X. Gong, K. Lee, A.J. Heeger, Thermally stable, efficient polymer solar cells with nanoscale control of the interpenetrating network morphology, Adv. Funct. Mater. 15 (2005) 1617–1622. doi:10.1002/adfm.200500211.

[4] H. Ito, T. Harada, H. Tanaka, S. Kuroda, Critical regime for the insulator-metal transition in highly ordered conjugated polymers gated with ionic liquid, Jpn. J. Appl. Phys. 55 (2016) 03DC08. doi:10.7567/JJAP.55.03DC08.

[5] H. Tanaka, M. Hirate, S. Watanabe, S. Kuroda, Microscopic signature of metallic state in semicrystalline conjugated polymers doped with fluoroalkylsilane molecules, Adv. Mater. 26 (2014) 2376–2383. doi:10.1002/adma.201304691.

[6] C. Francis, D. Fazzi, S.B. Grimm, F. Paulus, S. Beck, S. Hillebrandt, A. Pucci, J. Zaumseil, Raman spectroscopy and microscopy of electrochemically and chemically doped high-mobility semiconducting polymers, J. Mater. Chem. C. 5 (2017) 6176–6184. doi:10.1039/C7TC01277B.

[7] T. Harada, H. Ito, Y. Ando, S. Watanabe, H. Tanaka, S. Kuroda, Signature of the insulator-metal transition of a semicrystalline conjugated polymer in ionic-liquid-gated transistors, Appl. Phys. Express. 8 (2015) 021601. doi:10.7567/APEX.8.021601.

[8] T. Umeda, D. Kumaki, S. Tokito, Surface-energy-dependent field-effect mobilities up to 1 cm^2/V s for polymer thin-film transistor, J. Appl. Phys. 105 (2009) 024516. doi:10.1063/1.3072669.

[9] I. McCulloch, M. Heeney, C. Bailey, K. Genevicius, I. MacDonald, M. Shkunov, D. Sparrowe, S. Tierney, R. Wagner, W. Zhang, M.L. Chabinyc, R.J. Kline, M.D. McGehee, M.F. Toney, Liquid-crystalline semiconducting polymers with high charge-carrier mobility, Nat. Mater. 5 (2006) 328–333. doi:10.1038/nmat1612.

[10] D.M. DeLongchamp, R.J. Kline, Y. Jung, E.K. Lin, D.A. Fischer, D.J. Gundlach, S.K. Cotts, A.J. Moad, L.J. Richter, M.F. Toney, M. Heeney, I. McCulloch, Molecular basis of mesophase ordering in a thiophene-based copolymer, Macromolecules. 41 (2008) 5709–5715. doi:10.1021/ma800440f.

[11] D.M. DeLongchamp, R.J. Kline, Y. Jung, D.S. Germack, E.K. Lin, A.J. Moad, L.J. Richter, M.F. Toney, M. Heeney, I. McCulloch, Controlling the orientation of terraced nanoscale "ribbons" of a poly(thiophene) semiconductor, ACS Nano. 3 (2009) 780–787. doi:10.1021/nn800574f.

[12] B.H. Hamadani, D.J. Gundlach, I. McCulloch, M. Heeney, Undoped polythiophene field-effect transistors with mobility of $1 cm^2 V^{-1} s^{-1}$, Appl. Phys. Lett. 91 (2007) 243512. doi:10.1063/1.2824845.

[13] T. Higashi, N. Yamasaki, H. Utsumi, H. Yoshida, A. Fujii, M. Ozaki, Thermal annealing effects on optical anisotropy of aligned thiophene-based π-conjugated polymer films fabricated by capillary action, Jpn. J. Appl. Phys. 51 (2012) 02BK11. doi:10.1143/JJAP.51.02BK11.

[14] K. Fesser, A.R. Bishop, D.K. Campbell, Optical absorption from polarons in a model of polyacetylene, Phys. Rev. B. 27 (1983) 4804–4825. doi:10.1103/PhysRevB.27.4804.

[15] Y. Shimoi, S. Abe, K. Harigaya, Theory of optical absorption in doped conjugated polymers, Mol. Cryst. Liq. Cryst. Sci. Technol. Sect. A. Mol. Cryst. Liq. Cryst. 267 (1995) 329–334. doi:10.1080/10587259508034012.

[16] J.A. Blackman, M.K. Sabra, Interchain coupling and optical absorption in degenerate and nondegenerate polymers, Phys. Rev. B. 47 (1993) 15437–15448. doi:10.1103/PhysRevB.47.15437.

[17] S. Irle, H. Lischka, An *ab initio* investigation of the charge−transfer complexes of alkali atoms with oligo (α,α′) thiophenes and oligoparaphenylenes: a model calculation on polaronic and bipolaronic defect structures, J. Chem. Phys. 103 (1995) 1508–1522. doi:10.1063/1.469772.

[18] E. Cho, C. Risko, D. Kim, R. Gysel, N. Cates Miller, D.W. Breiby, M.D. McGehee, M.F. Toney, R.J. Kline, J.-L. Bredas, Three-dimensional packing structure and electronic properties of biaxially oriented poly(2,5-bis(3-alkylthiophene-2-yl)thieno[3,2-*b*]thiophene) films, J. Am. Chem. Soc. 134 (2012) 6177–6190. doi:10.1021/ja210272z.

[19] M.L. Chabinyc, M.F. Toney, R.J. Kline, I. McCulloch, M. Heeney, X-ray scattering study

of thin films of poly(2,5-bis(3-alkylthiophen-2-yl)thieno[3,2- *b*]thiophene), J. Am. Chem. Soc. 129 (2007) 3226–3237. doi:10.1021/ja0670714.

[20] S. Krimm, A. V. Tobolsky, Quantitative X-ray studies of order in amorphous and crystalline polymers. Quantitative X-ray determination of crystallinity in polyethylene, J. Polym. Sci. 7 (1951) 57–76. doi:10.1002/pol.1951.120070105.

[21] W.C. Tsoi, D.T. James, J.S. Kim, P.G. Nicholson, C.E. Murphy, D.D.C. Bradley, J. Nelson, J.-S. Kim, The nature of in-plane skeleton Raman modes of P3HT and their correlation to the degree of molecular order in P3HT:PCBM blend thin films, J. Am. Chem. Soc. 133 (2011) 9834–9843. doi:10.1021/ja2013104.

[22] Y. Furukawa, Vibrational spectroscopy of organic thin films used for solar cells, in: AIP Conf. Proc., 2013: pp. 5–8. doi:10.1063/1.4820272.

[23] Y. Iwasawa, Raman studies on the solid structures of bulk heterojunction films used for organic solar cells, Waseda University, 2018. https://waseda.repo.nii.ac.jp/?action=pages_view_main&active_action=repository_view_main_item_detail&item_id=41416&item_no=1&page_id=13&block_id=21 (accessed December 13, 2018).

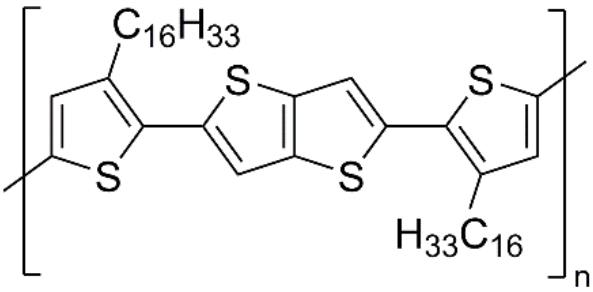

Figure 3.1. Chemical structure of PBTTT-C16

Unannealed sample

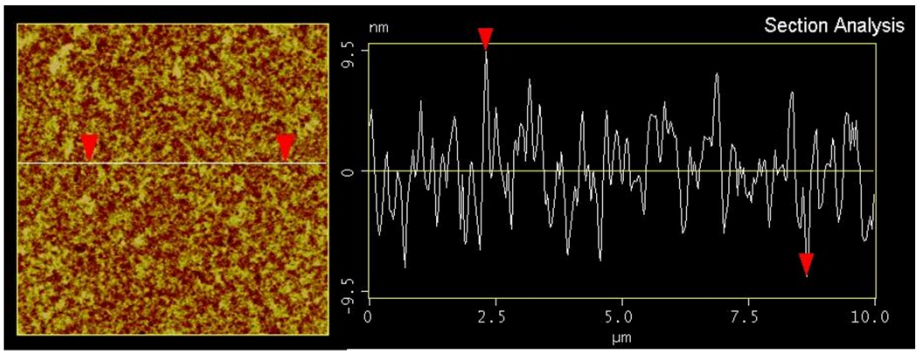

Sample annealed at 235 °C

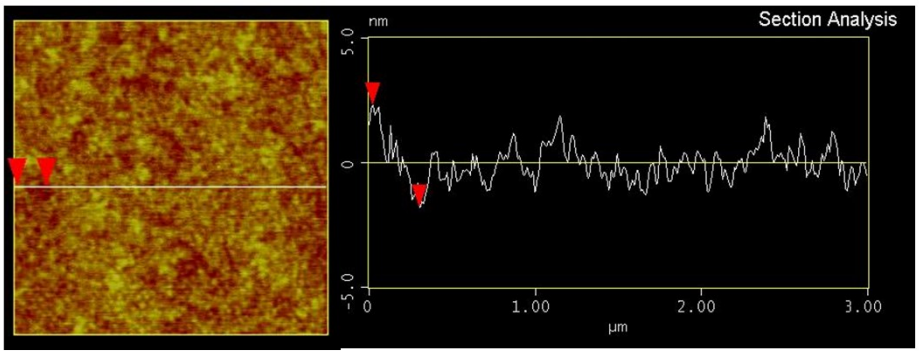

Figure 3.2. AFM images of unannealed and annealed PBTTT-C16 films

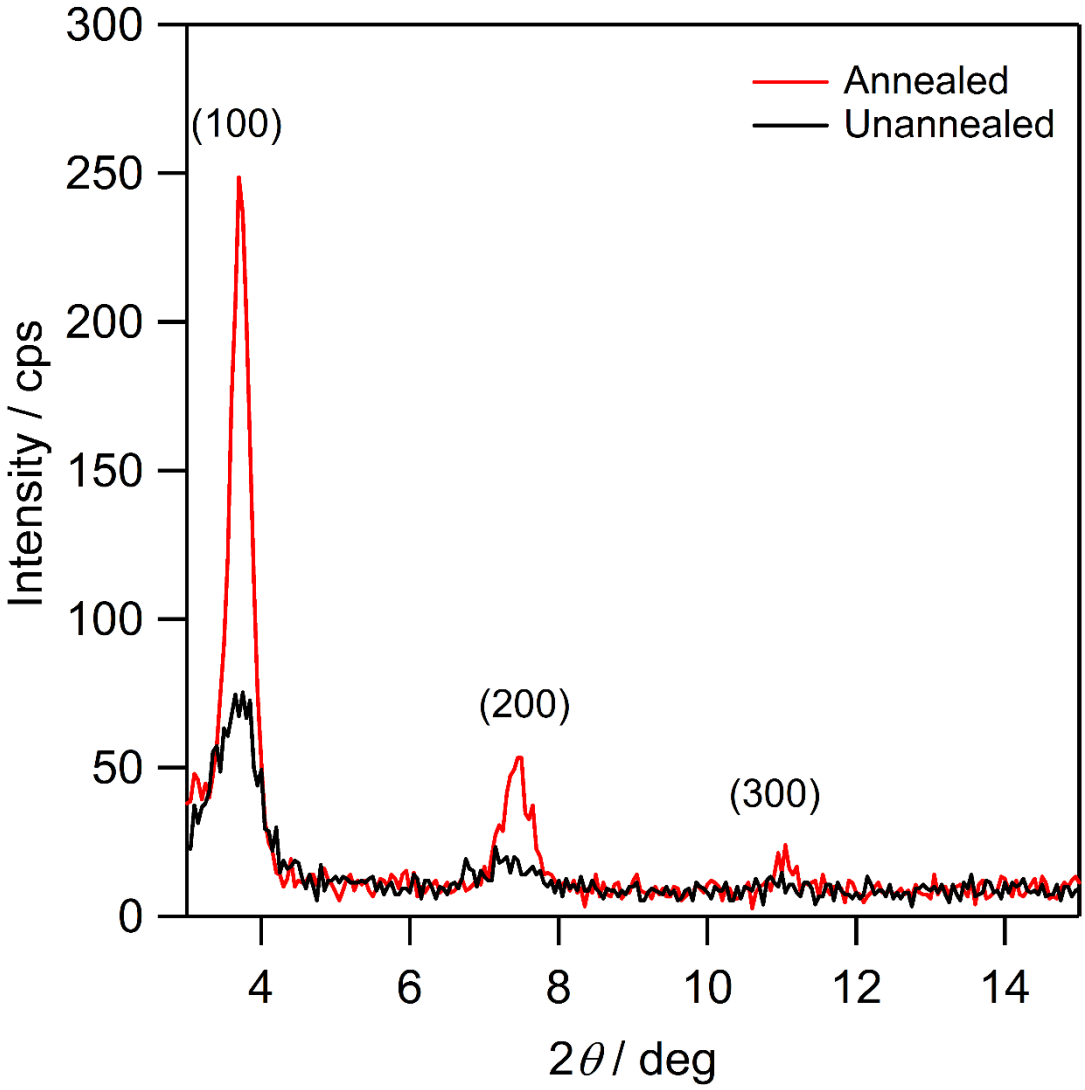

Figure 3.3 XRD patterns of annealed and unannealed PBTTT-C16 films

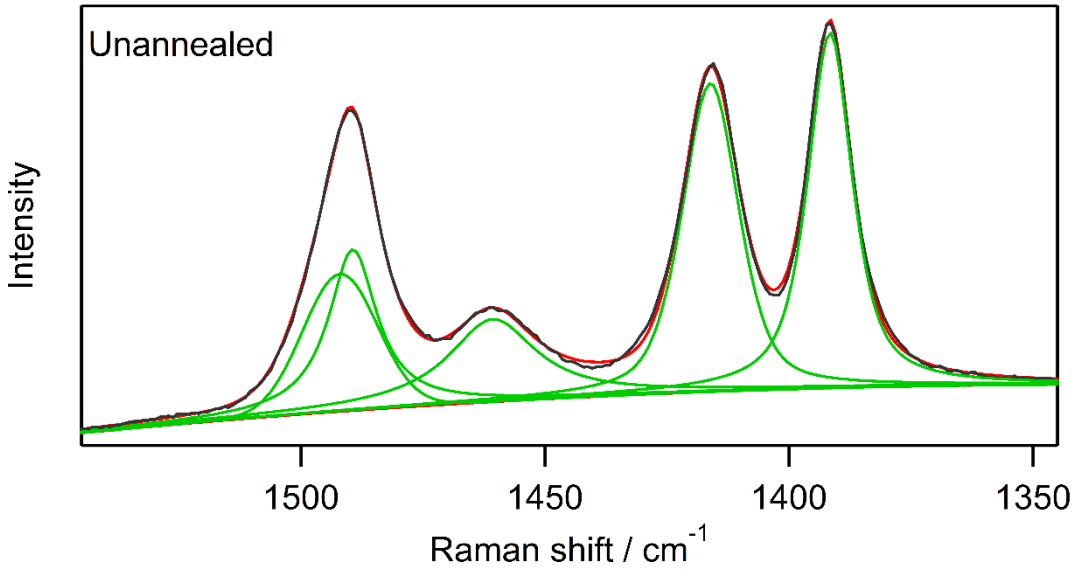

Figure 3.4. Raman spectrum of an unannealed PBTTT-C16 film

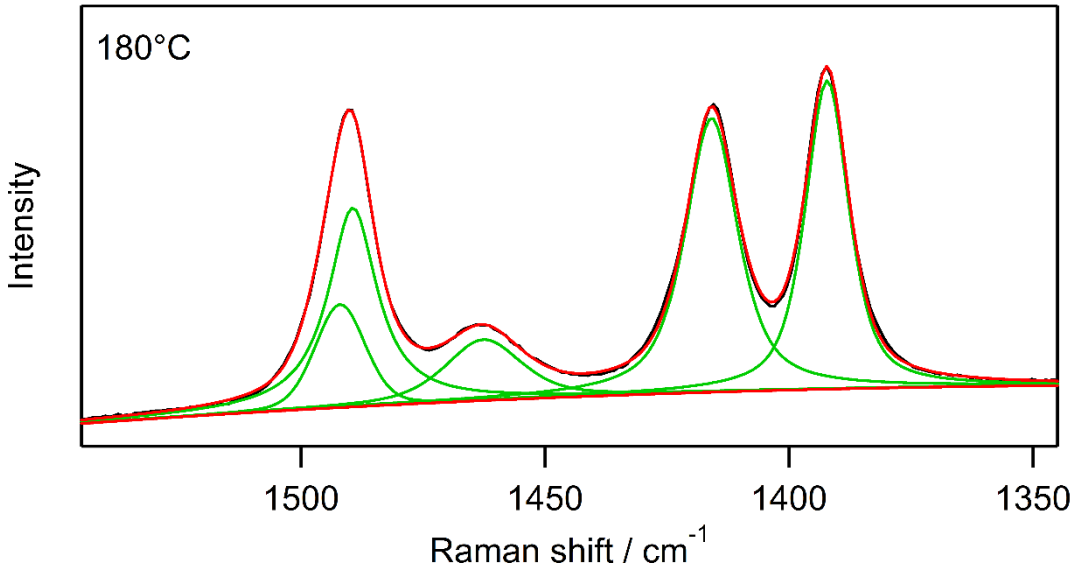

Figure 3.5. Raman spectrum of an annealed PBTTT-C16 film at 180 °C

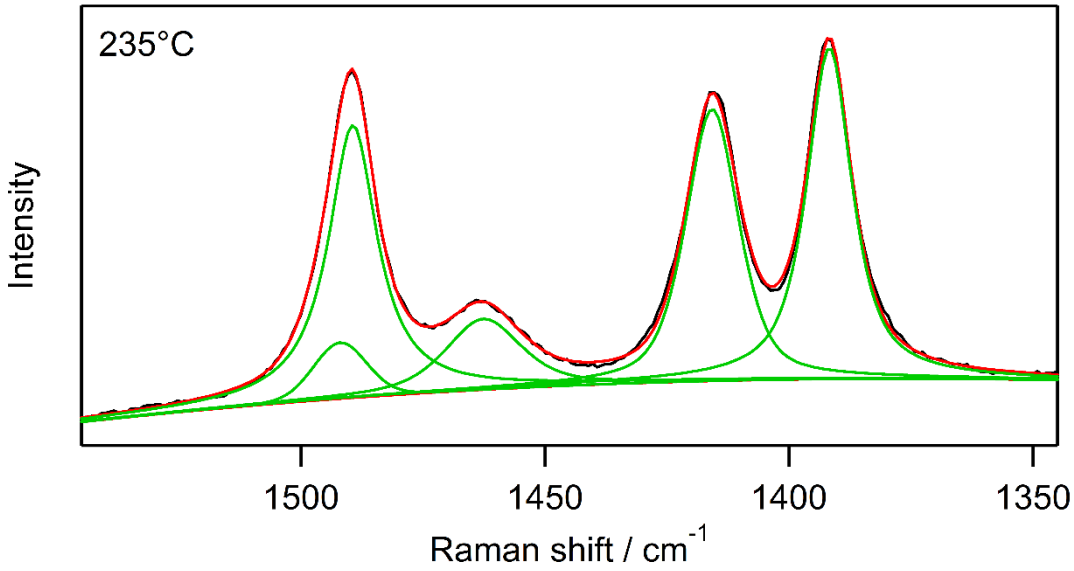

Figure 3.6. Raman spectrum of an annealed PBTTT-C16 film at 235 °C

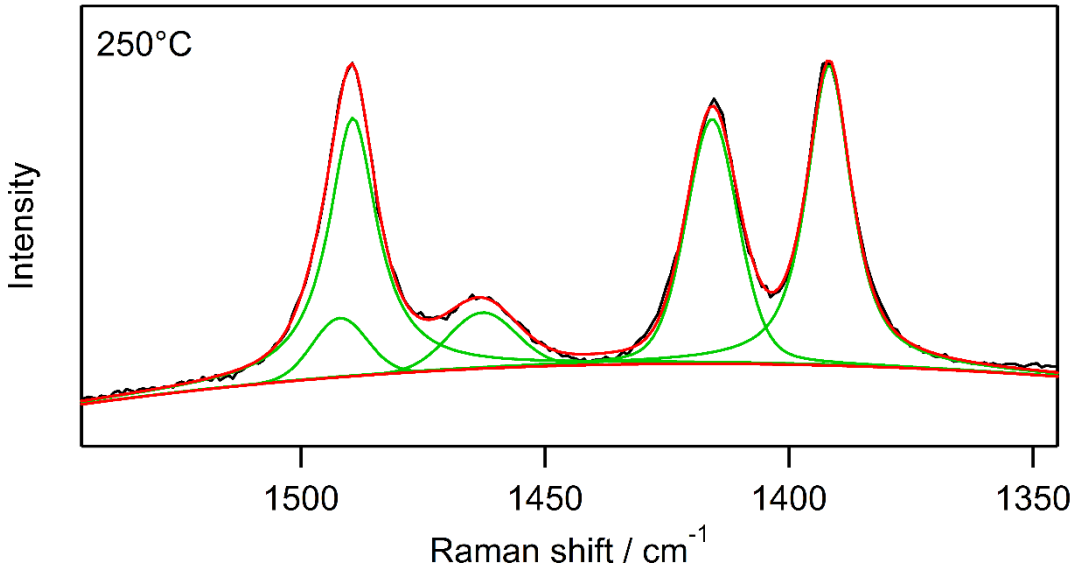

Figure 3.7. Raman spectrum of an annealed PBTTT-C16 film at 250 °C

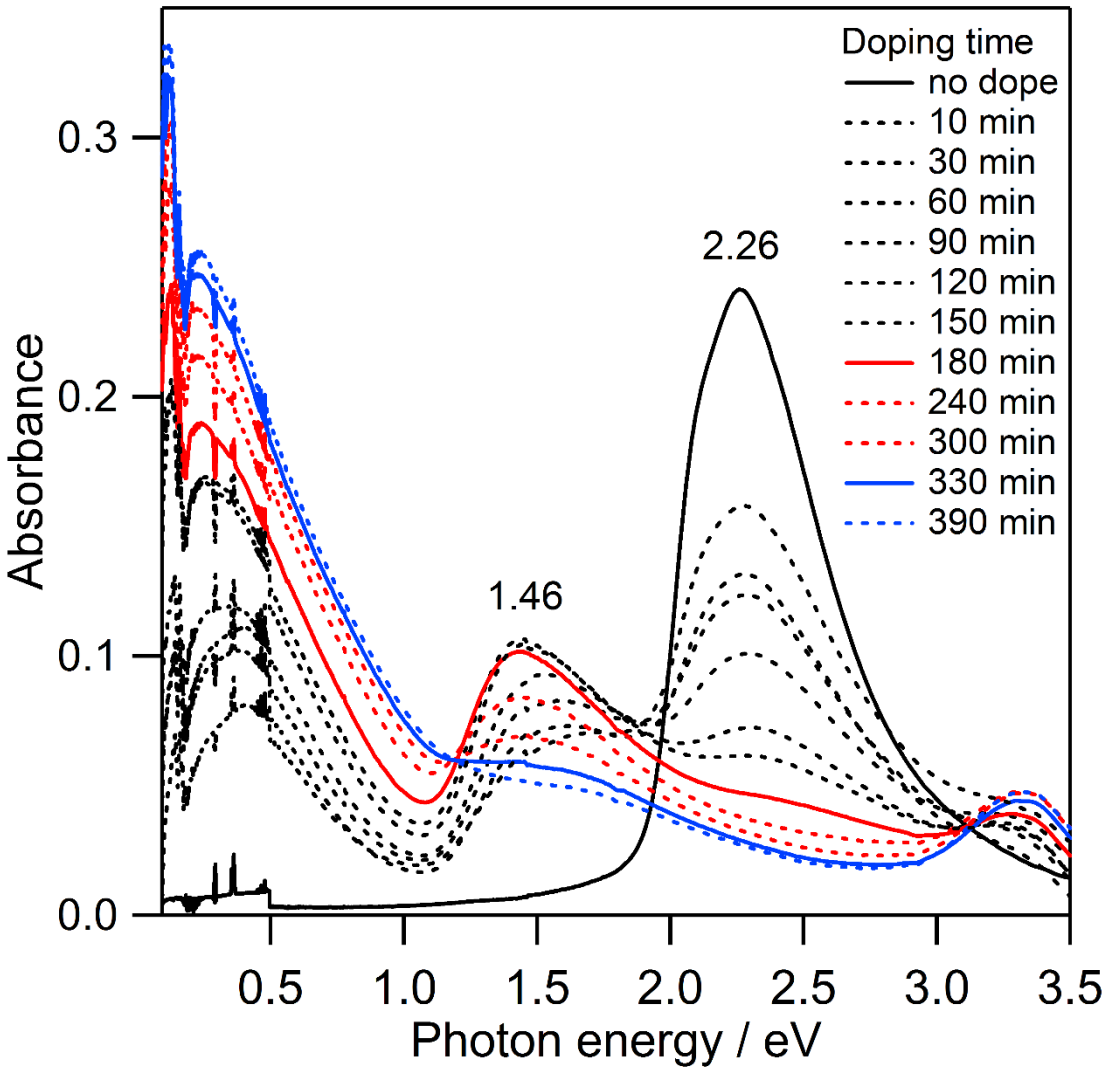

Figure3.8. Changes in the absorption spectra of a PBTTT-C16 film upon $FeCl_3$ doping

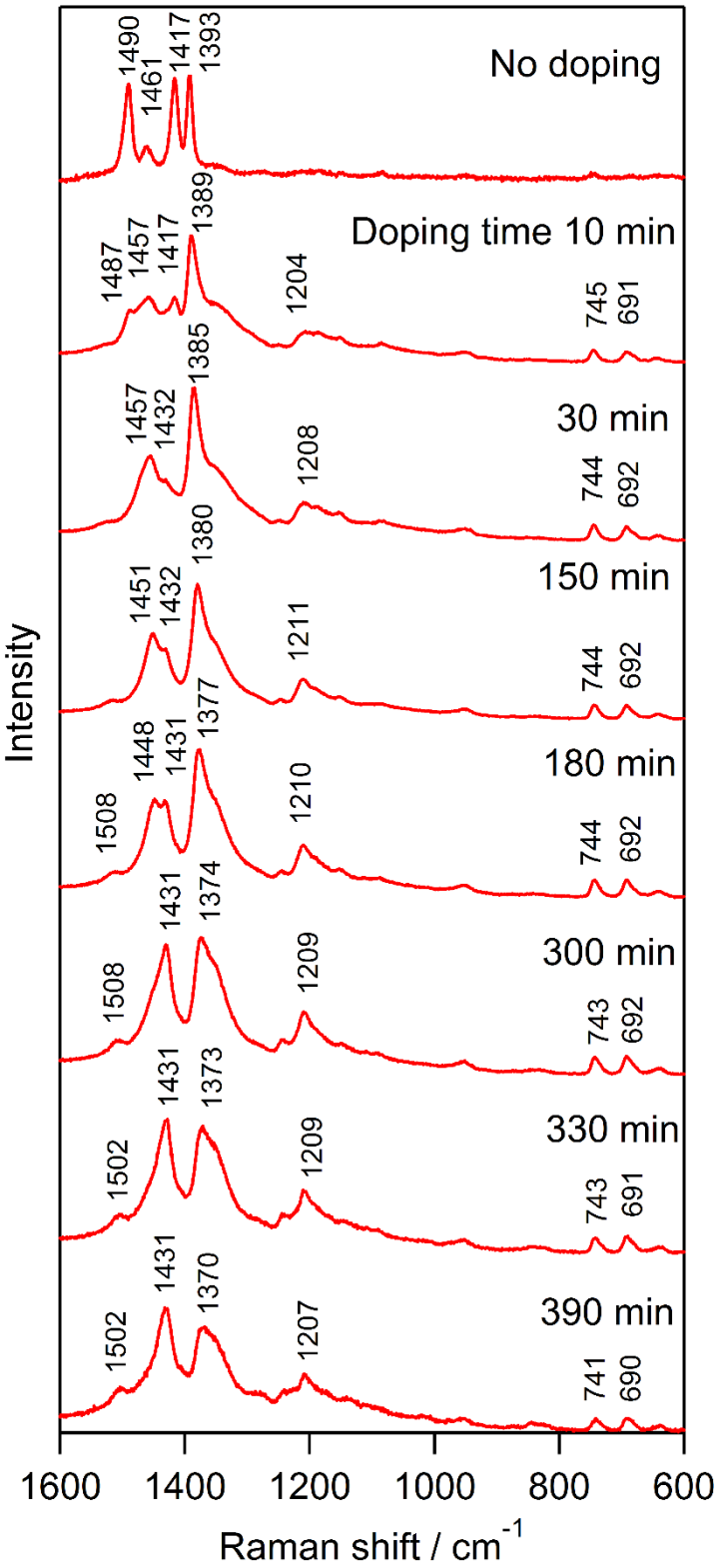

Figure 3.9. Changes in the Raman spectra of a PBTTT-C16 film upon $FeCl_3$ doping.

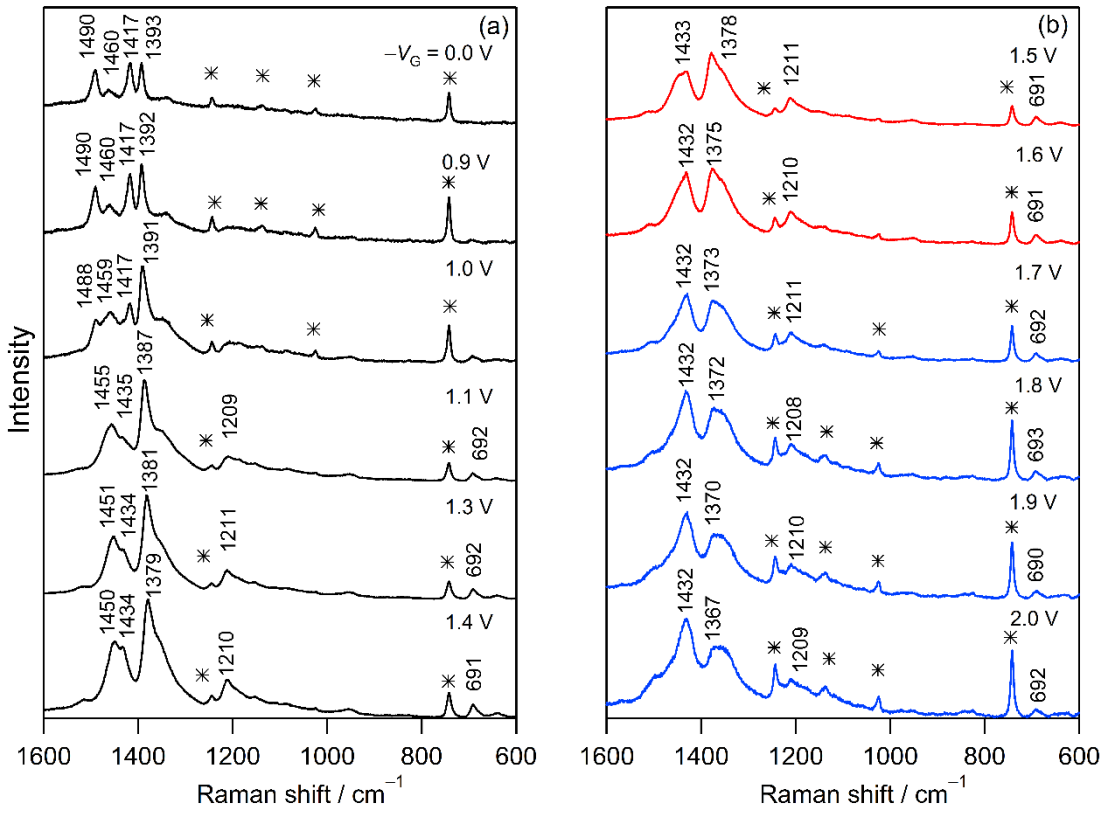

Figure 3.10. Changes in the Raman spectra of an unannealed PBTTT-C16 ILGT upon application of $-V_G$

(* indicates the bands of [BMIM][TFSI])

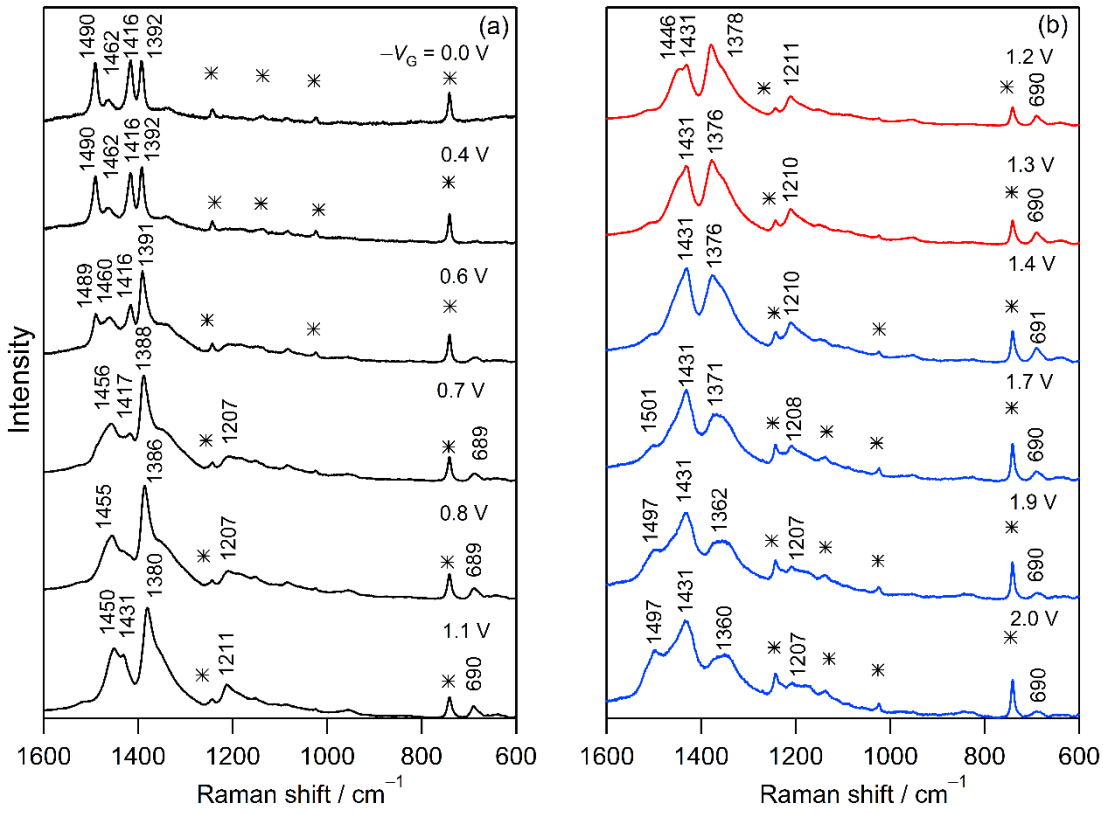

Figure 3.11. Changes in the Raman spectra of an annealed PBTTT-C16 ILGT upon application of $-V_G$

(* indicates the bands of [BMIM][TFSI])

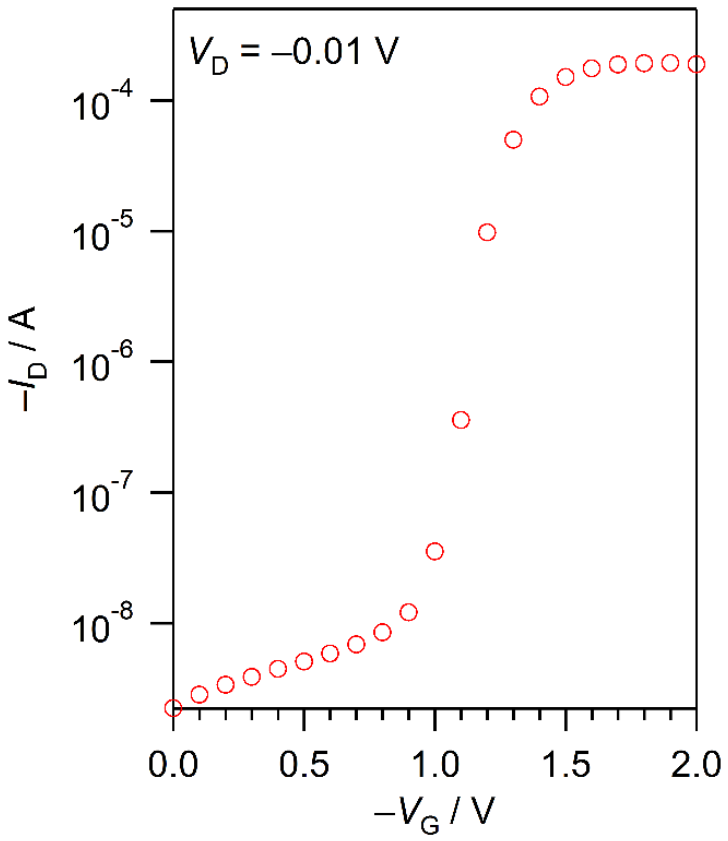

Figure 3.12. Transfer characteristics of an ILGT fabricated with unannealed PBTTT-C16

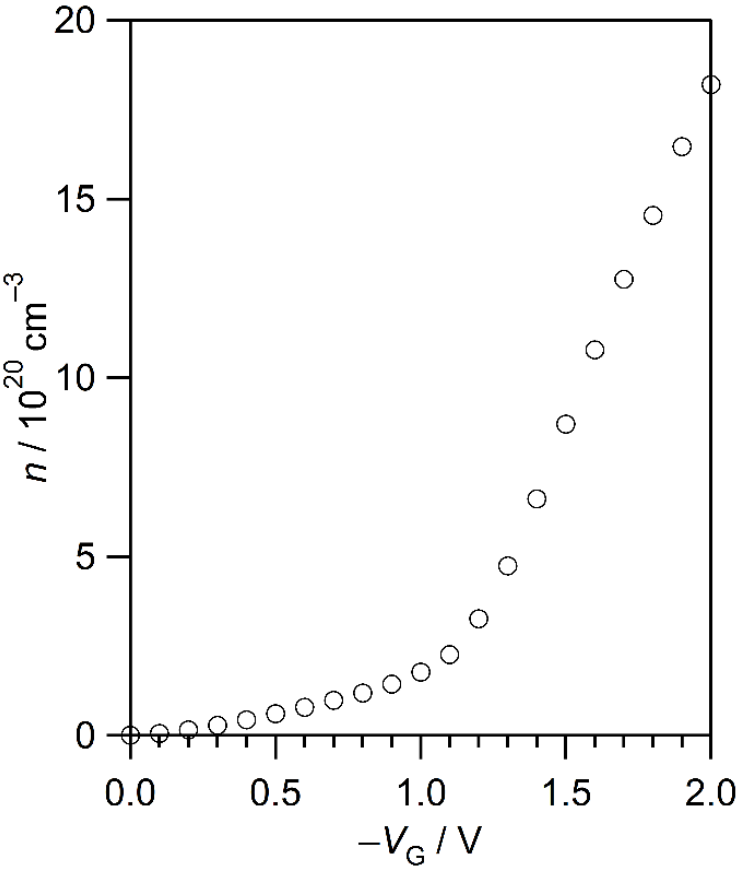

Figure 3.13. Plots of n versus $-V_G$ for an ILGT fabricated with unannealed PBTTT-C16

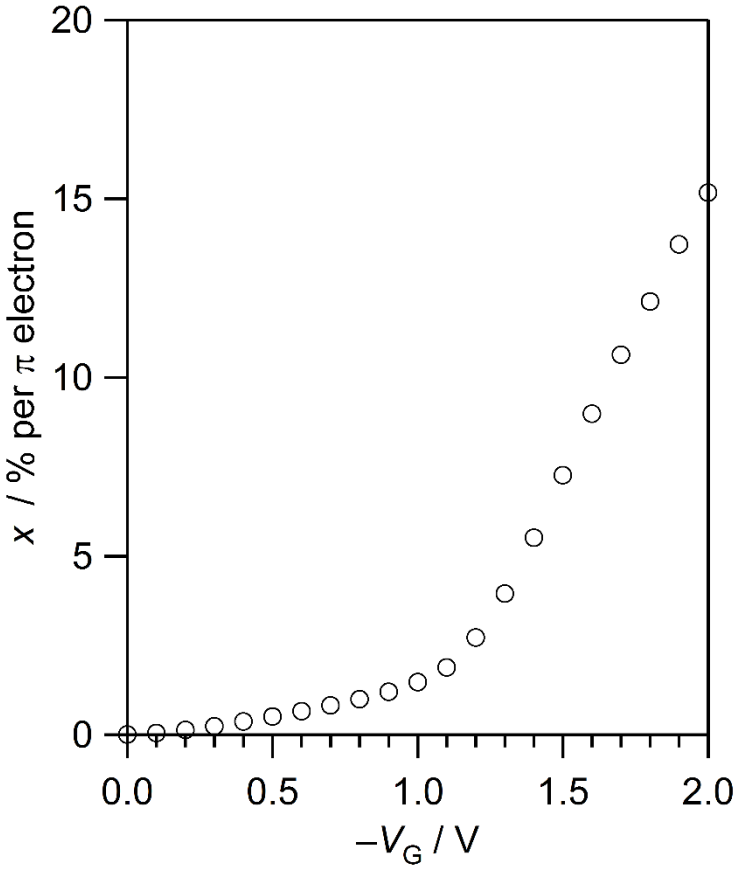

Figure 3.14. Plots of x versus $-V_G$ for an ILGT fabricated with unannealed PBTTT-C16

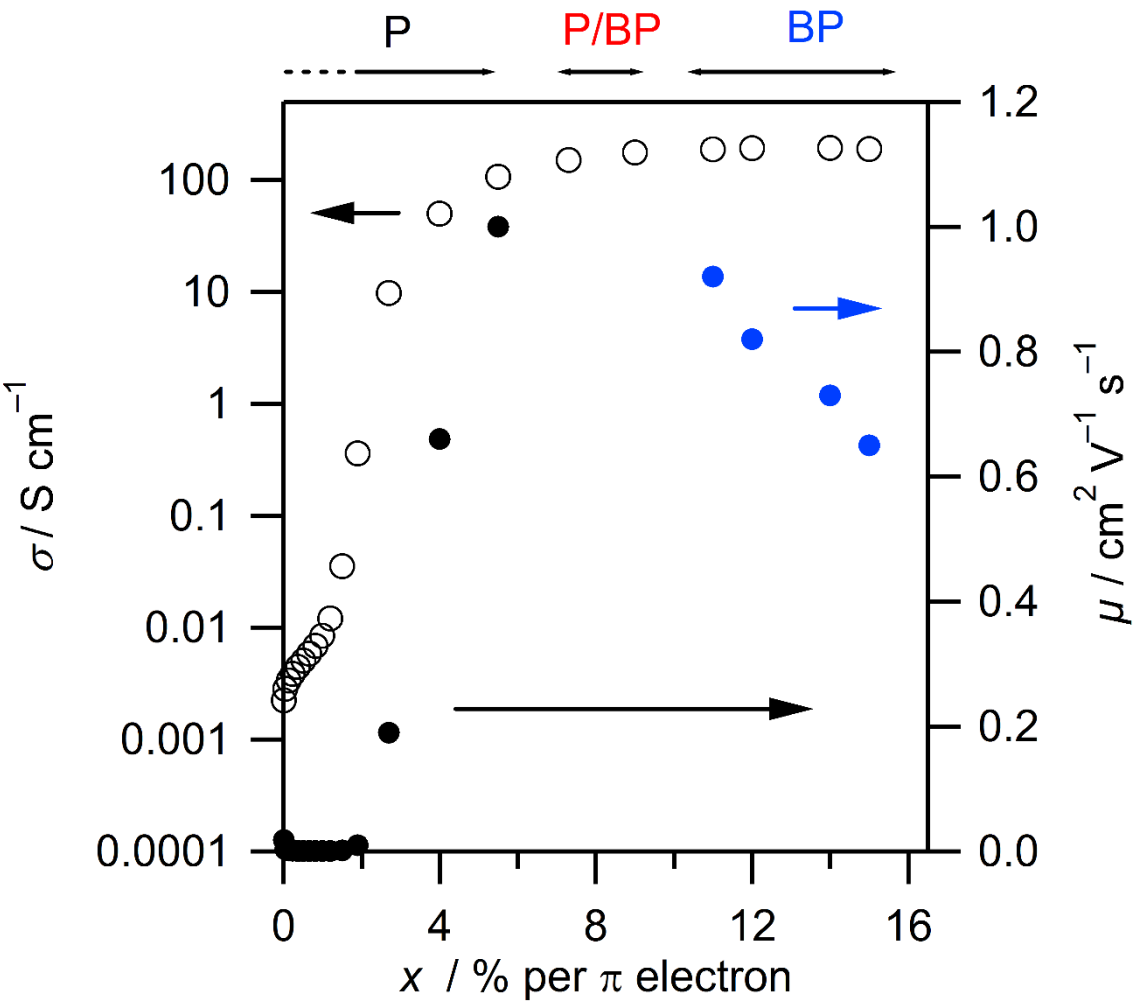

Figure 3.15. Plots of σ and μ versus x for an ILGT fabricated with unannealed PBTTT-C16

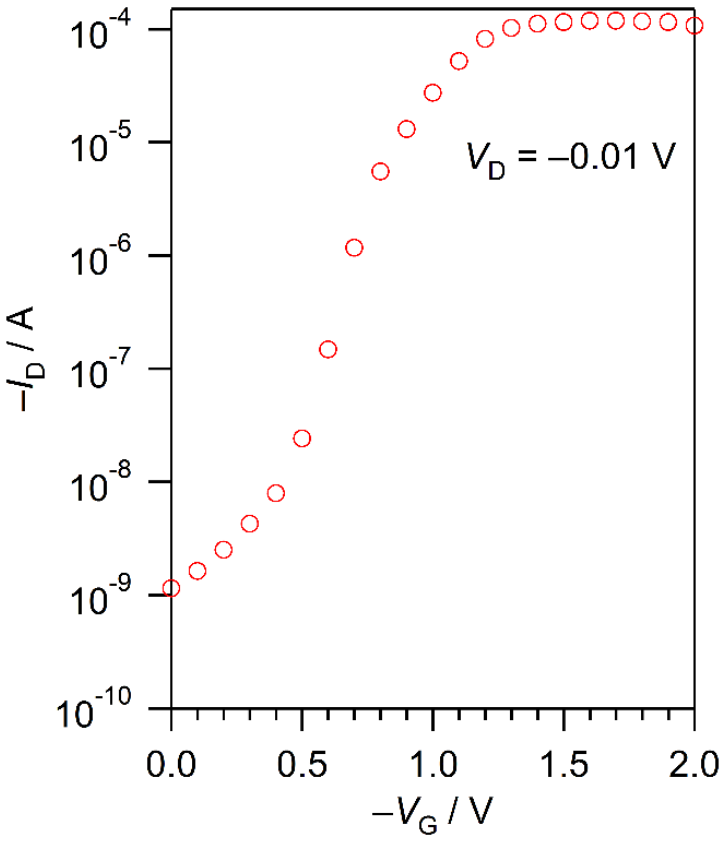

Figure 3.16. Transfer characteristics of an ILGT fabricated with annealed PBTTT-C16

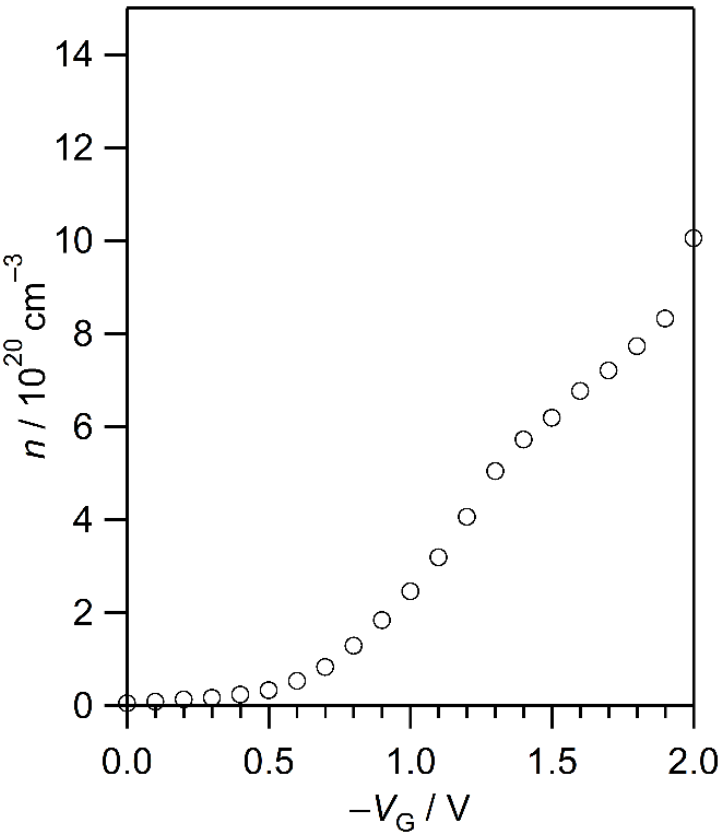

Figure 3.17. Plots of n versus $-V_G$ for an ILGT fabricated with annealed PBTTT-C16

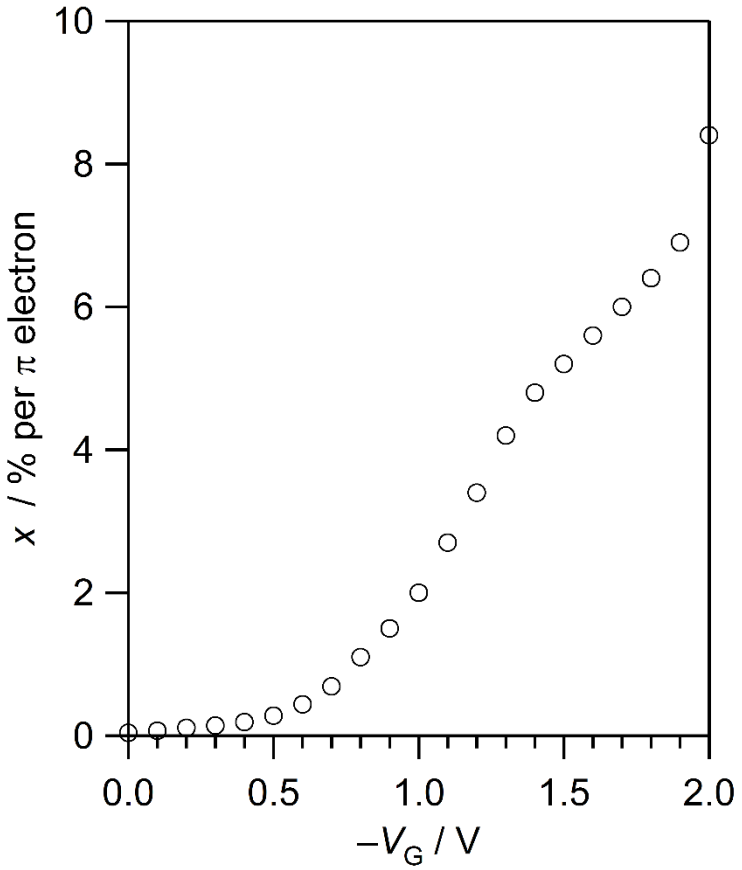

Figure 3.18. Plots of x versus $-V_G$ for an ILGT fabricated with annealed PBTTT-C16

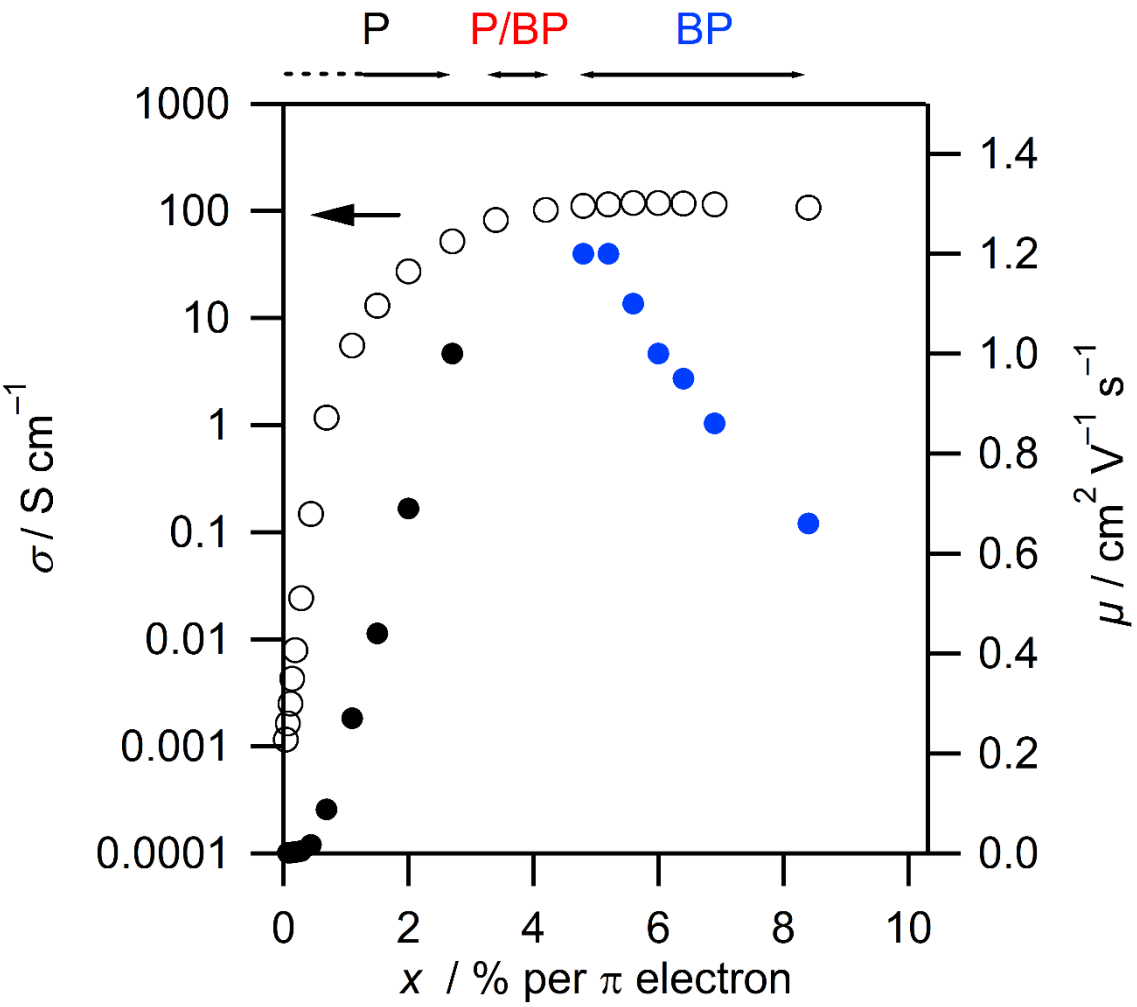

Figure 3.19. Plots of σ and μ versus x for an ILGT fabricated with annealed PBTTT-C16

Table 3.1. Parameters of the Raman band fitting

Assignments	Peak position / cm^{-1}	FWHM / cm^{-1}	Gaussian ratio / %
Crystalline	1489.4	12	0
Amorphous	1492	Variable	Variable

Table 3.2. Values of the parameters of the amorphous band

Annealing temperature / °C	FWHM / cm^{-1}	Gaussian ratio / %
Unannealed	18.1	98.3
180	12.1	78.2
235	12.8	89.7
250	13.1	100

Table 3.3. Values of X_C

Annealing temperature / °C	X_C	
	$\sigma_C/\sigma_A = 0.59$ [21]	$\sigma_C/\sigma_A = 1.04$ [23]
Unannealed	0.66	0.52
180	0.81	0.71
235	0.92	0.86
250	0.91	0.85

Chapter 4

Study on the dependence of doping on the ionic liquid species in ILGTs fabricated with PBTTT-C16

4.1 Introduction

In this chapter, the effect of anions in ILGTs fabricated with a PBTTT-C16 film was investigated using Raman spectroscopy and electrochemical measurements. Several ionic liquids can be used gate insulators in ILGTs [1–11]. The ionic liquid can affect the electrical properties of the ILGTs, such as mobilities, conductivities and threshold voltages [12,13].

The stability of polarons and bipolarons is explained by electron-lattice interaction and electron-electron interaction as a basic theory [14,15]. In addition, counterions also affect the stability of polarons and bipolarons [16,17]. In electrochemical doping, charges are injected into an active layer with migration of anions into the layer, whereas only charges are injected into the layer in typical OFETs [13]. The injected anions are placed on a polymer chain as counterions. Therefore, anions affect carrier generation, as the stability of positive polarons and bipolarons depends on anions. However, the effect of anions on the critical doping level of the polaron-to-bipolaron transition has not been elucidated yet. [EMIM][TFSI] or [EMIM][FAP] (Figure 4.1) were used as a gate dielectric in this chapter. These ionic liquids have two different sizes of anions, $[TFSI]^-$ and $[FAP]^-$. The critical doping level of the polaron-to-bipolaron transition and the mobilities of positive polarons and bipolarons were obtained using electrochemical measurements based on ILGTs fabricated with [EMIM][TFSI] or [EMIM][FAP]. Herein, I discuss the carrier generation and the electrical properties of the PBTTT-C16 films doped with $[TFSI]^-$ and $[FAP]^-$.

4.2 Experimental methods

4.2.1 Materials and devices

The structures of the ILGTs were the same as that described in Section 2. Ni (5 nm) and Au (45 nm) were deposited on the glass substrate as the source and drain electrodes using a shadow mask. The width and length of the channel were 1.0 mm and 5.0×10 μm, respectively. The PBTTT-C16 films were prepared from a 1,2-dichlorobenzene solution (12 mg/mL, at 90 °C) by spin coating. [EMIM][TFSI] and [EMIM][FAP] were purchased from Kanto Chemical and Merck, respectively, and were used as the gate dielectric. The thickness of the ionic-liquid layer was 200 μm using a Naflon® (polytetrafluoroethylene) spacer. The surfaces of ITO-coated glass substrates with a sheet resistivities of 30 $\Omega\ sq^{-1}$ were cleaned with UV-ozone plasma treatment and used as

the gate electrodes.

4.2.1 Raman and electrochemical measurements

Raman and electrochemical measurements were performed in the same way as in chapter 3. Raman spectra were acquired every 0.1 V of $-V_G$ from 0.0 to 1.7 V for an ILGT with [EMIM][TFSI] and from 0.0 to 1.4 V for an ILGT with [EMIM][FAP]. The injected charge (Q), the charge density (n), the doping level per π electron (x, %/π electron), the average electrical conductivity (σ) in the channel and the mobility (μ) of positive polarons and bipolarons were obtained in the same way as in chapter 3.

4.3 Results and discussion

4.3.1 Raman spectra of ILGTs

The changes in the Raman spectra of an ILGT with [EMIM][TFSI] are shown in Figure 4.2. The spectrum collected at $-V_G$ = 0.0 V is attributed to neutral PBTTT-C16. The intensity of the 1391-cm^{-1} band at $-V_G$ = 0.5 V increases. The spectra collected at $-V_G$ = 0.5 and 0.6 V are attributed to the mixture of neutral species and polarons. The spectra acquired between $-V_G$ = 0.7 and 1.0 V indicate the presence of polarons because these spectra have features similar to the spectra of polarons generated with $FeCl_3$ doping. The spectra acquired between $-V_G$ = 1.2 and 1.4 V are attributed to a mixture of polarons and bipolarons. The spectra acquired between $-V_G$ = 1.5 and 1.7 V are attributed to bipolarons. Accordingly, polarons form below $-V_G$ = 1.0 V, polarons and bipolarons coexist between $-V_G$ = 1.2 and 1.4 V, and bipolarons are dominant above $-V_G$ = 1.5 V.

The changes in the Raman spectra of an ILGT with [EMIM][FAP] are shown in Figure 4.3. The spectrum acquired at $-V_G$ = 0.0 V is attributed to neutral PBTTT-C16. The intensity of the 1391-cm^{-1} band at $-V_G$ = 0.1 V increases. The spectra acquired between $-V_G$ = 0.1 and 0.5 V indicate the presence of both neutral species and polarons. The spectra collected between $-V_G$ =0.6 and 1.3 V are attributed to polarons. The spectrum collected at $-V_G$ = 1.4 indicates a mixture of both polarons and bipolarons. In this region, a spectrum originating from only bipolarons was not observed. Accordingly, polarons form below $-V_G$ = 1.3 V, and polarons and bipolarons coexist

at $-V_G$ = 1.4 V.

4.3.2 Electrical properties of ILGTs

The transfer characteristics of an ILGT fabricated with [EMIM][TFSI] at V_D = −0.01 V are shown in Figure 4.4. The $-I_D$ increases gradually until $-V_G$ = 0.5 V due to electrostatic doping. On the other hand, $-I_D$ increases rapidly from 0.6 to 1.2 V and shows a plateau from 1.2 to 1.5 V. From 1.6 to 1.7, $-I_D$ decreases slightly. The n and x values were calculated from measured Q values using electrochemical measurements. The relationship between n and $-V_G$ is shown in Figure 4.5; the relationship between x and $-V_G$ is shown in Figure 4.6. According to the Raman results, polarons are generated below 3.2%. Bipolarons begin to form at x = 4.5% and are dominant above x = 9.9%. The σ values were calculated from the observed I_D values and were plotted against x in Figure 4.7. The σ values increase gradually from x = 0 to 0.14% and then increase rapidly above x = 0.28%. The maximum σ value is 137 S cm^{-1}, which was observed at x = 6.1% ($-V_G$ = 1.3 V). The μ values of the polarons were obtained from the data collected below x = 3.2% (n = 3.8×10^{20} cm^{-3}, $-V_G$ = 1.1 V); the μ values of the bipolarons were obtained from the data collected above x = 9.9% (n = 1.2×10^{21} cm^{-3}, $-V_G$ = 1.5 V). These μ values were plotted against x and are also shown in Figure 4.8. The μ values of the polarons depend on x, and they increase with increasing x. The μ values of the bipolarons are moderately dependent on x, and they decrease with increasing x. The highest μ values of the polarons and bipolarons were 1.3 cm^2 V^{-1} s^{-1} (x = 3.2%, n = 6.4×10^{20} cm^{-3}) and 0.56 cm^2 V^{-1} s^{-1} (x = 9.9%, n = 1.2×10^{21} cm^{-3}), respectively.

The transfer characteristics of an ILGT fabricated with [EMIM][FAP] at V_D = −0.01 V are shown in Figure 4.9. The $-I_D$ increases gradually until $-V_G$ = 0.5 V due to electrostatic doping. On the other hand, $-I_D$ increases rapidly from 0.6 to 1.1 V and plateaus from 1.1 to 1.4 V due to electrochemical doping. The relationship between n and $-V_G$ is shown in Figure 4.10; the relationship between x and $-V_G$ is shown in Figure 4.11. According to the Raman results, polarons are generated below 12%, and bipolarons form at x = 14%. The σ values were plotted against x for both [EMIM][TFSI] and [BMIM][TFSI] in Figure 4.7. The σ values increase gradually from x = 0 to 1.5% and then increase rapidly above x = 1.9%. The maximum σ value is 158 S cm^{-1}, and this value was observed at x = 14% ($-V_G$ = 1.4 V). The μ values of the polarons were obtained from the data collected below x = 12% (n = 1.4×10^{21} cm^{-3}, $-V_G$ = 1.3 V). The μ values of the

bipolarons cannot be obtained in this region. The μ values were plotted against x for both [EMIM][TFSI] and [BMIM][TFSI] in Figure 4.8. The mobilities of the polarons increased as the doping level increased and remained at high at values over 7.6%. The highest μ value of the polarons was 0.72 $cm^2 V^{-1} s^{-1}$ (x = 9.5%, $n = 1.1\times10^{21}$ cm^{-3}).

4.3.3 The relation between the carrier type and the doping level

The relation between carrier type and the doping level is shown in Figure 4.12. Bipolarons are formed firstly as the doping level increasing, and then bipolarons are formed. Bipolarons in the PBTTT-C16 film doped with [EMIM][FAP] are formed at 14%. On the other hand, bipolarons in the PBTTT-C16 films doped with [EMIM][TFSI] and [BMIM][TFSI] are formed at 4.5 and 7.3%; bipolarons are dominant above 9.9 and 11%, respectively. Thus, the bipolaron formation depends on dopant anions.

Molecular structures and volumes of $[FAP]^-$ and $[TFSI]^-$ were calculated with the DFT method based on the B3LYP/6-31++G(d,p) level using Gaussian 09 [18]. The calculated structures of anions are shown in Figure 4.13. The volumes of $[FAP]^-$ and $[TFSI]^-$ are 310 and 223 $Å^3$, respectively. The volume of $[FAP]^-$ is larger than $[TFSI]^-$. Bipolarons in PBTTT-C16 doped with $[FAP]^-$ are formed at higher doping level than $[TFSI]^-$. Therefore, bipolaron formation may be sensitive to the size of anion. Two charges of a bipolaron are localized over several thiophene rings. Two counter anions exist near the bipolaron. The charge localization stabilizes a bipolaron formation. $[FAP]^-$ anions are localized in a large region than $[TFSI]^-$ anions because of the size. Thus, the stabilization originating from charge localization for $[FAP]^-$ anions is smaller than that for $[TFSI]^-$ anions.

4.4 Conclusion

Carrier formation in ILGTs fabricated with [EMIM][TFSI] and [EMIM][FAP] was observed using Raman spectroscopy. The mobilities of polarons and bipolarons were evaluated using electrochemical measurements. The highest μ values of the polarons and bipolarons in the ILGT fabricated with [EMIM][TFSI] were 1.3 $cm^2 V^{-1} s^{-1}$ (x = 3.2%, $n = 6.4\times10^{20}$ cm^{-3}) and 0.56 $cm^2 V^{-1} s^{-1}$ (x = 9.9%, $n = 1.2\times10^{21}$ cm^{-3}), respectively. The highest μ value of the polarons in the ILGT fabricated with [EMIM][FAP] was 0.72 $cm^2 V^{-1} s^{-1}$ (x = 9.5%, $n = 1.1\times10^{21}$ cm^{-3}). These

values are on the same order as those in the ILGTs fabricated with [BMIM][TFSI]. Polarons doped with $[TFSI]^-$ are formed below x = 3.2%. Bipolarons doped with $[TFSI]^-$ begin to form at x = 4.5% and are the dominant carriers above x = 9.9%. Polarons doped with $[FAP]^-$ are formed below 12%. Bipolarons doped with $[FAP]^-$ begin to form at x = 14%. The presence of $[FAP]^-$ ions impeded bipolaron formation because of their larger size relative to $[TFSI]^-$ ions. The carrier formation can be controlled by choosing an appropriate ionic liquid, and careful selection helps to improve the electrical properties of ILGTs.

4.5 References

[1] J. Lee, M.J. Panzer, Y. He, T.P. Lodge, C.D. Frisbie, Ion gel gated polymer thin-film transistors, J. Am. Chem. Soc. 129 (2007) 4532–4533. doi:10.1021/JA070875E.

[2] E. Schmidt, S. Shi, P.P. Ruden, C.D. Frisbie, Characterization of the electric double layer formation dynamics of a metal/ionic liquid/metal structure, ACS Appl. Mater. Interfaces. 8 (2016) 14879–14884. doi:10.1021/acsami.6b04065.

[3] Y. Kaji, K. Ogawa, R. Eguchi, H. Goto, Y. Sugawara, T. Kambe, K. Akaike, S. Gohda, A. Fujiwara, Y. Kubozono, Characteristics of conjugated hydrocarbon based thin film transistor with ionic liquid gate dielectric, Org. Electron. 12 (2011) 2076–2083. doi:10.1016/J.ORGEL.2011.08.016.

[4] W. Shi, J. Ye, J.G. Checkelsky, C. Terakura, Y. Iwasa, Transport properties of polymer semiconductor controlled by ionic liquid as a gate dielectric and a pressure medium, Adv. Funct. Mater. 24 (2014) 2005–2012. doi:10.1002/adfm.201302954.

[5] T. Harada, H. Ito, Y. Ando, S. Watanabe, H. Tanaka, S. Kuroda, Signature of the insulator-metal transition of a semicrystalline conjugated polymer in ionic-liquid-gated transistors, Appl. Phys. Express. 8 (2015) 021601. doi:10.7567/APEX.8.021601.

[6] J.O. Guardado, A. Salleo, Structural effects of gating poly(3-hexylthiophene) through an ionic liquid, Adv. Funct. Mater. 27 (2017) 1701791. doi:10.1002/adfm.201701791.

[7] S. Ono, K. Miwa, S. Seki, J. Takeya, A comparative study of organic single-crystal transistors gated with various ionic-liquid electrolytes, Appl. Phys. Lett. 94 (2009) 063301. doi:10.1063/1.3079401.

[8] Y. Nagasaki, J.-H. Lee, Y. Kubozono, T. Kambe, Dynamics of carrier injection in picene thin-film field-effect transistors with an ionic liquid sheet and ionic liquid gel, Org. Electron. 15 (2014) 3070–3075. doi:10.1016/J.ORGEL.2014.08.043.

[9] Y. Xia, J.H. Cho, J. Lee, P.P. Ruden, C.D. Frisbie, Comparison of the mobility-carrier density relation in polymer and single-crystal organic transistors employing vacuum and liquid gate dielectrics, Adv. Mater. 21 (2009) 2174–2179. doi:10.1002/adma.200803437.

[10] J.H. Cho, J. Lee, Y. Xia, B. Kim, Y. He, M.J. Renn, T.P. Lodge, C. Daniel Frisbie, Printable ion-gel gate dielectrics for low-voltage polymer thin-film transistors on plastic, Nat. Mater. 7 (2008) 900–906. doi:10.1038/nmat2291.

[11] S. Wang, M. Ha, M. Manno, C. Daniel Frisbie, C. Leighton, Hopping transport and the

Hall effect near the insulator–metal transition in electrochemically gated poly(3-hexylthiophene) transistors, Nat. Commun. 3 (2012) 1210. doi:10.1038/ncomms2213.

[12] B.D. Paulsen, C.D. Frisbie, Dependence of conductivity on charge density and electrochemical potential in polymer semiconductors gated with ionic liquids, J. Phys. Chem. C. 116 (2012) 3132–3141. doi:10.1021/jp2093934.

[13] T. Fujimoto, M.M. Matsushita, K. Awaga, Ionic-liquid component dependence of carrier injection and mobility for electric-double-layer organic thin-film transistors, J. Phys. Chem. C. 116 (2012) 5240–5245. doi:10.1021/jp2122642.

[14] K. Fesser, A.R. Bishop, D.K. Campbell, Optical absorption from polarons in a model of polyacetylene, Phys. Rev. B. 27 (1983) 4804–4825. doi:10.1103/PhysRevB.27.4804.

[15] Y. Shimoi, S. Abe, K. Harigaya, Theory of optical absorption in doped conjugated polymers, Mol. Cryst. Liq. Cryst. Sci. Technol. Sect. A. Mol. Cryst. Liq. Cryst. 267 (1995) 329–334. doi:10.1080/10587259508034012.

[16] S. Irle, H. Lischka, An *ab initio* investigation of the charge−transfer complexes of alkali atoms with oligo (α,α′) thiophenes and oligoparaphenylenes: A model calculation on polaronic and bipolaronic defect structures, J. Chem. Phys. 103 (1995) 1508–1522. doi:10.1063/1.469772.

[17] N. Zamoshchik, M. Bendikov, Doped conductive polymers: Modeling of polythiophene with explicitly used counterions, Adv. Funct. Mater. 18 (2008) 3377–3385. doi:10.1002/adfm.200800639.

[18] M. J. Frisch, G. W. Trucks, H. B. Schlegel, G. E. Scuseria, M. A. Robb, J. R. Cheeseman, G. Scalmani, V. Barone, B. Mennucci, G. A. Petersson, H. Nakatsuji, M. Caricato, X. Li, H. P. Hratchian, A. F. Izmaylov, J. Bloino, G. Zheng, J. L. Sonnenberg, M. Hada, M. Ehara, K. Toyota, R. Fukuda, J. Hasegawa, M. Ishida, T. Nakajima, Y. Honda, O. Kitao, H. Nakai, T. Vreven, J. A. Montgomery, Jr., J. E. Peralta, F. Ogliaro, M. Bearpark, J. J. Heyd, E. Brothers, K. N. Kudin, V. N. Staroverov, T. Keith, R. Kobayashi, J. Normand, K. Raghavachari, A. Rendell, J. C. Burant, S. S. Iyengar, J. Tomasi, M. Cossi, N. Rega, J. M. Millam, M. Klene, J. E. Knox, J. B. Cross, V. Bakken, C. Adamo, J. Jaramillo, R. Gomperts, R. E. Stratmann, O. Yazyev, A. J. Austin, R. Cammi, C. Pomelli, J. W. Ochterski, R. L. Martin, K. Morokuma, V. G. Zakrzewski, G. A. Voth, P. Salvador, J. J. Dannenberg, S. Dapprich, A. D. Daniels, O. Farkas, J. B. Foresman, J. V. Ortiz, J. Cioslowski, D. J. Fox, Gaussian, Inc., Wallingford CT, Gaussian 09, Revision C.01, (2010).

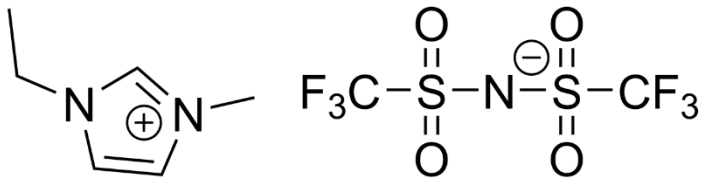

[EMIM][TFSI]

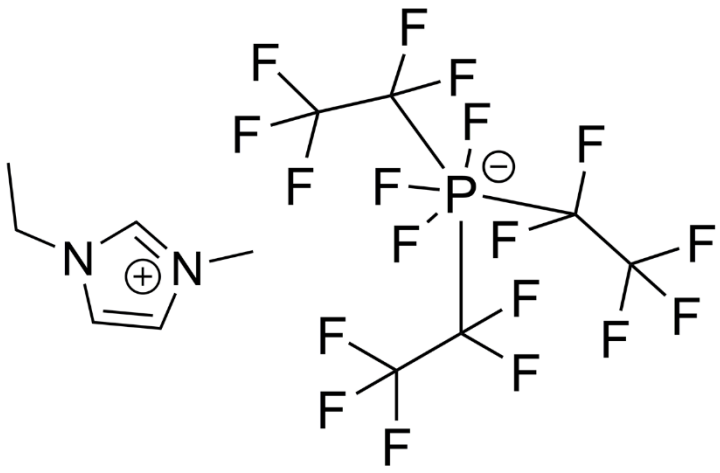

[EMIM][FAP]

Figure 4.1. The chemical structures of [EMIM][TFSI] and [EMIM][FAP]

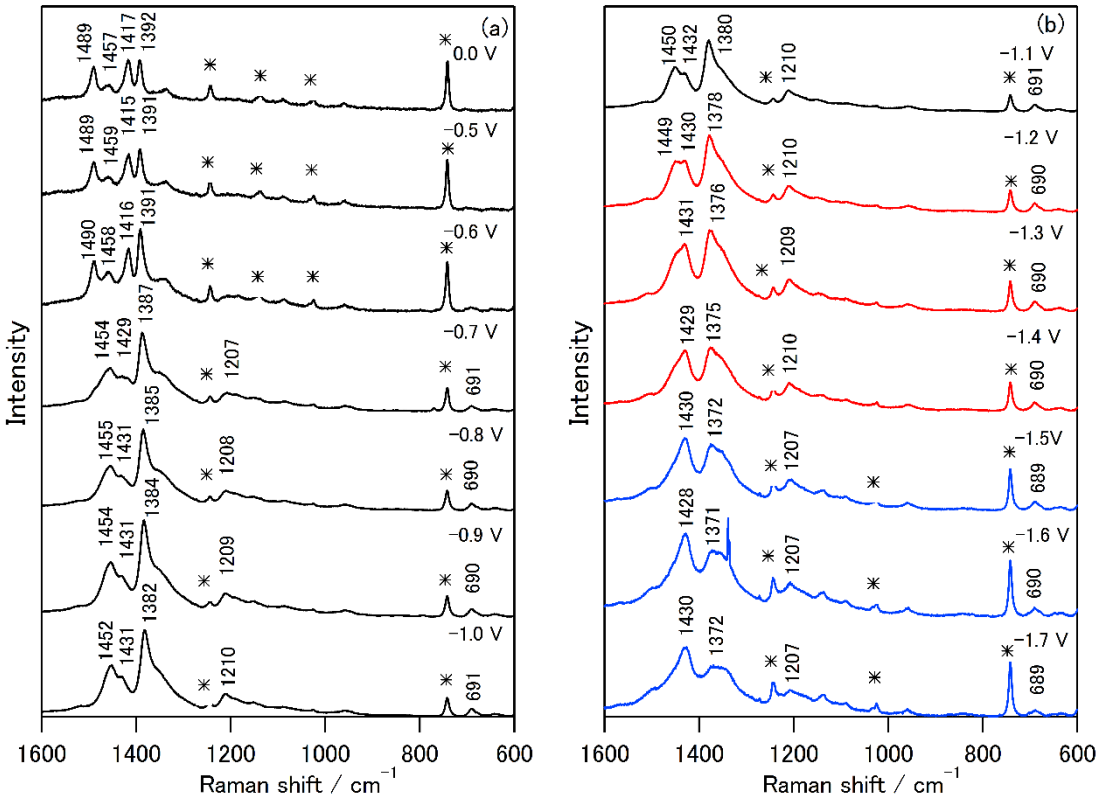

Figure 4.2. Raman spectra of an ILGT with [EMIM][TFSI]

(* indicates the bands of [EMIM][TFSI])

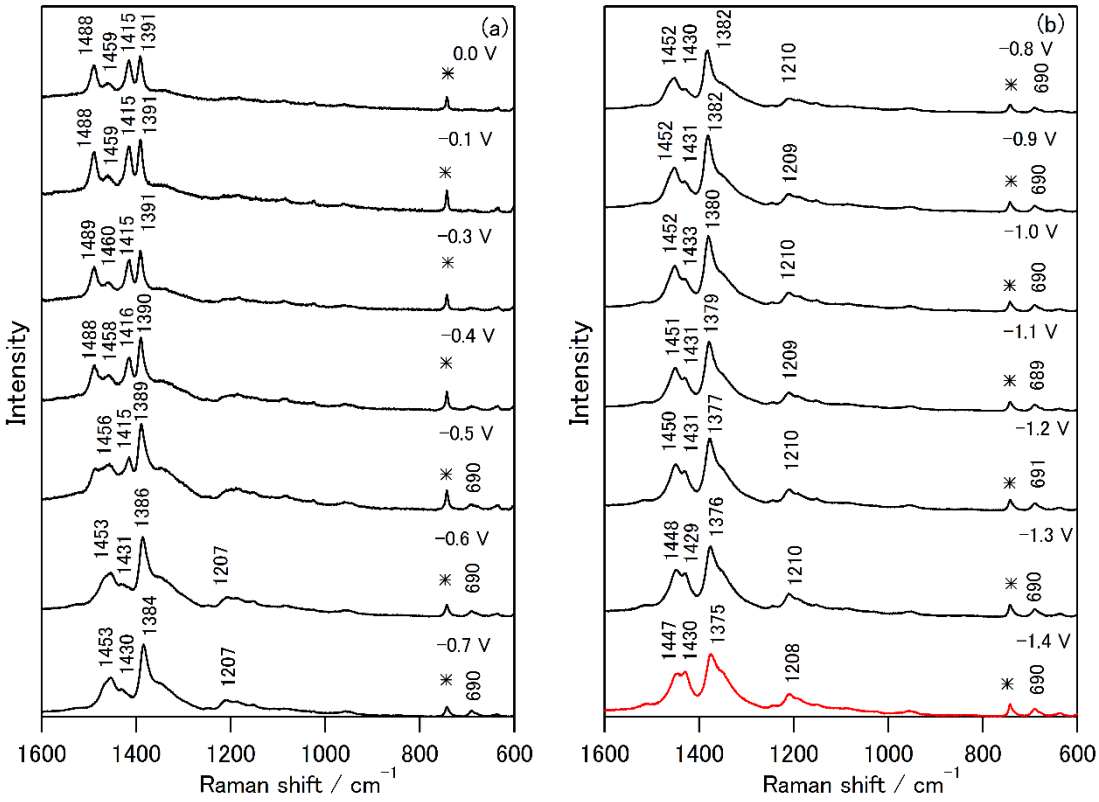

Figure 4.3. Raman spectra of an ILGT with [EMIM][FAP]

(* indicates the bands of [EMIM][FAP])

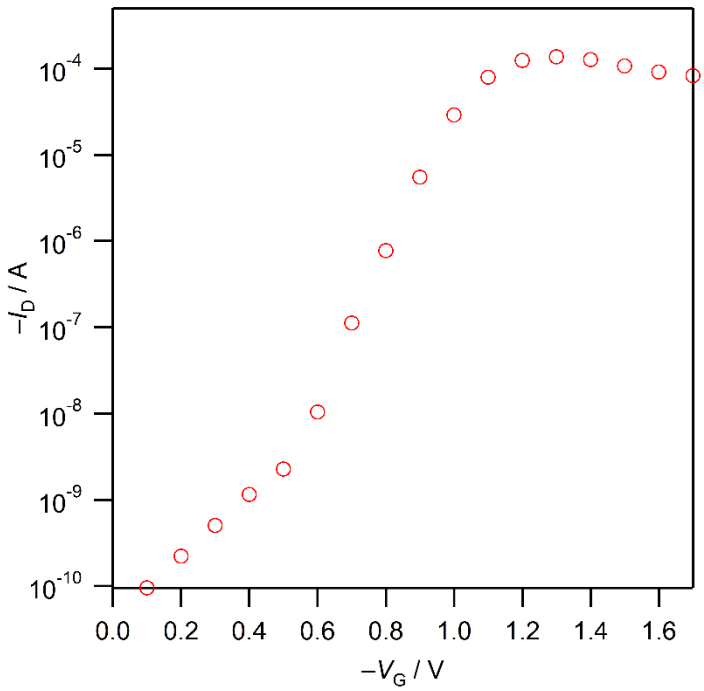

Figure 4.4. Transfer characteristics of an ILGT fabricated with [EMIM][TFSI]

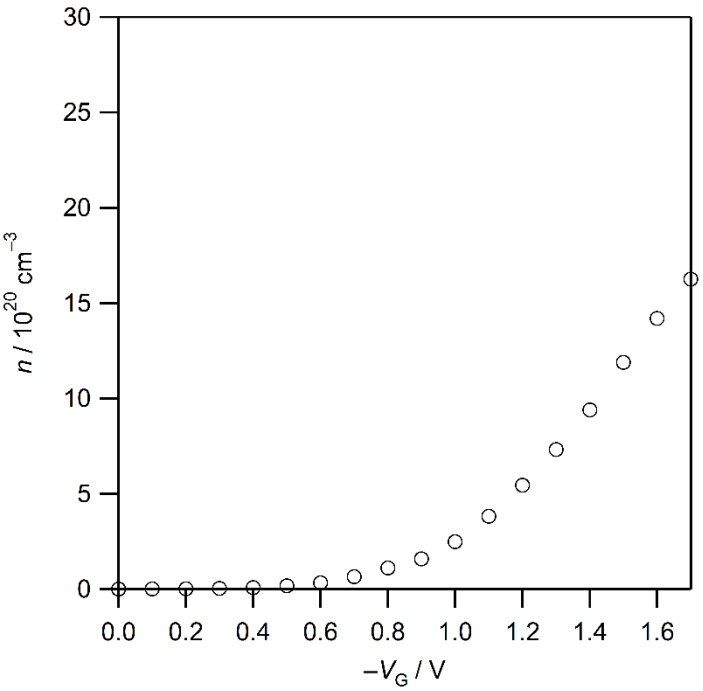

Figure 4.5. Plots of n versus $-V_G$ for an ILGT fabricated with [EMIM][TFSI]

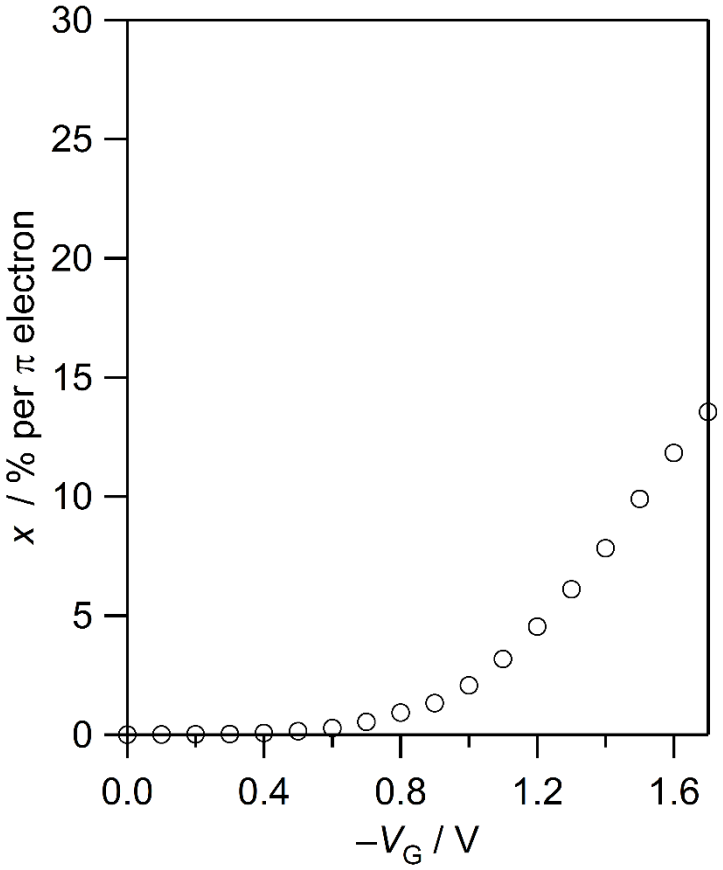

Figure 4.6. Plots of x versus $-V_G$ for an ILGT fabricated with [EMIM][TFSI]

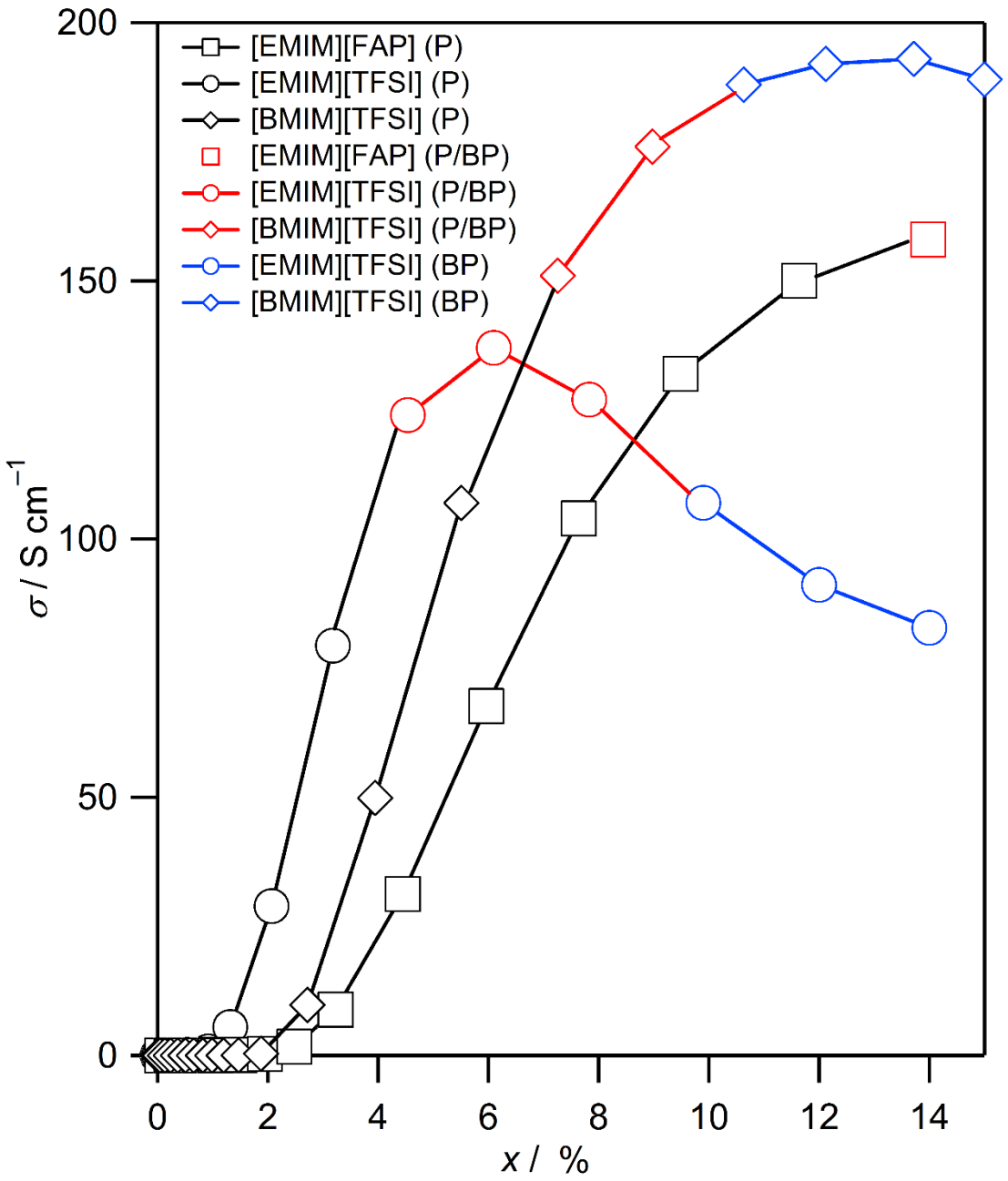

Figure 4.7. Conductivities of PBTTT-C16 films doped with three ionic liquids

(P indicates polarons, and BP indicates bipolarons)

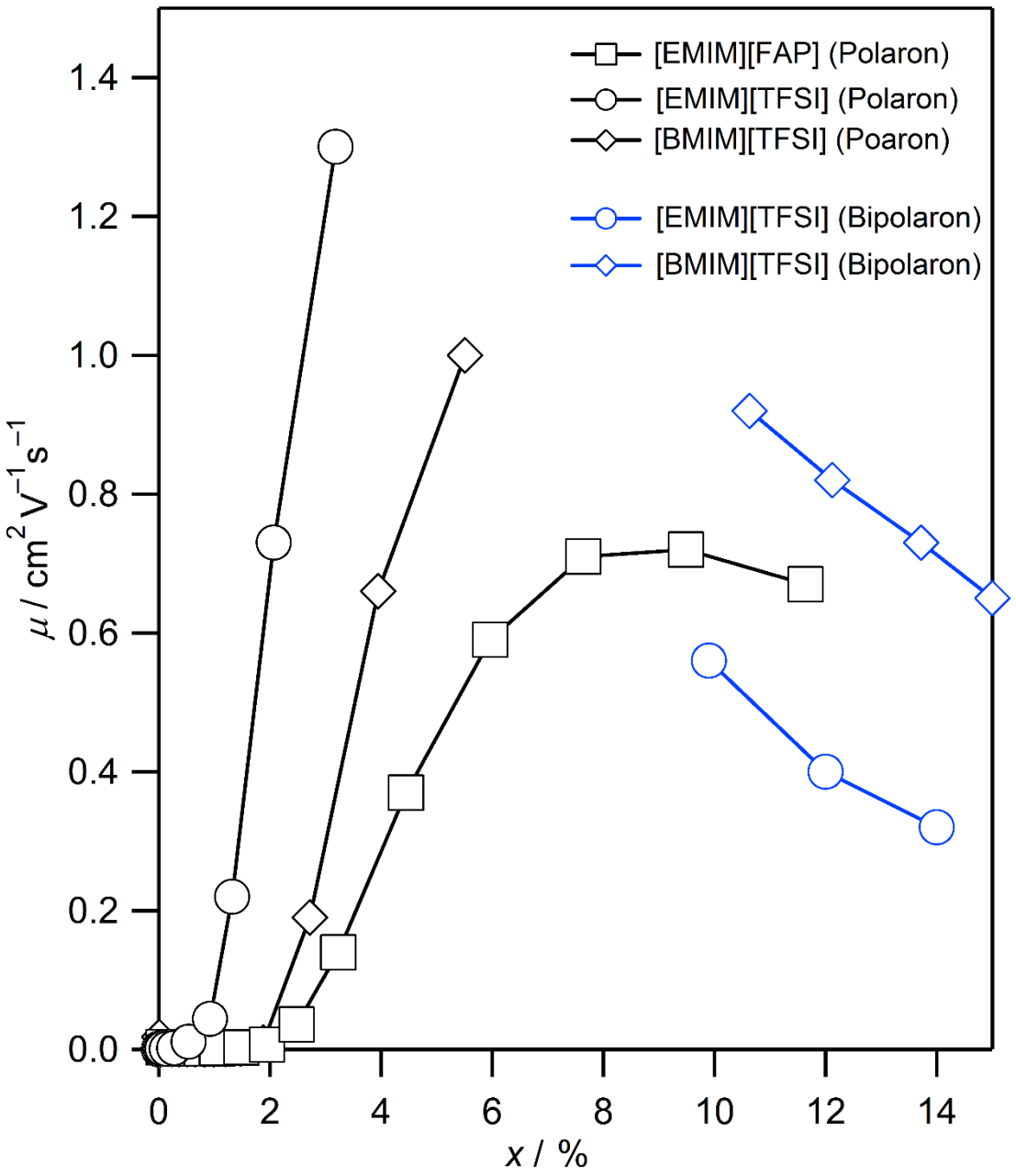

Figure 4.8. Mobilities of polarons and bipolarons in PBTTT-C16 doped with three ionic liquids

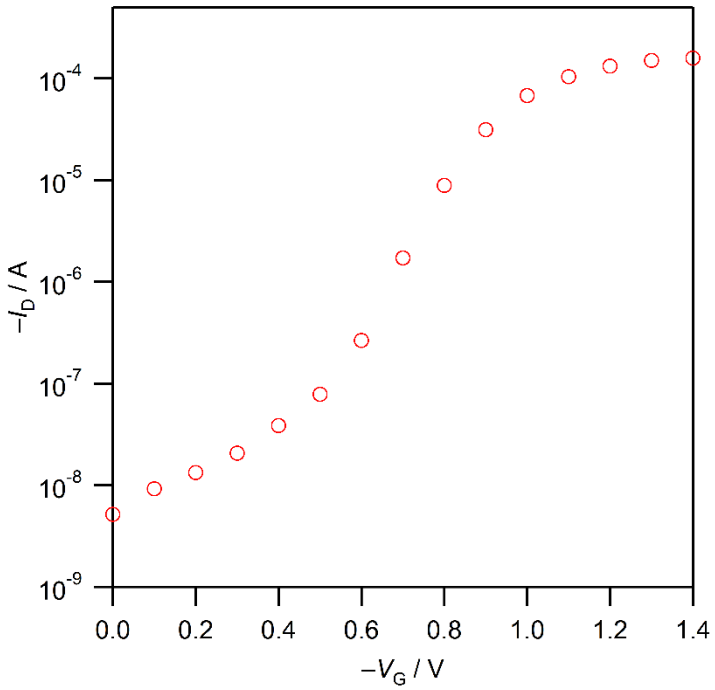

Figure 4.9. Transfer characteristics of an ILGT with [EMIM][FAP]

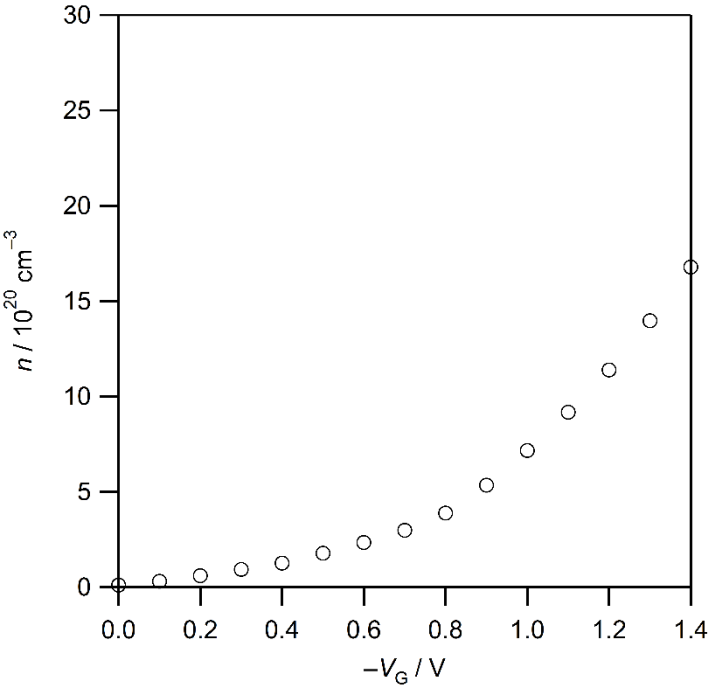

Figure 4.10. Plots of n versus $-V_G$ for an ILGT fabricated with [EMIM][FAP]

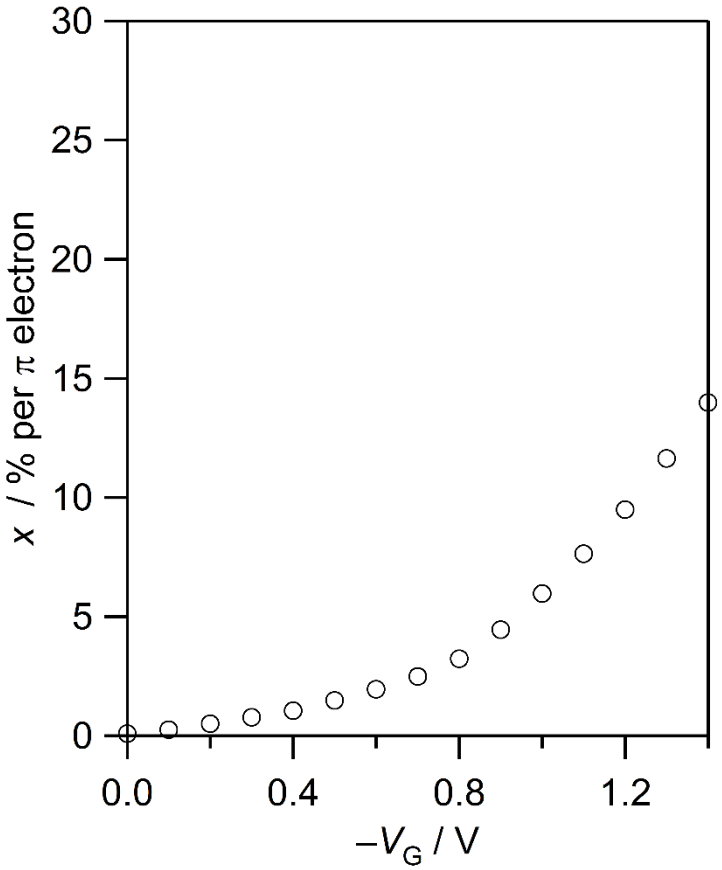

Figure 4.11. Plots of x versus $-V_G$ for an ILGT fabricated with [EMIM][FAP]

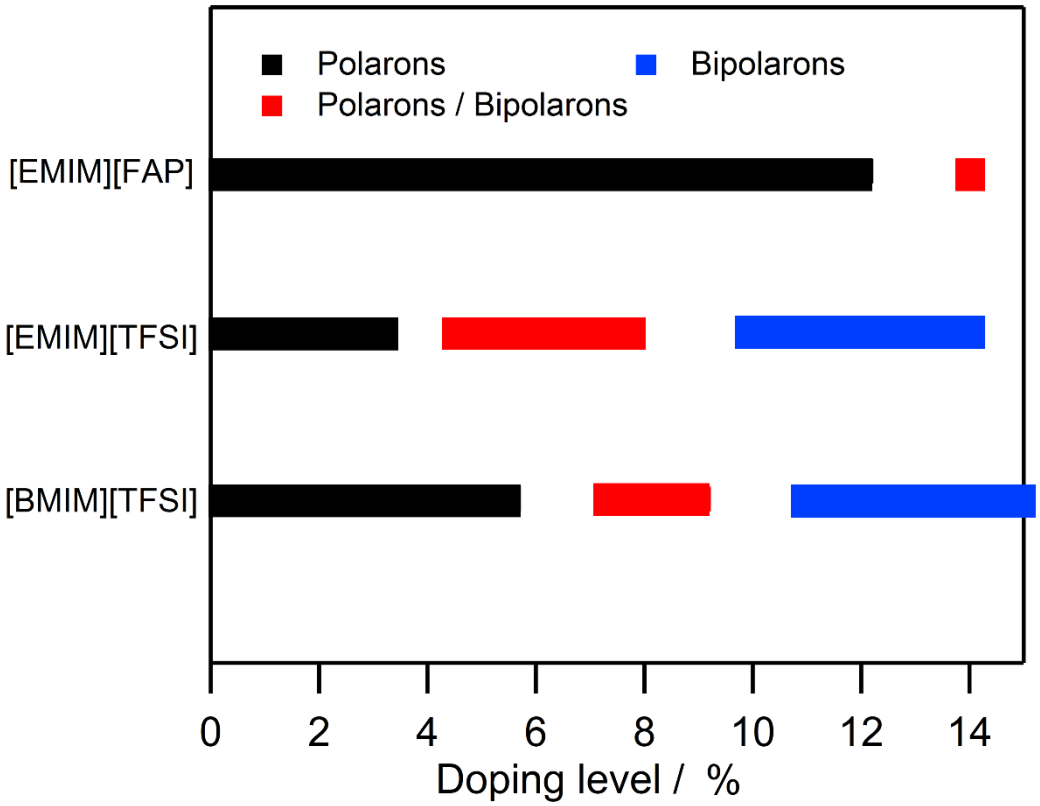

Figure 4.12. Plots of carrier types versus doping levels for ILGTs

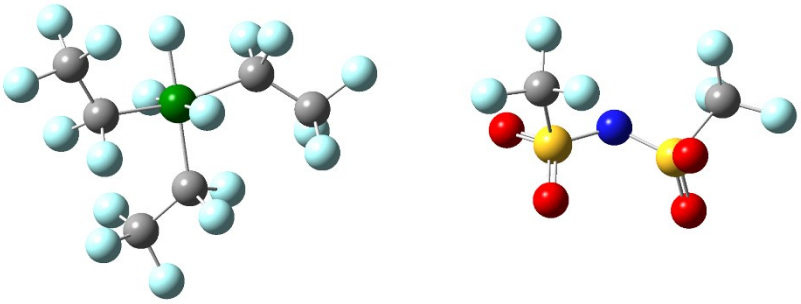

[FAP]⁻ [TFSI]⁻

Figure 4.13. Calculated molecular structures

Chapter 5

Conclusion

5. Conclusion

In this thesis, I investigated the relationship between polaron and bipolaron generation and conductivities, doping levels and mobilities in ILGTs fabricated with PBTTT using Raman spectroscopy and electrochemical measurements.

In Chapter 2, I investigated the ILGT fabricated with PBTTT-C14 and [BMIM][TFSI]. Raman spectra of positive polarons and bipolarons of PBTTT-C14 were identified according to the optical absorption spectra of the films doped with $FeCl_3$. Polaron and bipolaron formations in the ILGT were elucidated using the Raman spectra of polarons and bipolarons. The conductivities, doping levels and mobilities in the ILGT were obtained using electrochemical measurements. The highest mobility of polarons (4.2×10^{-2} cm^2 V^{-1} s^{-1}) was observed at the doping level equaling to 1.5%; the highest mobility of bipolarons (0.36 cm^2 V^{-1} s^{-1}) was observed at the doping level equaling to 8.2%. Bipolarons having a high mobility is quite unique, and it indicates that bipolarons can be used as effective carriers for ILGTs.

In Chapter 3, I investigated the ILGTs fabricated with unannealed and annealed PBTTT-C16 films. The crystalline contents of the PBTTT-C16 films were evaluated using Raman spectroscopy. The Raman spectra of positive polarons and bipolarons of PBTTT-C16 were identified according to the optical absorption spectra of the films doped with $FeCl_3$. The bipolarons of PBTTT-C16 also showed high mobilities. The high crystalline contents of annealed PBTTT-C16 resulted in bipolarons with slightly improved mobilities. Carrier formation was influenced by the crystalline contents. The bipolarons in annealed PBTTT-C16 were formed at 3.4% comparing to in unannealed PBTTT-C16 at 7.3%. It indicates that polarons are stable in the disordered structure of PBTTT-C16.

In Chapter 4, I investigated the relationship between carrier generation and the size of the anions of an ionic liquid. ILGTs fabricated with [EMIM][TFSI] and [EMIM][FAP] were evaluated using Raman spectroscopy and electrochemical measurements. Bipolarons in the PBTTT-C16 films doped with [EMIM][FAP] and [EMIM][TFSI] are formed at 14 and 4.5%, respectively. The large anions prevented the bipolaron formation in the ILGTs, indicating that carrier formation can be controlled by choosing the anion in ionic liquids.

The investigations in this thesis show that the combination of Raman spectroscopy and electrochemical measurements is a powerful tool for elucidating carrier formation in organic semiconductors in ILGTs. Bipolarons can be used as an effective carrier, and carrier formation can be controlled. These results will help advance the field of organic electronics, organic

spintronics and organic magnetic functionality. For example, polarons are used as a carrier for spin currents, whereas bipolarons are used as spinless carriers for electric currents. In addition, it has been reported that bipolarons affect the properties of not only transistors but also solar cells, light-emitting diodes and magneto resistive sensors. However, these mechanisms have not elucidated completely because they were investigated using ESR. This thesis helps to understand and elucidate the fundamental mechanism of the effect of bipolaron in several organic devices. Further research and development will lead to the preparation of flexible, low-cost and novel organic devices based on ILGTs.

Acknowledgments

I would like to express the deepest appreciation to my supervisor, Prof. Yukio Furukawa. He gives me insightful comments, generous support and encouragement. Without his guidance and persistent help, this thesis would not have been possible. I also appreciate him to give me the many opportunity to have an irreplaceable experiment, such as attending the international conference, organizing international symposium, working abroad as an intern.

I am also deeply grateful to Prof. Yoshinori Nishikitani, Prof. Toru Asahi, and Dr. Takuro Sugiyama as referee in my Ph.D. thesis committee. Their insightful comments and suggestions have been a great help in writing this thesis.

During my graduate life, I have many opportunities to go abroad. I would like to express my gratitude to Dr. Oscar Cabellos and all members in OECD/NEA Data Bank, and Prof. Akifumi Yamaji and Mr. Kiyoshi Matsumoto in Waseda University. They gave me a great support to work and live there. I was able to have a wonderful time in their thanks.

I would like to express my gratitude to Prof. Sergei Kazarian for allowing me to do research as an intern in Imperial College London. He gave me the excellent opportunity to challenge new research fields and to expand my insight. I am also grateful to Denisa Lizoňová and all members in the laboratory. They kindly supported me for the experiment to be successful. I was able to have a wonderful time in their thanks.

I would like to offer my special thanks to Dr. Yasuhiro Iwasawa, Dr. Yoshifumi Wada, and Ms. Moeka Oshiro. They always helped me as a member of the same Leading program. I am deeply grateful to Dr. Jun Yamamoto, Mr. Kotaro Akiyama, Ms. Kana Monya, Ms. Xin Jing and Ms. Natsuki Imai as colleagues working on ionic-liquid-gated transistors. I also appreciate the members in Prof. Furukawa laboratory, Dr. Miho Momose, Dr. Kenji Takashima, Dr. Hayato Isoda, Mr. Ryota Iwasaki, Mr. Hirotaka Murata, Ms. Miho Nitta, Mr. Hiroki Yoshida, Mr. Kogoro Hayashi, Mr. Kei Kanazawa, Ms. Sachie Goto, Ms. Maia Kamei, Ms. Nagisa Kawate, Mr. Tasuku Nakamura, Mr. Yusuke Sakaki, Ms. Tomoko Yokoyama, Mr. Shin Hisatsune, Mr. Yusaku Karatsu, Mr. Tatsuya Makino, Ms. Yumi Tanaka, Ms. Mebae Kojima, Mr. Hirotaka Koriki, Mr. Kunpei Maruyama, Mr. Kousuke Nakada, Mr. Makoto Saito, Mr, Daiki Shuto, Ms. Haruna Itagaki, Mr. Noriaki Oki, Mr. Masafumi Yamashita, Mr. Ken Yoshinaka, Ms. Sakurako Wada, Mr. Nuo Xu, Mr. Seiya Ikawa, Mr. Yui Ishikawa, Ms. Shiho Matsumuro, Mr. Kanato Takahashi, Mr. Shuhei Yamaguchi, Mr. Yugo Kikuchi, Mr. Kota Kimura, Ms. Hanako Kiyohara, Mr. Takayuki Kushida and Mr. Yuki

Sendai. I also appreciate other all former members in Prof. Furukawa laboratory to help my graduate life.

I appreciate all members at Materials Characterization Central Laboratory, Waseda University. They always helped me to use the laboratory, do experiment and analyze the data.

I was supported by the Leading Graduate Program in Science and Engineering of Waseda University from the MEXT of Japan. I am deeply grateful to all members of this program for supporting my graduate life and giving me excellent opportunities.

Finally, I would like to express my great appreciation for my family. They always help and understand my graduate life.

List of research achievements

Journal papers

1. Ippei Enokida, Yukio Furukawa, “Doping-Level Dependent Mobilities of Positive Polarons and Bipolarons in Poly(2,5-bis(3-hexadecylthiophen-2-yl)thieno[3,2-b]thiophene) (PBTTT-C16) based on an ionic-liquid-gated transistor configuration”, Org. Electron., 2019, 68, 28.

2. Yoshifumi Wada, Ippei Enokida, Jun Yamamoto, Yukio Furukawa, “Raman Imaging of Carrier Distribution in the Channel of an Ionic Liquid-Gated Transistor Fabricated with Regioregular Poly(3-hexylthiophene)”, Spectrochimica Acta Part A: Molecular and Biomolecular Spectroscopy, 2018, 197, 166.

3. Yukio Furukawa, Kotaro Akiyama, Ippei Enokida, Jun Yamamoto, “Raman Spectra of Carriers in Ionic-Liquid-Gated Transistors Fabricated with Poly(2,5-bis(3-tetradecylthiophen-2-yl)thieno [3,2-b]thiophene), Vib. Spectrosc., 2016, 85, 29.

Conference presentation

1. Yukio Furukawa, Yoshifumi Wada, Yasuhiro Iwasawa, Ippei Enokida, “Raman Spectroscopy of Polymer Semiconductors Used for Electronic Devices”, The Great Scientific Exchange (SciX 2018), USA, October 2018.

2. 榎田一平，古川行夫, “Raman Study of Carriers in Ionic-Liquid-Gated Transistors Fabricated with Annealed and Unannealed PBTTT-C16 Films”，平成 30 年度日本分光学会年次講演会，神奈川，2018 年 5 月.

3. Ippei Enokida, Yukio Furukawa, “Study on Carriers of PBTTT-C16 Generated in Ionic-Liquid-Gated Transistors Using Raman Spectroscopy and Electrochemical Method”, 9th International Conference on Advanced Vibrational Spectroscopy, Canada, June 2017.

4. Ippei Enokida, Yuiko Furukawa, “Raman and Electrochemical Measurements of Ionic-Liquid-Gated Transistors Fabricated with PBTTT-C16”, 4th Taiwan International Symposium on Raman Spectroscopy, Taiwan, June 2016.

5. Ippei Enokida, Yukio Furukawa, “Study on Electrochemical Doping in Ionic-Liquid-Gated Transistors Fabricated with PBTTT”, 2015 International Chemical Congress of Pacific Basin Societies, USA, December 2015.

6. 榎田一平，古川行夫, “PBTTT-C16 を活性層としたイオン液体有機トランジスタのラマン分光法によるキャリヤー解析”, 第 75 回応用物理学会秋季学術講演会，愛知，2015 年 9 月.

7. Ippei Enokida, Yukio Furukawa, “Raman Study of Carriers Generated by Electrochemical Doping in Ionic-Liquid-Gated Transistors Fabricated with PBTTT-C16”, 5th Jilin-Korea-Waseda Alliance Annual Symposium, Japan, August 2015.

8. Ippei Enokida, Yukio Furukawa, “Raman Spectroscopic Study on Electrochemical Doping in Ionic-Liquid-Gated Transistors Fabricated with PBTTT”, 3rd Taiwan International Symposium on Raman Spectroscopy, Taiwan, July 2015.

9. Ippei Enokida, Yukio Furukawa, “Study on Two-Dimensional Solid Structure of Poly(3-hexylthiophene) Blend Films by Raman Imaging”, 4th Jilin-Korea-Waseda Alliance Annual Symposium, Korea, August 2014.

10. Ippei Enokida, Yukio Furukawa, “Resonance Raman Spectra of Thin Films of Poly[[4,8-bis[(2-ethylhexyl)oxy]benzo[1,2-b:4,5-b’]dithiophene-2,6-diyl][3-fluoro-2-[(2-ethylhexyl)carbonyl]thieno[3,4-b]thiophenediyl]](PTB7)”, International Conference on Raman Spectroscopy, Germany, August 2014.

11. 榎田一平，古川行夫，“ラマンイメージングと統計分析によるポリ（3ーヘキシルチオフェン）混合物薄膜の構造に関する研究”，平成 26 年度日本分光学会年次講演会，埼玉，2014 年 5 月.

Referees:

Professor Yukio Furukawa

Date 28/Jan/2019 Signature Yukio Furukawa

Professor Toru Asahi

Date 16/Jan./2019 Signature Toru Asahi

Professor Yoshinori Nishikitani

Date 17/Jan/2019 Signature Yoshinori Nishikitani

Dr. Takuro Sugiyama

Date 30/Jan/2019 Signature Takuro Sugiyama